

RESOLVING THE STELLAR POPULATIONS OF CLUMPY
STAR-FORMING GALAXIES USING FINITE RESOLUTION
DECONVOLUTION

Visal Sok

A THESIS SUBMITTED TO
THE FACULTY OF GRADUATE STUDIES
IN PARTIAL FULFILLMENT OF THE REQUIREMENTS
FOR THE DEGREE OF

MASTER OF SCIENCE

Graduate Program in Physics and Astronomy
York University, Toronto, Ontario

June 2020

© Visal Sok, 2020

Abstract

We have a broad understanding of the stellar mass build-up in galaxies over much of cosmic time, yet the detailed understanding of how and where stellar mass grows remains elusive. Compact star-forming regions in distant, irregular galaxies are often suggested to have a crucial role in this evolutionary process. These regions are generally defined as “clumps” and its host galaxy as “clumpy galaxies”. The study of clumpy galaxies requires high resolution and multi-wavelength observations to resolve these structures and to infer their physical properties. While current efforts are directed toward space-based slitless spectroscopy and ground-based adaptive optics, these studies are generally limited to smaller samples owing to the need for long integration times. We presents an affordable alternative to tackle this problem. We use an image deconvolution algorithm (finite resolution deconvolution) to obtain higher resolution in ground-based images of the Cosmic Evolution Survey field. One major advantage of using deconvolution is the ability to perform resolved studies for a substantially larger sample of galaxies. In this study, we model the 14-band deconvolved optical + near-IR spectral energy distribution to provide resolved color and stellar population maps for a sample of 22960 star-forming galaxies at $0.5 < z < 2$. These galaxies are selected based on their rest-frame ($U - V$) and ($V - J$) colors, with stellar mass greater than $10^{9.8} M_{\odot}$, and an integrated S/N greater than 20 in the K_s band. Star-forming galaxies are classified as clumpy if its clumps contribute to at least 8% of the total luminosities or stellar mass. When clumps are detected based on the U_{rest} luminosity map, the fraction of clumpy galaxies decreases slightly from ~ 0.65 at $z \sim 1.8$ to ~ 0.55 at $z \sim 0.8$. We also find that the clumpy fraction is dependent on the stellar mass of the host galaxy, with lower fractions for massive galaxies. More than 80% of SFGs are observed to be clumpy in both color and stellar mass distributions at $z > 1.5$, but decreases to $\sim 70\%$ at $z \sim 0.8$. We suggest that if galaxies that are clumpy in stellar mass distribution are taken as a proxy for mergers, this result implies that not all mergers play a significant role in clump formation.

Acknowledgements

It certainly is a daunting task to write a dissertation for a Master of Science, and it wouldn't have been possible to complete it in two years (plus a few months, but who is really counting) without the help and support of so many people throughout this period. If I was to list out each item that every one of you helped me with, this dissertation would be stupendously long. Therefore, while the acknowledgements are kept short, know that they go beyond what are written below. I will always cherish every moment with each of you, and I would give anything to relive them again.

The foremost acknowledgement goes to no one other than the boss himself, Adam. I cannot ignore the fact that I would not have continued in astronomy had you not reached out and persuaded me to stay. Thank you for being so patient throughout the years and for creating so many opportunities for me.

To Cemile and Leo, for dealing with my questions when I was too scared to bug Adam.

To Vivian, for being the best office mate in the world.

To Nicky, for continuously bugging me to pursue my PhD studies.

To Paul, for the numerous adventures at all-you-can-eat sushi and Tuesday wings.

To my parent, for their unconditional love and support! Although more specifically, for providing me a roof to live under, in a time when the housing market in Toronto is broken.

To members of the #swegastrophysicists group; specifically, Cassandra, Abhinav and Darren. My undergraduate experience would be a completely different story if it weren't for all of you.

To my past undergraduate supervisors, Dylan and Chris, for your guidance.

To Dennis, Shiranka and Nicky, for taking the time to read this thesis.

And to every else who has not been named (you all know who you are) - thank you for believing in me! And no, just because I have an MSc in astronomy, it does not mean that I'm going to space.

At last, it is time for me to show you what you have been waiting for years. Allow me to take you on a journey through the Universe to worlds unknown.

*To undergraduate Visal,
way to go my dude.*

Table of Contents

Abstract	ii
Acknowledgements	iii
Table of Contents	v
List of Tables	vii
List of Figures	viii
1 Introduction	1
1.1 A Brief Introduction to Extragalactic Astronomy	2
1.2 The Cosmic Star-Forming History	3
1.3 The Stellar Mass Assembly of Galaxies	4
1.4 The Evolution of Galaxy Morphologies	5
1.5 On the Nature of Clumpy Star-Forming Galaxies	7
1.5.1 Recent Observational and Theoretical Studies	7
1.6 Motivation and Outline	8
2 Data Overview	11
2.1 The Cosmic Evolution Survey Field	11
2.1.1 HST Ancillary Data	12
2.2 COSMOS/UltraVISTA Survey and Catalog	12
2.3 Photometric Data	13
2.4 Galaxy Sample	14
2.4.1 Limiting S/N for Image Deconvolution	14
2.4.2 Star-Forming Galaxies Definition	16
2.5 Summary of the Data	17
3 Image Deconvolution	19
3.1 Brief Introduction to Deconvolution	20
3.1.1 Finite Resolution Deconvolution	20
3.2 Deconvolution in Practice	21
3.2.1 Constructing the Deconvolution Kernel	23
3.3 Validation of Deconvolution using Space-Based Data	26
3.3.1 Comparison with the F814W Data	26
3.3.2 Multi-Wavelength Comparison	28
3.4 Summary of Image Deconvolution	31

4	Methodology	32
4.1	Segmentation Maps	32
4.2	Misaligned Astrometry	33
4.3	Pixel Binning	33
4.4	Resolved Spectral Energy Distribution Modeling	35
4.5	Clumpy Structures Analyses	35
4.5.1	Normalized Color and Stellar Mass Profiles	36
4.5.2	Examples of Normalized Profiles	36
4.5.3	Classification Scheme for Clumpy Structures	37
4.6	Summary of Methodology	38
5	Results	46
5.1	The Clumpy Fractions	46
5.1.1	Evolution of f_{clumpy}	47
5.1.2	Comparison to Other Studies based on HST Imaging	49
5.2	The Star-Forming Main Sequence of Clumpy Galaxies	50
5.3	Summary of the Results	51
6	Discussion	53
6.1	Evolution of Clumpy SFGs	53
6.2	Connecting High- z Galaxies to Low- z Galaxies	54
6.3	The Role of Mergers in the Formation of Clumpy SFGs	55
6.4	Possible Biases in Different f_{clumpy} Measurements	58
6.5	Summary of the Discussion	59
7	Conclusions	60
7.1	Future Directions	62
7.2	Final Words	63
	Bibliography	64

List of Tables

2.1	Summary of Photometric Data	14
5.1	Values of the Fit for the Clumpy Fraction Evolution	47

List of Figures

1.1	The Cosmic Star Formation Rate Density	3
1.2	The Stellar Mass Density Evolution	4
1.3	The Hubble Tuning Fork	6
1.4	The Hubble Sequence in Relation to the Age of the Universe	6
2.1	K_s S/N of Galaxies Binned by Stellar Mass	15
2.2	The UVJ Diagram and the Star-forming Main-Sequence	17
3.1	The spatial Variation in the FWHM seeing in the COSMOS data	22
3.2	Analytical Residuals	23
3.3	Numerical Residuals	24
3.4	Examples of Deconvolving z+-Band Images	27
3.5	Examples of Multi-Wavelength Deconvolution	29
3.5	Same as above.	30
4.1	Examples of the Voronoi Bins	34
4.2	Examples of Normalized Profiles	39
4.2	An example of how the normalized profiles are used to classify the morphology of galaxies. The galaxy is shown mainly for its clumpy morphology. Note that the galaxy is defined as clumpy in the rest-frame U luminosity, however its morphology is not clumpy in the rest-frame V luminosity since its clumpy components contribute less than 8% of the total rest-frame V luminosity.	40
4.2	Another example of how the normalized profiles are used to classify the morphology of galaxies. The galaxy is shown, again, mainly for its clumpy morphology. Similar to ID240419, the galaxy is defined as clumpy in the rest-frame U luminosity, however its morphology is not clumpy in the rest-frame V luminosity.	41

4.2	Another example of how the normalized profiles are used to classify the morphology of galaxies. The galaxy is shown, again, mainly for its clumpy morphology. For this galaxy, its morphology is clumpy in all the rest-frame luminosity and stellar mass distribution maps. Interestingly, its clumpy components in the stellar mass distribution map do not correspond to the clumps identified based on the rest-frame luminosities.	42
4.2	An example of the normalized profiles for non-clumpy star-forming galaxies. In this case, the galaxy has smooth light and mass profiles, which are shown in the normalized profiles. The normalized surface brightness and surface mass density fall off with further distance from the mass-weighted center.	43
4.2	Another example of the normalized profiles for non-clumpy star-forming galaxies. Similar to ID123057, its light and mass profiles are smoother, which can be seen within the normalized profiles. As such, the galaxy has been labeled as non-clumpy.	44
5.1	The Clumpy Fractions for SFGs at $0.5 < z < 2$	48
5.2	Comparison of $f_{\text{clumpy}}^{U_{\text{rest}}}$ to Other Studies	49
5.3	The Morphology of Galaxies with Relation to the Main-Sequence Star Formation . .	51
6.1	The Evolution of the Clumpy Fractions With the Evolution of Galaxies	54
6.2	Examples of Galaxies that are Clumpy in its Stellar Mass Distribution	56
6.3	The Fraction of Clumpy Fraction in Both Luminosity and Mass	57

Chapter 1

Introduction

The origin and evolution of galaxies are among the most intriguing and complex chapters in the formation of cosmic structure. Endeavoring to address these enigmatic topics, astronomers have surveyed the night sky using the most advanced technologies at their disposal. Wide-field surveys such as the Sloan Digital Sky Survey have probed millions of nearby galaxies, sampling diverse populations in different environments (e.g. Kauffmann et al. 2004; Baldry et al. 2006). At the other end, deep-field surveys with space telescopes such as the *Hubble Space Telescope* and *Spitzer Space Telescope* have confirmed galaxies as far back as $z = 11.1$ (Oesch et al., 2016), and have provided hundreds more candidates at $z > 7$ (e.g. Bouwens et al. 2010; McLeod et al. 2015).

Even with the avalanche of remarkable measurements of galaxy properties over the majority of cosmic history, putting forward a coherent explanation of how distant galaxies evolve to be present-day spiral and elliptical galaxies still remains one of the great challenges in astronomy. The primary challenge lies mainly in the observational difficulties associated with tracking evolving populations of galaxies across cosmic time. Ideally, the in-depth understanding of galaxy evolution would encompass the sequence of events from the first stars to the diverse populations of galaxies we have presently. While this is a very daunting task to embark on, this dissertation aims to present a unique and resolved approach that will provide some insights onto a small, yet crucial part of this evolution.

The following sections summarize the current understanding of galaxy formation and evolution, particularly focusing on the cosmic star-forming history and its implications on galaxy evolution. We highlight the importance of compact star-forming regions in distant galaxies, and the roles they have in shaping the evolution of galaxies. In the final sections, we address the limitations in resolving distant galaxies, and outline the approach we take to progress our understanding in the field of galaxy formation and evolution.

1.1 A Brief Introduction to Extragalactic Astronomy

This section provides a brief overview of the astronomical tools and techniques used to infer galaxy properties. Measuring fundamental properties such as stellar masses and star formation rates requires observations of galaxies at various wavelengths. For example, the rest-frame ultraviolet (UV) and several nebular emission lines (such as H α and [OII]) are useful diagnostics of the star formation rates in the absence of dust. In general, these luminosities are linearly related to a star formation rate by some conversion factors, which we denote as κ . Similarly, near-infrared (NIR) and mid-infrared (MIR) observations are crucial for deriving stellar masses. In addition to stars and gas, galaxies are made up of various metal abundances and dust. Dust particles absorb UV radiation and re-emit it at longer wavelengths, causing the attenuation of the shorter wavelength light. As such, the far-infrared (FIR) emission of galaxies can be used to measure the re-emitted star formation rate due to dust.

Furthermore, the wavelength of the emitted radiation can be lengthened due to the expansion of the Universe. This effect can be parametrized as,

$$z = \frac{\lambda_{\text{obs}} - \lambda_{\text{rest}}}{\lambda_{\text{rest}}}, \quad (1.1)$$

where λ_{rest} is the emitted wavelength, λ_{obs} is the observed wavelength, and z is the cosmological redshift. Since the Universe is expanding, distant galaxies are moving away from us, and the farther away they are from us, the faster they move away from us. This results in their emitting light to be redshifted. Therefore, UV radiation from distant star-forming regions will be lengthened by the time it reaches the earth, and will be observed as a longer wavelength radiation.

The properties of galaxies and their underlying stellar populations are therefore encoded within their spectral energy distributions (SEDs). To construct the SEDs of galaxies, astronomers observe galaxies at various wavelengths. There are distinct software routines that utilize stellar population synthesis models to derive various properties from SEDs (e.g. FAST, Kriek et al. 2009). While existing models can still be imperfect, astronomers have made significant progress in further developing and improving these population synthesis models. Other software routines such as EAZY (Brammer et al., 2008) enable astronomers to estimate the redshift of extragalactic objects from the SEDs (redshift derived this way is known as the photometric redshift), and the observed rest-frame luminosity for specific filters.

Finally, the first step in the scientific analysis of extragalactic astronomy is to identify objects within the data. The **SExtractor** package (Bertin & Arnouts, 1996) is one of the the main tools for astronomers to reliably extract sources within their images. Being able to identify individual objects within an image allows astronomers to perform aperture photometry, a process in which astronomers measure the flux that falls within a circular aperture centered around an object. Knowing the fluxes of an object in different bands therefore enables them to infer the stellar properties of this object from SED modeling.

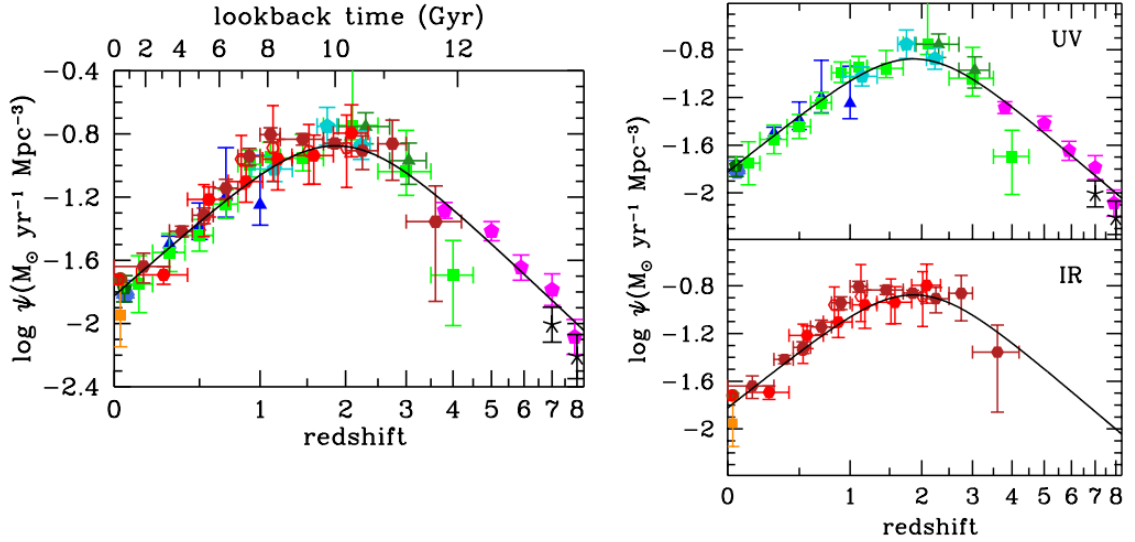


Figure 1.1: The cosmic star formation rate density as derived by Madau & Dickinson (2014). The top (bottom) right panel shows the SFRD derived from the UV (IR) rest-frame measurements, while the left panel shows the total SFRD derived from the UV+IR rest-frame measurements. The black solid line shows the best-fitting function. The colors denote the different surveys used to obtain those measurements.

1.2 The Cosmic Star-Forming History

One of the major accomplishments that came with the surge of astronomical data is the determination of the evolving star-forming history. The cosmic star formation rate density (SFRD) provides a sensitive probe of galaxy formation and evolution as it tells us the rate at which the Universe was forming stars per unit volume over time.

The earliest estimates of the SFRD showed a steep decline from $z \sim 1$ toward the present-day, suggesting that the Universe was more active in terms of star formation during its earliest days. A more recent estimate of the cosmic SFRD was presented in Madau & Dickinson (2014), where they based their modeling on a number of contemporary galaxy surveys that probed a range of redshifts. These surveys had provided good measurements of the UV and IR luminosity functions. The “observed” UV and IR star formation rate densities are inferred by multiplying the luminosity densities by their respective conversion factors, κ_{UV} and κ_{IR} . Figure 1.1 shows the derived cosmic SFRD from UV+IR rest-frame measurements, after correcting for dust attenuation, along with the SFRD based on the individual UV and IR rest-frame measurements. The best-fitting parameterization for the cosmic SFRD is,

$$\psi(z) = 0.015 \frac{(1+z)^{2.7}}{1 + [(1+z)/2.9]^{5.6}} \text{ M}_\odot \text{ yr}^{-1} \text{ Mpc}^{-3} \quad (1.2)$$

The findings of these different surveys have painted a consistent picture of the star formation

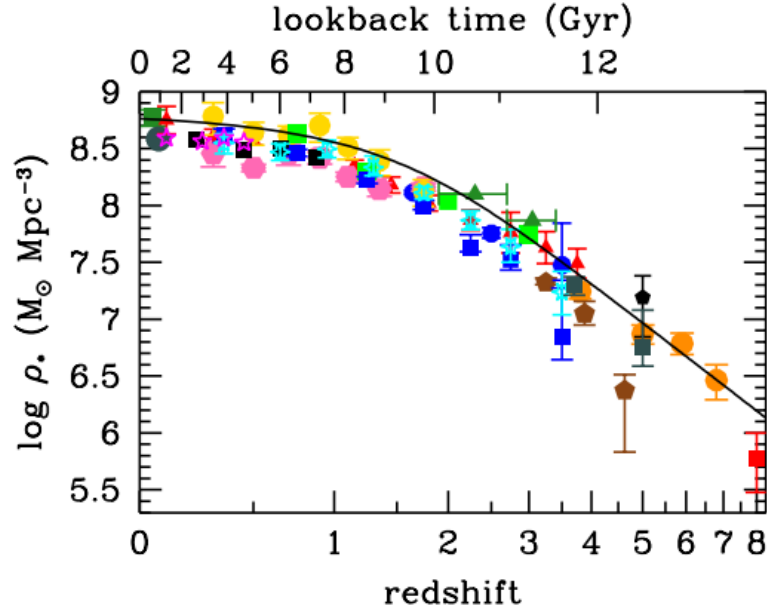


Figure 1.2: The evolution of the stellar mass density as a function of redshift as shown in Madau & Dickinson (2014). The data points are recent measurements of the stellar mass density as a function of redshift, while the solid black curve is obtained by integrating the best-fitting SFRD (Equation 1.2) and accounting for the mass loss during stellar evolution.

history (SFH) of the Universe: a rising phase of star formation between $3 < z < 8$, an epoch of peak cosmic star formation at around $z \sim 2$, followed by gradual decline afterward. By integrating the instantaneous SFH over redshift and correcting for mass loss during stellar evolution (due to stellar winds, or supernovae explosions), a prediction of the stellar mass density can be made (shown in Figure 1.2). In fact, the predicted stellar mass density history implies that the bulk of the stellar mass in the local universe ($> 75\%$) actually formed during the epoch of peak cosmic star formation, with only 8% formed before that period (Madau & Dickinson, 2014).

Even though we now have this impressive measurement of when most of the stellar mass was created, the underlying physics governing how galaxies build up their stellar mass and why the Universe was more active in the past is still not fully understood. Indeed, it is intriguing to ask which mechanisms sustained the high star formation rate at $z \sim 2$ in distant galaxies. By observing galaxies during the epoch of cosmic star formation, we can better understand the mechanisms behind the progression of the SFRD from that epoch to that of the present-day.

1.3 The Stellar Mass Assembly of Galaxies

In cosmological models, approximately 85% of the matter in the Universe is made of dark matter. In the context of structure formation, dark matter forms the backbone from which galaxies form,

evolve, and merge. In this sense, galaxies grow in a hierarchical process; through accreting smaller systems composed of both dark matter and baryons. This process is controlled by the nature of dark matter itself and the initial density fluctuations. The assembly of the stellar contents within galaxies is further governed by more complex baryonic physics, including the gaseous dissipation inside the evolving dark matter halos, the physical mechanisms behind star formation, the chemical enrichment on the galactic and intergalactic scales, and the role of feedback (i.e. stellar energetic output from supernovae, or active galactic nuclei) in regulating star formation.

The growth of stellar mass within galaxies can be summarized through (1) *ex-situ* processes such as the accretion of small satellites and tidal debris or galaxy mergers, and/or (2) *in-situ* processes such as local star formation that is fueled by existing and infalling gas. The importance of mergers and internal processes in driving the growth of stellar components within galaxies is still an ongoing topic of debate in the literature. There is a growing consensus that *in-situ* processes dominate at higher redshifts and *ex-situ* processes at lower redshifts. This can be seen by comparing the star formation rate and stellar mass density plot (Figure 1.1 and 1.2), where the integrated stellar mass density continues to rise steadily even after star formation rates peak at $z \sim 2$. It should be noted however that the distinctions between the two processes are generally not clear as local star formation can be induced through both galaxy interaction and mergers.

1.4 The Evolution of Galaxy Morphologies

One of the fundamental ways in which galaxy properties are described is through the morphology of galaxies. Early works to classify nearby galaxy morphologies resulted in the most commonly known classification scheme, the ‘‘Hubble Tuning Fork’’ (Hubble 1936; Sandage 1961, see Figure 1.4). The basic Hubble sequence consists of two main types; spiral and elliptical, while a further division is made for spirals into those with and without bar-like structures. The basic structures in distant galaxies were more difficult to characterize due to the limitation of existing facilities to resolve these galaxies in the same manner as nearby galaxies.

It was not until the 1990s when the *Hubble Space Telescope* was launched and its various ‘‘deep field’’ images (Williams et al. 1996, Volonteri et al. 2000; Beckwith et al. 2006) were released that astronomers had a clearer picture of what the distant Universe looked like (e.g. Abraham et al. 1996; van den Bergh et al. 1996). Now, we are able to resolve galaxies at $z > 1$ with space-based observatories, and innovative technologies such as adaptive optics on ground-based observatories (Genzel et al. 2006). Galaxies in the distant Universe are significantly different, in terms of morphologies, compared to what they are today. Figure 1.4 shows snapshots of the evolving morphologies with respect to the age of the universe. The local Universe consists of mainly spirals and ellipticals, while higher redshifts are dominated by galaxies with a peculiar morphology. This preponderance of irregular morphologies is not an effect of a shift in the rest-wavelength of the observations, as

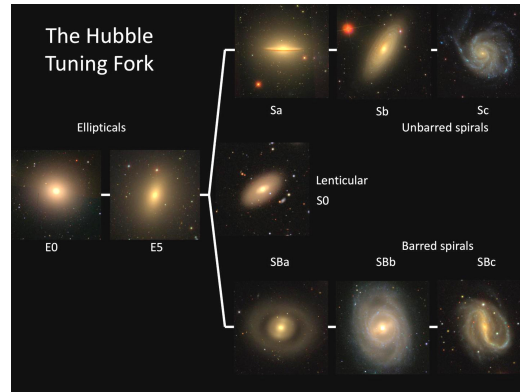


Figure 1.3: The Hubble Tuning Fork illustrated with images of nearby galaxies from the Sloan Digital Sky Survey.

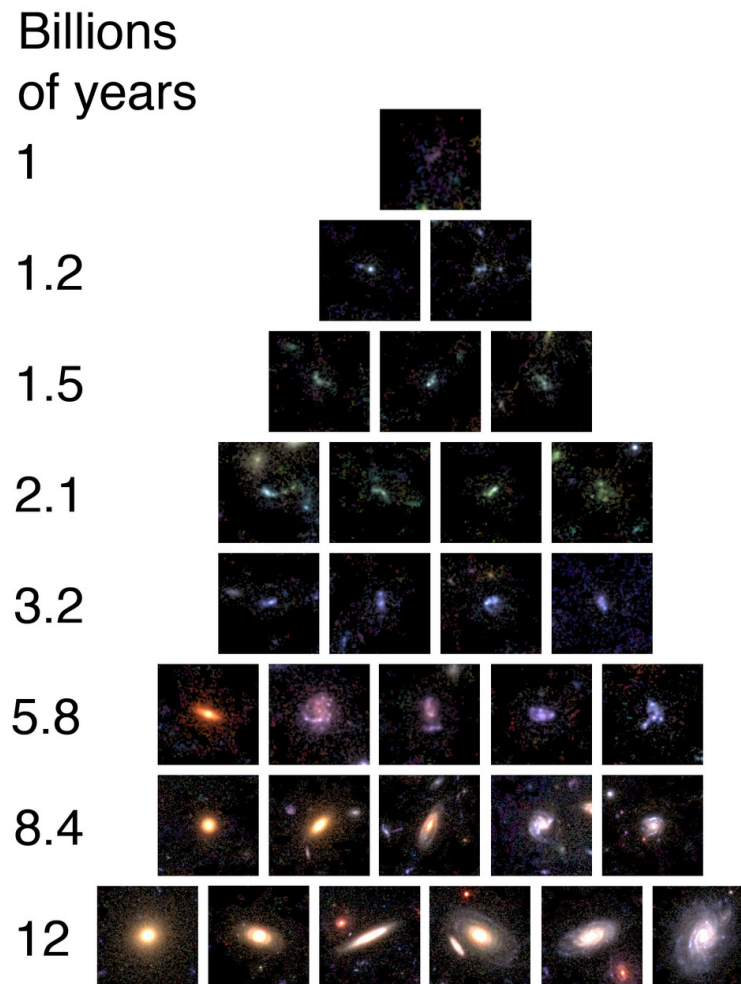


Figure 1.4: Snapshots of galaxies in relation to the age of the universe. In the distant Universe, galaxies are smaller and more peculiar, while nearby galaxies are typically spirals and ellipticals. Image taken from the Cosmic Evolution Survey webpage.

irregularities are observed to persist in both the rest-frame UV and optical images (e.g. Dickinson 2000). A common feature that characterizes these irregular galaxies are clump-like structures that are observed in the rest-frame UV and optical. These structures have been studied for both field and lensed galaxies, with a variety of multi-wavelength data that include the rest-frame UV and optical data, emission line maps, CO observations (e.g. Elmegreen & Elmegreen 2005; Elmegreen et al. 2007; Elmegreen et al. 2009a; Elmegreen et al. 2009b; Wuyts et al. 2012; Murata et al. 2014; Livermore et al. 2015; Guo et al. 2018; Shibuya et al. 2016; Cava et al. 2018; Zanella et al. 2019). While there is no formal definition for clumpy galaxies, compact star-forming structures in distant galaxies are generally dubbed as “clumps”, and their host galaxies as “clumpy galaxies”.

1.5 On the Nature of Clumpy Star-Forming Galaxies

The physical sizes of star-forming clumps are not well constrained due to the limiting resolution of our facilities. Size estimates can vary from tens of parsecs to a few kiloparsecs based on observations at $z \sim 1 - 4$ (e.g. Livermore et al. 2015; Soto et al. 2017; Cava et al. 2018). At these scales, even the *Hubble Space Telescope* can only marginally resolve these structures. Clumps are observed to have enhanced blue optical-UV colors and specific star formation rates (e.g. Wuyts et al. 2012, Wuyts et al. 2013, Hemmati et al. 2014). Indeed, clumpy structures are detected in high-resolution observations of H α emission line maps (e.g. Wuyts et al. 2013, Mieda et al. 2016), suggesting that they are compact, star-forming regions.

1.5.1 Recent Observational and Theoretical Studies

Interestingly, astronomical surveys during the epoch of cosmic star formation ($z \sim 2$) reveal that irregular and clumpy galaxies outnumber normal types, with percentages as high as 60% for star-forming galaxies (e.g. Wuyts et al. 2012, Guo et al. 2015). Shibuya et al. (2016) reported that the evolution in the fraction of clumpy galaxies over cosmic time broadly follows the trend of the Madau & Dickinson’s star formation history plot, with the clumpy fraction peaking at around $z \sim 2 - 3$.

Despite their ubiquity at high- z , the origin and evolution of clumpy star-forming galaxies are not well constrained by observational studies due to the limited instruments that can resolve them. As a result, their formation and evolution can be explained within a wide range of theoretical models. Theories suggest that the formation mechanisms of star-forming clumps are associated with both *in-situ* and *ex-situ* origins. In the nearby Universe, such irregular morphologies are attributed to galaxy interactions and mergers. These same physical processes can be used to explain the irregular morphologies at larger lookback time. In this context, star-forming clumps are induced from the perturbation and collapse of gas due to various gravitational interactions. This view is supported by some observational studies (e.g. Guo et al. 2015). It is also not clear whether clumps are just remnants of accreted satellites which have not been tidally disrupted (Zanella et al., 2019).

While mergers are undoubtedly taking place at high redshifts, only a minority of high-redshift galaxies are reported to be in the process of merging, with pair/merger fractions ranging from a few to 25% (e.g. Lotz et al. 2011, Man et al. 2016, Mantha et al. 2018). Further, the gas-phase kinematics of most high- z galaxies is dominated by ordered disk rotation (e.g. Genzel et al. 2006; Förster Schreiber et al. 2011; Stott et al. 2016), even for those with irregular morphologies, suggesting that these morphologies can not be the result of recent mergers. If mergers play a minimal part in creating clumpy SFGs, then another mechanism must be responsible. Indeed, observations of typical SFGs between $z \sim 0 - 2$ show that their molecular gas mass fractions steeply rise with redshift (e.g. Tacconi et al. 2010). If the gas reservoir in these galaxies is being used up for star formation, then a continuous fueling is needed in order to sustain the observed high star formation rate. A widely invoked theoretical framework to explain star-forming clumps is the continuous replenishment of the gas reservoir within these galaxies through cold, filamentary streams. Such gas-rich, turbulent disks are likely to gravitationally collapse at the kiloparsec-scale, causing the formation of star-forming clumps (Dekel et al., 2009).

The fate of clumps is often debated in the literature. Simulations are inconclusive, while observational studies lack the statistical significance to constrain specific scenarios. In one scenario, clumps can remain as bound systems, surviving stellar feedback for ≥ 500 Myr. In this case, clumps are expected to migrate inward due to dynamical friction and gravitational torques, and coalesce and contribute to the stellar growth of the progenitor of present day galactic bulges (e.g. Bournaud 2016, Mandelker et al. 2014 2017). In the other scenario, clumps are believed to be short-lived phenomena, on the time-scale of ≤ 50 Myr, where strong stellar feedback and/or tidal forces disperse the gas and unbind the stellar system. Differentiating the two scenarios requires information on the resolved stellar populations of clumps.

1.6 Motivation and Outline

Understanding the formation and evolution of clumps is important, not only for studying the mechanism driving the growth of bulges and thick disks, but also to test models on the interstellar medium and stellar feedback, and to investigate which models can correctly reproduce observational results at the sub-galactic scales of clumps (e.g. Inoue & Yoshida 2019). Furthermore, star-forming clumps act as important laboratories to determine what is the dominant mode of star formation. These studies enable us to test and constrain how galaxies assemble their mass over time (whether through mergers, and/or secular evolution), and how star formation within galaxies proceeds with redshift.

However, in order to investigate the nature of star-forming clumps, high resolution and multi-wavelength data are needed to resolve these regions and to accurately measure their physical properties respectively. At the present, the *Hubble Space Telescope* (HST) is the only telescope capable of providing such data. While HST has now been in service for approximately three decades, there

are actually only a few existing fields with truly deep and multi-wavelength imaging in more than a handful of filters (e.g. the Cosmic Assembly Near-Infrared Deep Extragalactic Legacy Survey, or CANDELS; Grogin et al. 2011, Koekemoer et al. 2011). CANDELS is a survey of five fields, which consist of two deep fields centered on the Great Observatories Origins Deep Survey (GOODS) north and south fields, and three wide fields. These fields only cover a small portion of the sky, with the deep fields spanning ~ 130 square arcminutes, thus the number of clumpy SFGs observed in these fields are limited (e.g. Wuyts et al. (2012) presented arguably the most in-depth study of the resolved stellar populations for ~ 700 distant SFGs in GOODS-South). Of course, new data such as the Hubble Frontier Field (HFF) is becoming available and represents an exciting opportunity to do resolved stellar population studies of the distant Universe. The full multi-wavelength coverage of the HFF, however, only extends to ~ 60 square arcminutes. Additionally, the amount of future data that will be comparable to CANDELS and HFF remains small.

The unrivaled image quality of space-based observatories makes them ideal for observing star-forming clumps. However, larger cameras on ground-based observatories can take advantage of the large field of view of these telescopes, allowing them to survey larger regions of the sky. Ground-based observatories also have access to more photometric filters compared to their space-based counterparts. However, these observatories are subjected to light pollution and atmospheric turbulence. The turbulence nature of the atmosphere smears images and effectively degrades their image quality, rendering these images to limited use for resolved studies of galaxies. Image deconvolution has often been explored as a solution to reverse the smearing effect and to improve the angular resolution. In fact, it has been recently shown that it is possible to achieve close to space-based resolutions in deconvolved ground-based images (Cantale et al. 2016b).

The new algorithm, finite resolution deconvolution (FIREDEC, Cantale et al. 2016a), has two main features that are advantageous compared to past deconvolution algorithms. (1) FIREDEC deconvolves to a finite resolution as opposed to completely removing the point spread function, ensuring that solutions are well-sampled and constrained, and (2) FIREDEC introduces a new method of characterizing noise, which allows the algorithm to better distinguish signal from noise. We present the deconvolved and resolved stellar properties of high- z ($0.5 < z < 2$) galaxies within the Cosmic Evolution Survey (COSMOS) field. Ground-based images are deconvolved with FIREDEC to the target resolution of $0.1''$ so that star-forming clumps can be resolved at our given redshift range. FIREDEC is ideal for this analysis as Cantale et al. (2016b) have previously shown that this target resolution is attainable. The COSMOS field covers an area of a 2 square degrees (or 7200 square arcminutes), with arguably the most impressive array of multi-wavelength coverage (30+ photometric bands). In comparison, the CANDELS/Deep survey covers 130 square arcminutes within the GOODS-N and GOODS-S, and has been observed in at most 10 photometric bands. In fact, 55 CANDELS/Deep fields can fit into one COSMOS field! Deconvolving the COSMOS field presents an exciting and unique opportunity to study a larger sample of galaxies over a larger volume

of the sky. At its fullest potential, this study can provide an unprecedented catalog of resolved stellar population maps for hundreds of thousands of galaxies.

In the following chapter, we review the photometric data of COSMOS and the selection process for galaxies within this study. Chapter 3 introduces the basic concepts of image deconvolution and FIREDEC. We also provide some examples of deconvolved ground-based images and compare them to the respective HST imaging. The techniques used to identify clumpy structures are presented in Chapter 4. Finally, the remaining chapters present the results, specifically focusing on the evolution of the fraction of clumpy galaxies with redshift, and the implications on the formation and evolution of clumps.

We adopt the following cosmological parameters $\Omega_M = 0.3$, $\Omega_\Lambda = 0.7$, and $H_o = 70 \text{ km s}^{-1} \text{ Mpc}^{-1}$. The cosmological parameters describe the properties of the Universe, where Ω_M and Ω_Λ is the mass and dark energy density respectively, and H_o is the Hubble constant. All magnitudes are quoted in the AB magnitude system.

Chapter 2

Data Overview

“The science is only as good as the data.”

Adam Muzzin

This chapter gives an overview of the Cosmic Evolution Survey, hereafter COSMOS. This includes observations made with the Subaru and VISTA telescopes, as well as the partial imaging of the field with the *Hubble Space Telescope*. The chapter provides an explanation for how galaxies are selected from the COSMOS/UltraVISTA catalog, and provides the definition for star-forming galaxies.

2.1 The Cosmic Evolution Survey Field

The Cosmic Evolution Survey field is roughly 2 square degrees, and is centered at RA=10:00:28.6, DEC=+02:12:21.0 (J2000) near the celestial equator. This location ensures visibility by all astronomical facilities, especially with the expected arrival of next-generation 20-30 meter optical and infrared telescopes.

The main goal of COSMOS is to address the evolution of galaxies in the context of their large-scale structure, star formation, and active galactic nuclei (AGN) out to moderate redshift. As observations and data of the field continue to grow over the past decade, COSMOS has arguably the most impressive array of multi-wavelength coverage, spanning from: X-ray observations with *XMM-Newton* and *Chandra* (Hasinger et al. 2007; Elvis et al. 2009), UV observations with *GALEX* (Martin et al., 2005), extensive optical observations with the CFHT and Subaru telescopes (Taniguchi et al. 2007; Taniguchi et al. 2015; Capak et al. 2007), mid-infrared observations with *Spitzer* (Sanders et al., 2007), submillimeter observations with *Herschel* (Oliver et al., 2012), millimeter observations with the AzTEC and MAMBO instruments (Scott et al. 2008; Aretxaga et al. 2011), and radio observations with the VLA (Schinnerer et al., 2007).

The large areal coverage of COSMOS is needed to properly sample large-scale structure as smaller volumes are subjected to cosmic variance, which can affect measurements of the abundances and

types of galaxies. On the other hand, the full spectral coverage enables astronomers to probe the coupled evolution of young and old stellar populations, starbursts, the interstellar medium, AGN, and dark matter. Further, the multi-wavelength coverage is necessitated by the fact that light from different epochs is differently redshifted, and the presence of dust obscuration around star-forming regions can absorb UV light and re-emit it at longer wavelength.

2.1.1 HST Ancillary Data

In addition to the extensive multi-wavelength coverage of ground-based observatories, COSMOS was observed with the Advanced Camera for Surveys (ACS) on board HST. Details of the observations and reductions are provided in Koekemoer et al. (2007) and Massey et al. (2010). Briefly, 581 orbits were devoted to imaging the full field in the F814W filter. A smaller section of roughly 10 square arcminute, centered on the field, was imaged using the F475W filter in 9 orbits.

The field was further observed as part of the Cosmic Assembly Near-infrared Deep Extragalactic Legacy Survey (CANDELS; Grogin et al. 2011, Koekemoer et al. 2011). The CANDELS program consists of five distinct fields at two distinct depths, with the deep portion of the survey known as CANDELS/Deep and the wide portion as CANDELS/Wide. While CANDELS/Wide has exposures in all five field, one of its primary Wide fields is COSMOS. The COSMOS observations consisted of a contiguous mosaic of overlapping 4x11 ACS/WFC V_{606} tiles (of roughly 8x23 arcminutes) that run north-to-south at a position angle of 180° . Further, we obtain HST H_{160} imaging from the COSMOS-Drift and SHift survey (COSMOS-DASH). Details of the survey and observing techniques are presented in Mowla et al. (2019) and Momcheva et al. (2017). The survey takes advantage of the unique Drift And SHift (DASH) observing mode, allowing COSMOS-DASH to be the widest HST/WFC3 imaging survey with the F160W filter.

2.2 COSMOS/UltraVISTA Survey and Catalog

At the time it was released, the UltraVISTA survey (McCracken et al., 2012) was one of the most notable near-infrared surveys. The main strength of UltraVISTA lies with the fact that the field is directly centered on the COSMOS field. UltraVISTA has imaging in four broad-band NIR filters ($YJHK_s$). It is the deepest of the VISTA public surveys, with the latest data release reaching a magnitude depth of $K_s \sim 25.5$. With the combination of optical imaging from the COSMOS field, UltraVISTA presents a unique opportunity for astronomers to investigate the growth of galaxies during the crucial redshift range $1 < z < 3$.

In fact, Muzzin et al. (2013) already published a photometric catalog that exploited the combined COSMOS and UltraVISTA multi-wavelength observations, spanning the wavelength range between 0.15 to $24 \mu\text{m}$. Briefly summarized, source detection and photometry were performed using SExtractor based on the K_s -band imaging. The catalog made use of the PSF-matched photometry

in the 30 photometric bands, providing the photometric redshifts, stellar population parameters (e.g. stellar masses and star formation rates), along with information of the rest-frame ($U - V$) and ($V - J$) colors, and UV/IR luminosities for all the galaxies within the field. The high image quality of the UltraVISTA K_s -band allows for the selection of mass-complete galaxy sample up to $z = 4$.

Due to deep, multi-wavelength observations and large areal coverage, COSMOS/UltraVISTA serves as an attractive field to study the evolution of galaxies. Along with existing HST imaging of the field in certain filters, COSMOS/UltraVISTA provides an ideal ground-based database on which to apply deconvolution techniques to resolve clumpy structures.

2.3 Photometric Data

We choose not to utilize all the existing ground-based imaging of the COSMOS field since image qualities between these photometric data are not homogeneous. The variation in image qualities is the result of differences in observing conditions, which vary from pointing-to-pointing. In theory, since FIREDEC can be set to obtain a similar angular resolution in all deconvolved images, it is possible that the variation in image qualities will have little to no effect on our analysis. However, image deconvolution is not magic; the result of deconvolution is partly dependent on the original image quality (e.g. the angular resolution of the image). In terms of Fourier analysis, retrieving higher angular resolution with image deconvolution means retrieving higher Fourier frequencies. Since the only limit we have on the frequency components of an arbitrary image is its point spread function, the smoother this point spread function is (i.e. the larger the full-width at half-maximum, FWHM, is), the more difficult it is to constrain higher spatial components in deconvolution.

This presents a complication for the analysis. Using non-homogeneous data can result in images of varying resolution. It is important that all our photometric data cover the same physical region, so that the correct stellar properties can be inferred at the resolved scale. One simple approach to deal with mismatched image qualities is to use only the photometric data that have fairly homogeneous image quality. The seeing variations for all the photometric data are summarized in Muzzin et al. (2013), where seeing can range from 0.53" to 1.20". We opt not to use the $g+$ filter of the Subaru/SuprimeCam as the photometric data have the worst seeing compared to the others (1.01" to 1.20"). We also omit the $i+$ -band data as its long integration time caused most stars to be saturated and unusable for modeling the point spread function. Included in the analysis of this study are the B_jV_jr+z+ data from the Subaru/SuprimeCam. We have also included 6 optical medium bands ($IA484, IA527, IA624, IA738, IB427, IB505$). We omit the other medium band optical data of the COSMOS field as these data either have bad seeing, or a large range in seeing. Finally, we include the four near-infrared bands, $YJHK_s$ from the UltraVISTA survey. Table 2.1 summarizes the seeing of the each data and their respective papers.

Filter	Seeing (")	Reference
(1)	(2)	(3)
B_j	0.71 - 0.78	Capak et al. (2007)
V_j	0.74 - 0.84	-
$r+$	0.78 - 0.85	-
$z+$	0.81 - 0.91	-
$IA484$	0.54 - 0.72	-
$IA527$	0.59 - 0.67	-
$IA624$	0.70 - 0.81	-
$IA738$	0.72 - 0.80	-
$IB427$	0.66 - 0.75	-
$IB505$	0.71 - 0.84	-
Y	0.82 - 0.86	McCracken et al. (2012)
J	0.81 - 0.85	-
H	0.78 - 0.82	-
K_s	0.77 - 0.82	-

Table 2.1: Summary of the photometric data selected to be processed with deconvolution. While image deconvolution is used to obtain better resolution, the achieved resolution is limited by the original image quality (see text for more information). To ensure that deconvolved images have the same resolution, not all the photometric data of the COSMOS field are used, but instead only images which have comparable seeing are used within this study. The seeing information of all the photometric data is shown in Muzzin et al. (2013).

2.4 Galaxy Sample

This study makes use of the K_s -selected catalog from Muzzin et al. (2013) to select galaxies. The parent galaxy sample is obtained by using the flag, “use=1”, in the catalog. Essentially, this excludes objects that are flagged as stars based on a color-color cut, objects that are badly contaminated by nearby bright stars, and objects that contain bad regions. The total number of galaxies in the parent sample is 160,070. In the following section, we discuss the selection criteria for suitable galaxies.

2.4.1 Limiting S/N for Image Deconvolution

Image deconvolution is reviewed in Chapter 3, however we briefly describe some key concepts in deconvolution as it affects the selection process. In general, image deconvolution is an iterative process, in which the original image is resampled and pixel intensities are redistributed so that the proposed solution is consistent with the setup of the problem (i.e. based on the estimate of the noise and point spread function). For this reason, it is unnecessary to deconvolve objects that are already faint and have low signal-to-noise ratio (S/N), as the resulting deconvolved image will further suffer from low S/N and offer no new information with regards to galaxy morphologies.

The recovered S/N of the deconvolved image depends on the resolved surface brightness of the

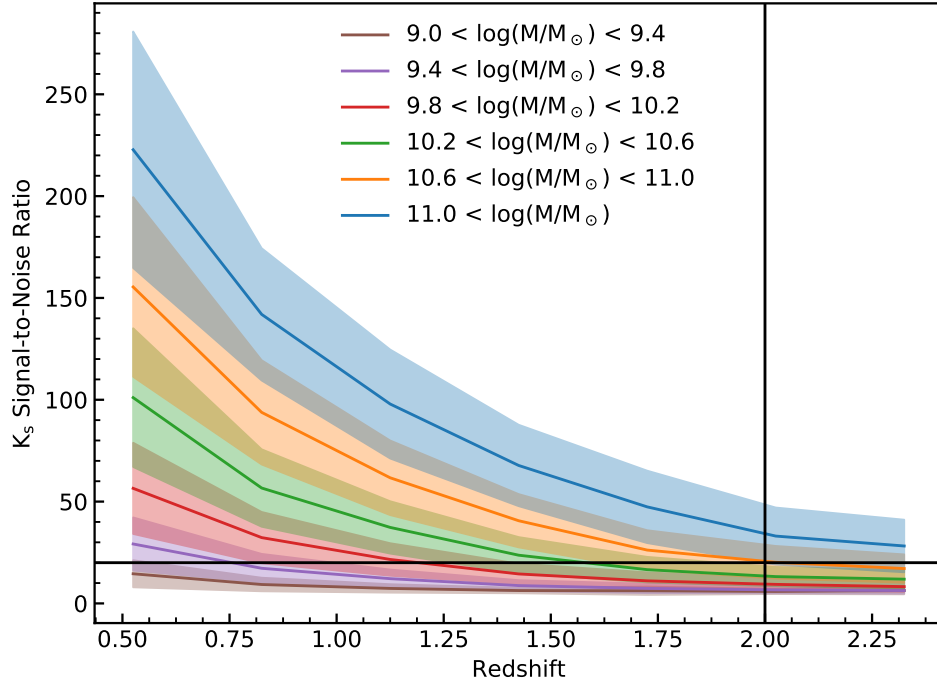


Figure 2.1: Left: The distribution of galaxies in COSMOS based on their K_s S/N and redshift, binned by stellar masses. The black solids show the selection criteria; deconvolution is ineffective at K_s S/N $<$ 20 and above $z >$ 2, only massive galaxies have sufficient S/N.

galaxy. In the ideal situation, we would know the morphology of galaxies *a priori* and can make a cut based on the surface brightness to ensure that the recovered S/N is at some minimum. In practice, the resolved morphology of these galaxies is not known, and therefore, we choose to use the integrated S/N as a proxy for what the resolved surface brightness would be. Figure 2.1 shows the distribution of galaxies based on the integrated K_s -band S/N and photometric redshift for different mass bins. We set the limiting S/N to be 20. Galaxies with integrated S/N in the K_s -band below the limiting S/N are excluded from our sample. Since the majority of galaxies with $\log(M_*/M_\odot) <$ 9.8 are below the limiting S/N, we also omit those galaxies. Similarly, we omit all galaxies above $z >$ 2, since only massive galaxies with $\log(M_*/M_\odot) >$ 11 meet the required S/N at these redshifts.

Note that using the integrated S/N as a proxy assumes that all galaxies at a given magnitude have similar light profiles, which is not necessarily true. This is however unavoidable as the recovered S/N in deconvolved images depends on the morphology of the galaxy. It could be instructive to model what the limiting S/N should be (i.e. assume a minimum S/N for resolved clumps and find its integrated PSF-convolved S/N) in order to create a uniform, mass-complete sample with redshift.

However, our sample is close to mass-complete at $0.5 < z < 1.5$, with only galaxies that have low surface brightness excluded from the low-mass bins at higher redshifts. Regardless of whether we choose to exclude or include these, the observed trends on the fraction of clumpy galaxies will not change.

2.4.2 Star-Forming Galaxies Definition

Using the photometric redshift, stellar mass, and K_s photometry from the COSMOS/UltraVISTA catalog, we construct a sample of galaxies at $0.5 < z < 2$ based on the limiting S/N. We further separate the sample into star-forming and quiescent galaxies as the main focus of the study is on the resolved stellar populations of galaxies during their lifetime prior to quenching. The morphological bi-modality of galaxy populations has been well studied in the local Universe and is observed to persist to higher redshifts. Several methods have already been developed to distinguish the two populations.

In particular, the classification based on the rest-frame ($U - V$) and ($V - J$) colors (hereafter UVJ diagram) has been used in many previous studies (e.g. Williams et al. 2009; Whitaker et al. 2011, Muzzin et al. 2013). The separation of star-forming and quiescent galaxies based on the UVJ diagram has been shown to correlate with the separation based on UV+IR-determined specific star formation rates (hereafter sSFR \equiv SFR/ M_* , e.g. Williams et al. 2009) and based on SED-determined sSFRs (e.g. Williams et al. 2010). The inverse of the sSFR defines a timescale for the formation of the stellar population of a galaxy, which is why it is often used as a diagnostic of quiescence. Therefore, the distinction between star-forming and quiescent is made based on the UVJ, in particular, galaxies are labeled as star-forming if their rest-frame ($U - V$) and ($V - J$) colors satisfy,

$$\begin{aligned} (U - V) &\leq 1.3 \\ (U - V) &\leq 0.88(V - J) + 0.69 \\ (V - J) &\geq 1.6 \end{aligned} \tag{2.1}$$

In the left panel of Figure 2.2, we plot the distribution of galaxies satisfying the limiting S/N and redshift range onto the UVJ diagram. The bi-modality of galaxy populations can be clearly seen in the UVJ diagram, where quiescent galaxies lie along the upper envelope (above the solid black line) and star-forming galaxies along the lower envelope. In total, the number of star-formation galaxies satisfying the color, redshift, and S/N criteria is 22960. In the right panel, we show the distribution of these galaxies in the SFR-M plane, where the SFRs are determined from the UV and IR fluxes (details in Muzzin et al. 2013). It is clear that the UVJ selection is good, as the selected galaxies mostly lie along the star-forming main sequence.

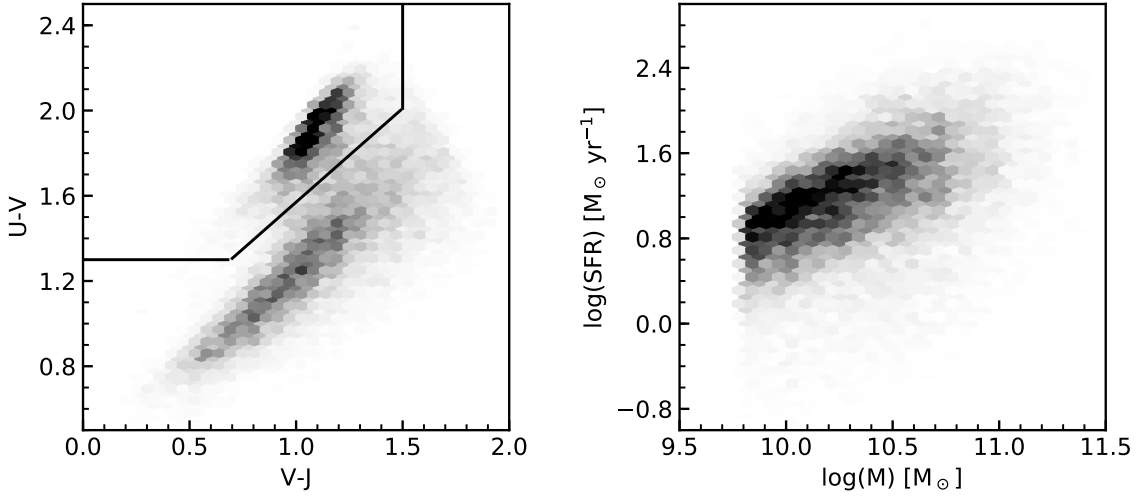


Figure 2.2: Left: The distribution of all the galaxies in COSMOS at $0.5 < z < 2$, based on $(U - V)_{\text{rest}}$ and $(V - J)_{\text{rest}}$ colors, excluding those with $\log(M_*/M_\odot) < 9.8$ and K_s -band S/N < 20 . Right: The distribution of the selected star-forming galaxies in the SFR-M plane.

2.5 Summary of the Data

The COSMOS project aims to study how galaxies are influenced by both their intrinsic physical properties and the environment that surrounds them. This project necessitates a large survey of the field with major telescopes around the world, ranging from X-ray observations to radio observations. In particular, the field was observed in the optical with a number of broad-band and medium-band filters with the Subaru/SuprimeCam instrument, and in the NIR as part of the UltraVISTA survey. These deep and multi-wavelength observations enable in-depth studies of galaxy evolution up to $z \sim 4$. As a result, COSMOS/UltraVISTA is an attractive field to be further processed with image deconvolution, especially when existing HST imaging of the field are available and can be used to validate deconvolution.

To ensure that deconvolved images have the same angular resolution, we use photometric data that are homogeneous in seeing. This resulted in a selection of mosaics that have similar similar with small variations. The photometric data used within this study include the optical broad-band ($B_j, V_j, r+, z+$) and medium-band ($IA484, IA527, IA624, IA738, IB427, IB505$) images with the Subaru/SuprimeCam, and the NIR broad-band (Y, J, H, K_s) images from the UltraVISTA survey.

Our parent catalog is selected from the COSMOS/UltraVISTA catalog from Muzzin et al. (2013). Galaxies are selected to have $\log(M_*/M_\odot) > 9.8$ at $0.5 < z < 2$, with an integrated S/N (in the K_s band) greater than 20. We distinguish between star-forming and quiescent galaxies using the UVJ diagram. The number of SFGs in our final sample is 22960, although the analysis for this dissertation is based on a smaller sample of 9000. While there are some drawbacks to image deconvolution (e.g. results can suffer from low S/N, and are heavily reliant on how well the point spread function is

modeled and the estimates of the noise), deconvolution enables us to perform resolved and multi-wavelength studies of distant galaxies on a larger scale. In fact, the number of galaxies presented in this study is substantially greater than what has been done previously with HST (i.e. ~ 700 galaxies in Wuyts et al. 2012), or could ever be done with HST.

Chapter 3

Image Deconvolution

“Observations always involve theory.”

Edwin Powell Hubble, *The Realm of the Nebulae*

In optical astronomy, the angular resolution (θ) of an image is proportional to the ratio of the observed wavelength (λ), and the diameter of the telescope’s primary mirror (D),

$$\theta \propto \frac{\lambda}{D} \tag{3.1}$$

Instruments with a finite resolving power (or in other words, finite mirror size) will have an instrumental point spread function (PSF). Without any atmospheric effects, an astronomical image of a star is an Airy disk with some apparent size. When observations are made from the ground, an additional contribution to the PSF is introduced due to the turbulent motions of the earth’s atmosphere. Mathematically, the blurring effects can be described as a convolution with a Moffat profile.

Imaging at high angular resolution can be achieved in several different ways. The most straightforward approach is to use space observatories. Space observatories are free of atmospheric disturbances, resulting in observations with unprecedented image qualities. However, they are considerably more expensive to build compared to their ground-based counterparts. The alternative is to correct for the effects of atmospheric disturbances in ground-based observations. Complex optical systems, known as adaptive optics, are designed to detect disturbed wavefronts and adjust their deformable mirrors to correct for these distortions. Further improvements on the post-processed images are also advantageous and possible using numerical techniques. The basis for these numerical techniques is to invert the convolution operation to reconstruct the original image.

3.1 Brief Introduction to Deconvolution

Mathematically, an image (D) taken with a telescope can be modeled as,

$$D = (PSF * M) + Z, \quad (3.2)$$

where PSF is the total PSF, M is the original image, and Z is the noise map. Noise in astronomical images is generally characterized by a Poisson distribution, but can be approximated as the standard deviation of the pixel-to-pixel variations. An image deconvolution algorithm therefore attempts to reconstruct M , given the estimates for noise and the PSF. For future reference, M should be thought of as a solution for the original image.

Image deconvolution is simply a minimization problem, in which M can be obtained by minimizing the cost function,

$$C = \sum_i \left[\frac{D - (PSF * M)}{\sigma} \right]_i^2. \quad (3.3)$$

The summation goes over the pixel number and σ represents the associated noise at that pixel. The term in the cost function is a chi-squared term, which describes how well M fits the data. Therefore, the cost function is designed to provide a solution, M , that produces the minimum value in the cost function. However, the inverse operation of convolution is often degenerate as observed images are sampled and noise properties are not well known. This is further complicated by the fact that the PSF can be challenging to model, as it can vary significantly between observations (even if the same instrument is used).

3.1.1 Finite Resolution Deconvolution

Finite resolution deconvolution (FIREDEC) has two main features which make it more advantageous compared to past deconvolution algorithms; (1) as opposed to completely removing the PSF, images are deconvolved such that the deconvolved image still has a PSF of its own (Magain et al., 1998; Cantale et al., 2016a), and (2) it implements a new noise characterization (based on wavelet filtering and multi-scale analysis), which mitigate the amplification of noise during the iterative process (Cantale et al., 2016a). We briefly describe the algorithm, but we refer readers to Cantale et al. (2016a) for detailed explanations of FIREDEC.

In regards to (1), the PSF of an image can be expressed as,

$$PSF = g * P, \quad (3.4)$$

where g is the target resolution defined by a 2D Gaussian function, and P is the kernel that transforms PSF to g . In this sense, the deconvolution of an image by P will result in a deconvolved image with a resolution of g . Therefore, given a target resolution, FIREDEC can construct a deconvolution kernel, P , so that Equation 3.4 is satisfied.

Given a deconvolution kernel, P , the main cost function for FIREDEC is defined as,

$$C = \sum_i \left[\frac{D - (P * M)}{\sigma} \right]_i^2 + \lambda H \quad (3.5)$$

The first term is the chi-squared term similar to that in Equation 3.3. The second term is known as the regularization term; H is a regularization weighted by a defined Lagrange parameter, λ . The purpose of the regularization term is to suppress high spatial frequencies arising during each iteration of the deconvolution process. While there are different ways to define the regularization term, FIREDEC uses the following definition,

$$\lambda H = \lambda \sum_i \left(\frac{M - \tilde{M}}{\sqrt{1 + M}} \right)_i^2, \quad (3.6)$$

where \tilde{M} represents a solution where the transition between pixel intensities is smooth (in other words, it is the “de-noised” version of M). While there are numerous methods proposed to remove noise from image, the de-noising function used in FIREDEC is based on wavelet decomposition. Therefore, the numerator ($M - \tilde{M}$) defines the noise within M and its minimization depends on the value of λ . When no regularization term is included (i.e. λ is zero), the algorithm will overfit the data, resulting in a noisy solution. On the other hand, if a large λ is used, the solution is smoother as the noise in M is harshly penalized.

3.2 Deconvolution in Practice

Since COSMOS is one of the largest astronomical surveys, it took several observing sessions over an extended period of time to produce mosaic images of the field. These observing sessions had different observing condition, which led to varying image qualities across the mosaics. In Figure 3.1, we show these variations for the different photometric data as Δ FWHM. The FWHM of each star was measured using **SExtractor**. Each mosaic is divided into 15×15 different regions, where each region roughly covers 10 square arcminute of COSMOS. For each region, we calculate the differences between the median FWHM of that region and the median FWHM of the mosaic (Δ FWHM). In general, the variations of the FWHM seeing for the intermediate-band images are scattered, while the broad-band images appear to be more homogeneous.

To account for the variation in PSFs and noise, we divide the COSMOS field into different regions. These regions correspond to the HST/ACS mosaic tiles. Essentially, each tile is an image of a specific region of COSMOS that is approximately 10 square arcminute. We use **SExtractor** to obtain a list of stars for each set of photometric data within those tiles. Generally, the brightest stars, which are flagged as unblended and unsaturated by **SExtractor**, are selected as suitable stars for PSF fitting. We also ensure that the PSF stars do not have any close companions. This is done during the PSF fitting phase where we check the residuals for faint structures that are not associated with the PSF star. Since the FWHM and S/N of the PSF stars can also vary based on the observing

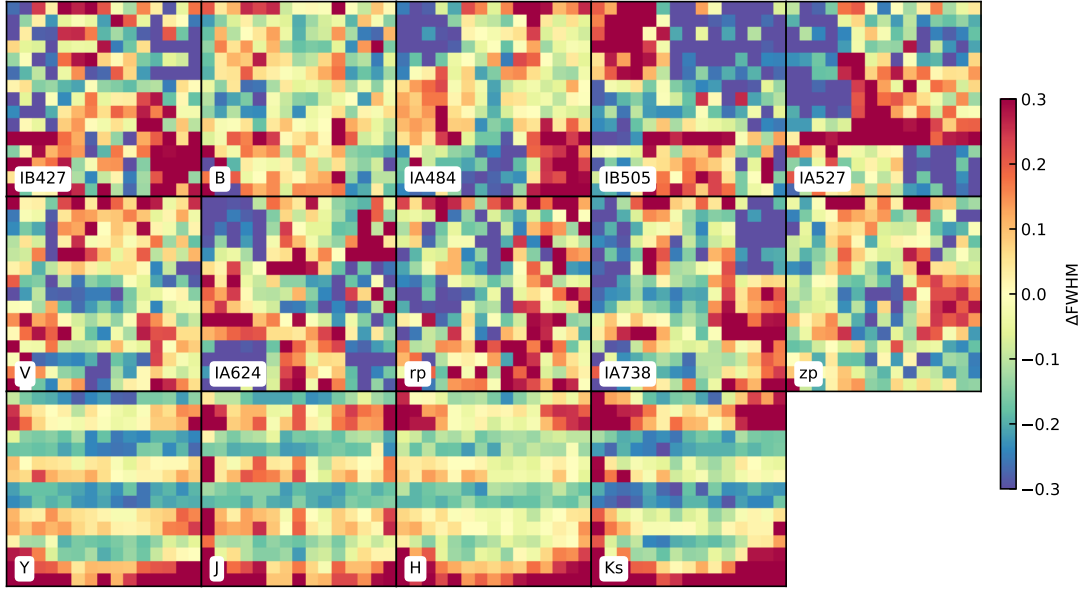


Figure 3.1: The spatial variation in the FWHM seeing in the COSMOS data. We use `SExtractor` to calculate the FWHM of stars within each mosaic. The colormap shows the differences between the median FWHM within each bin and the median FWHM over the mosaic. Each subplot shows the spatial variation in the different photometric data. The FWHM variations within intermediate-band images generally appear to be more scattered, while the broad-band images are more homogeneous.

wavelength, the same star may not be necessarily used as the PSF star for the other photometric data.

Instead of deconvolving the COSMOS mosaic, which requires tremendous computing power, we decide to deconvolve smaller image cutouts centered on each galaxy. At $0.5 < z < 2$, the effective radius of galaxies are observed to be $\sim 3 - 5$ kpc, corresponding to a scale of $\sim 1 - 2''$. We choose to use a cutout size of $7.8''$ by $7.8''$ (52×52 pixels), which is roughly 2-4 effective radii bigger than the estimated size of galaxies. During the deconvolution of each galaxy, we search for the 3 closest suitable stars and simultaneously model the deconvolution kernel. The target resolution is set as $0.1''$, corresponding to a physical size of ~ 0.7 kpc at our redshift range. This target resolution is therefore sufficient to resolve star-forming clumps that have an estimated size of ~ 1 kpc (e.g. Soto et al. 2017). Note that the target resolution is the same for all the photometric data to ensure that each deconvolved image has the same angular resolution. In order to satisfy the Nyquist sampling theorem, which states that the sampling frequency should be at least twice the highest frequency contained in the signal, deconvolved images are sampled so that each pixel corresponds to a physical size of $0.05''$ (i.e. this is the new pixel size). Effectively, this means that our original pixel scale (or the original pixel size per pixel) is increased by a factor of 3.

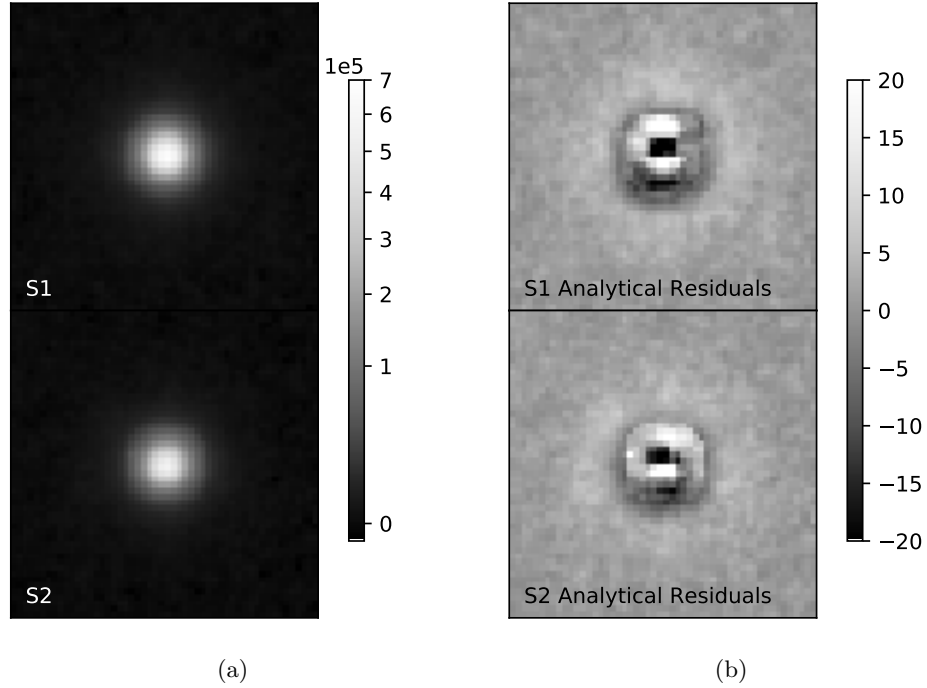


Figure 3.2: The PSF stars (S1 and S2) are shown in the left panels. The right panels show the residuals of the analytical fit. Although, the residuals are relatively small compared to the initial flux of the stars, faint extended structure such as the PSF wings is still visible. This structure will be further fitted by the numerical fit.

3.2.1 Constructing the Deconvolution Kernel

This section gives an overview of how a deconvolution kernel is constructed for the center-most tile (T065) of COSMOS. We select two stars (S1 and S2, Figure 3.2a) that satisfy the conditions of a PSF star. To ensure that differences in the noise and seeing for both stars have minimal effects in the fitting process, the stars are chosen to be nearby stars so that they are representative of the local values.

The deconvolution kernel can be decomposed into two parts; an analytical fit of the PSF and a numerical fit that aims to model any structures that the analytical fit cannot capture. The Moffat profile of a PSF can be analytically approximated as the sum of three elliptical Gaussian functions. This approximation can capture the main characteristics of a PSF (e.g. width, ellipticity, orientation, and the PSF “wings”). Since the idea is to create a kernel that deconvolves images to a target resolution, the analytical fit is obtained by simultaneously fitting the Gaussian approximation, convolved with the target resolution, to the chosen stars.

The analytical residuals (i.e. the difference between the PSF and the analytical fit) are shown in Figure 3.2b. In general, the analytical fit is good, as the integrated fractional residual is $\sim 0.001\%$, and the maximum residual for pixel-to-pixel is $< 0.01\%$. The two analytical residuals are also similar

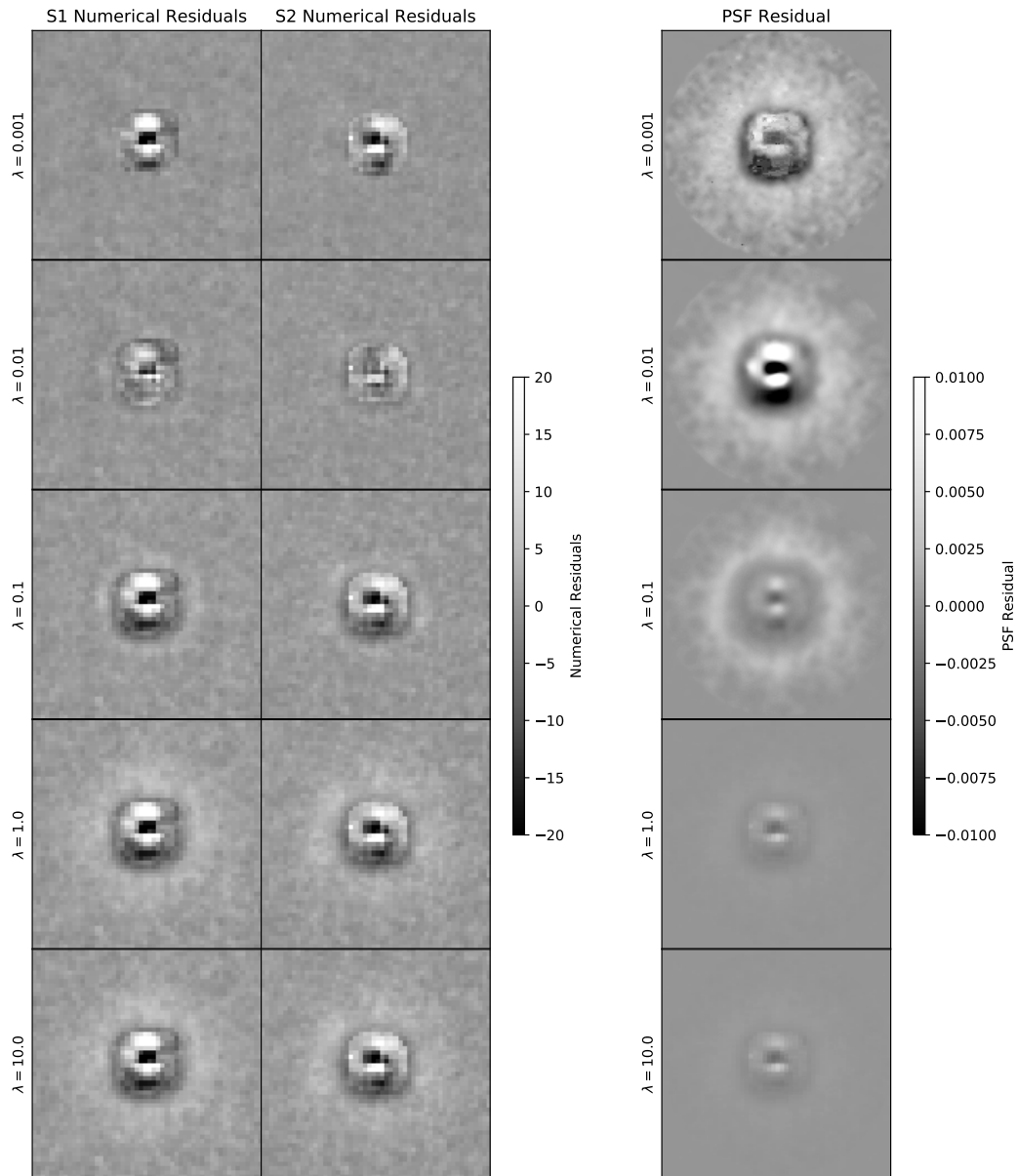


Figure 3.3: The residuals of the superposition of analytical and numerical fit for S1 and S2 are shown in the left panels, while the right panels shows the differences between the analytical and numerical fit. The Lagrange parameter, λ_n , is increasing down the rows. Looking at the right panels, the residuals represent the structures that were fitted in the numerical fit. Note that the residuals are noisier when λ_n is low (e.g. $\lambda_n = 0.001$), indicating that FIREDEC is overfitting the data.

to one another, which indicate that the chosen stars are representative of the local PSF. It is also possible that the PSF stars are different¹, which result in differences in the analytical residuals. In that case, instead of fitting for 3 stars simultaneously, we would reduce the number of stars to be fitted simultaneously, until either the analytical residuals are similar, or until only one star is used. This ensures that the closest star(s) is affected by the same PSF as the galaxy we want to deconvolve.

The numerical fit for the deconvolution kernel is obtained by modeling the structures in the analytical residuals. This is done by deconvolving the analytical residuals by g . Note that this step is required as the angular resolution of the analytical residuals is seeing-limited. In essence, the numerical fit is the solution that minimizes the following cost function,

$$C = \sum_i \left[\frac{\mathbf{afit} - (g * \mathbf{nfit})}{\sigma} \right]_i^2 + \lambda_n H \quad (3.7)$$

This is similar to Equation 3.5, but **afit** and **nfit** now represent the analytical and numerical residuals respectively. Note that the Lagrange parameter is denoted as λ_n to specify that the value for this parameter is different from λ in Equation 3.5.

The value for λ_n can significantly affect the features of the numerical fit as illustrated in Figure 3.3. The residuals of the combined analytical and numerical model (or numerical residuals) for S1 and S2 are shown in the left panels, with λ_n increasing down the rows. The right panels shows the differences between the analytical and numerical fit (or background residuals). In cases where a high value of λ_n is used (> 0.1), the algorithm failed to properly fit the PSF wings, which are still visible in the numerical residuals. However, the faint ring structure disappears when $\lambda_n < 0.1$. It is, however, still unclear what λ_n value should be used, as the ring structure disappears in all the numerical residuals with $\lambda_n < 0.1$. The value for λ_n is chosen by checking the background residuals; noisier residuals indicate that FIREDEC is overfitting the data during the numerical fit. A “good” λ_n value should have minimal structures in the numerical residuals and a relatively smoothed background residual. For this example, $\lambda_n = 0.01$ is a good value to use in order to fit the deconvolution kernel.

It should be noted that the Lagrange parameters (λ and λ_n) used for this dissertation are not optimized, but are close to the optimal values. As we will show in the next section, the deconvolved images already resemble HST images even though we did not optimize these parameters. In principle, there should be one value for λ_n which gives the best approximation of the PSF. (Likewise, there should be one value for λ which gives the best solution for deconvolution.) We stress that the main advantage of using image deconvolution on ground-based data is the larger sample of tens of thousands of galaxies. Since FIREDEC currently does not automatically search for the best values, manually searching the parameter space at this scale is completely unfeasible and impractical. Further, as long as the Lagrange parameter is close to the optimal value, getting the precise value does not have a strong effect on the final deconvolution.

¹In the few cases where galaxies lie along a region with varying image qualities

3.3 Validation of Deconvolution using Space-Based Data

To further investigate the effectiveness of FIREDEC, we empirically validate the deconvolved images by comparing them to the available HST images in this section. While COSMOS is the widest HST survey ever taken, observations of the entire field were primarily done with the F814W band. These deep observations allow astronomers to detect faint structures in distant galaxies. Other observations of COSMOS (e.g. COSMOS in g -band, COSMOS-DASH, CANDELS/COSMOS, see Section 2.1.1) are shallower and restricted to a smaller region of COSMOS. As a result, this section is broken into two parts, with the first part focusing on the quantitative comparison with the I_{814} image and the second part on the qualitative analyses of multi-wavelength deconvolution with the $F475W$, $F606W$ and $F160W$ images.

3.3.1 Comparison with the F814W Data

In order to compare the deconvolved and HST images, we first account for differences in the astrometric alignment and angular resolution. This is necessary to ensure that the residuals show the intrinsic differences, and not systematic differences. We align the astrometry by cross-correlating the I_{814} images with the deconvolved images. The angular resolution between the two images is also different due to the necessary regularization inherent in deconvolution. The regularization term causes flux to spread, which can cause deconvolved images to have a slightly degraded angular resolution compared to HST images. Therefore, we PSF-match our HST images to the deconvolved images, where the kernel is taken as a Gaussian function. The FWHM of the kernel is varied as we iteratively convolve it with the HST images until their residuals between the PSF-matched HST and deconvolved images are minimized.

Figure 3.4 shows a few examples deconvolution of the $z+$ images. The galaxies are randomly chosen over a range of redshifts, and vary in term of S/N, angular size and visible substructures. The first three columns show the ground-based images, the deconvolved images and their corresponding I_{814} images respectively. The last two columns show the residuals between the deconvolved and HST images and the same residuals normalized by the PSF-matched HST images. In general, the light profile of galaxies observed in the ground-based $z+$ filter are smooth, representative of underlying older stellar populations. We see dramatic improvements when comparing ground-based to deconvolved images. Complex substructures are unveiled by FIREDEC within the deconvolved images for a few cases, and these are further confirmed by the ACS images. In particular, clumpy structures are resolved in the deconvolved images for both ID115280 and ID121068. The light profile of these features is also well constrained by FIREDEC, with residuals consistent of the background noise.

At first glance of the residual maps, the deconvolution of bright luminosity profiles such as bulges appear to be less well constrained by FIREDEC. However, the normalized residual maps

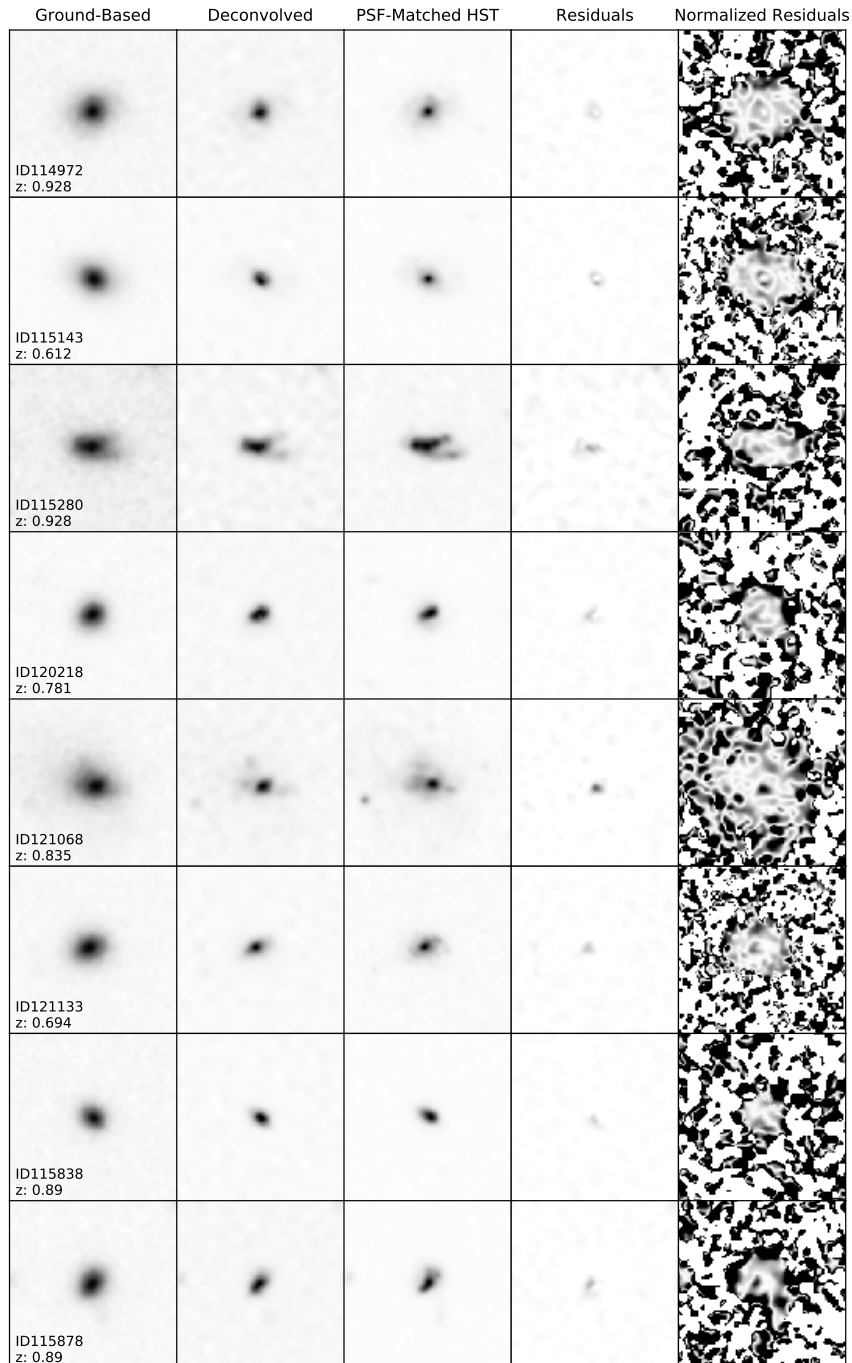


Figure 3.4: Left to right column are ground-based $z+$ images, their corresponding deconvolved images, their corresponding F814W images, the residuals, and the normalized residuals. The residual maps show the difference between the deconvolved images and the PSF-matched HST images, calculated at the same pixel scale as the deconvolved images ($0.05''$). Similarly, the normalized residuals show the absolute residuals, normalized by the PSF-matched HST images.

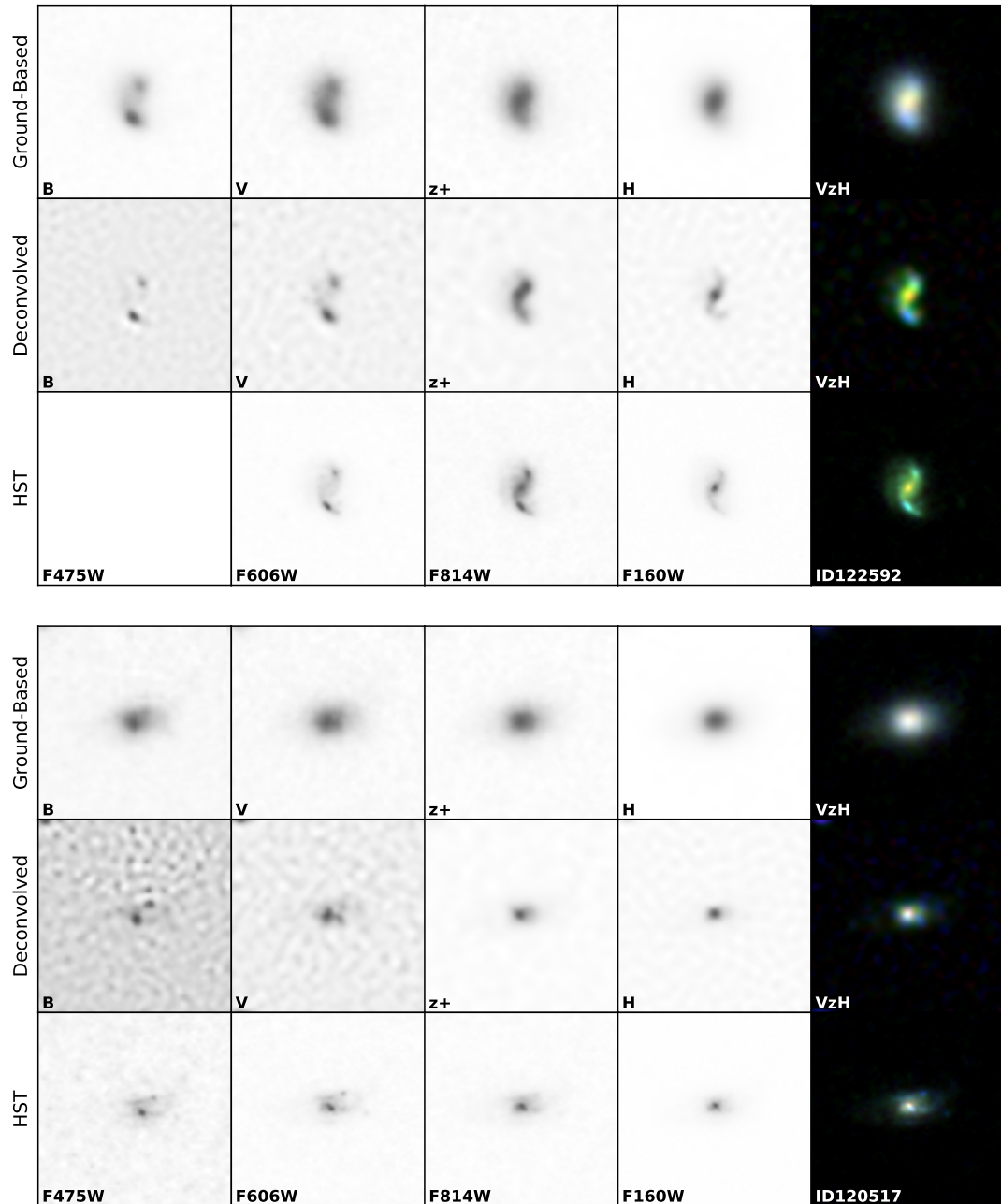
show that the residuals are actually consistent for each image. We also note that, in principle, a deconvolved image shows the true light distribution convolved by a Gaussian PSF with a FWHM of 0.1". A Gaussian PSF is not the same as the diffraction limit PSF of HST, which has ring-like and “spikey” structures. The inclusion of these structures in a kernel can alter the light profile in different ways, and can cause minor differences between the deconvolved and HST images. Combined with the necessary regularization, this can prevent the deconvolved data from reaching the true light distribution in the inner parts of very sharp profiles. While this suggests that the flux of individual pixels may not be perfectly calibrated (particularly for structures smaller than the target resolution such as bulges and clumps), we stress that pixels are binned together when we fit for the stellar populations. This ensures that the correct physical properties within each bin are extracted from the SED models. The binning process is explained in Section 4.3.

3.3.2 Multi-Wavelength Comparison

In the previous section, we show that the reconstructed light distributions are consistent with their space-based counterparts, with negligible structures in each residual map. However, the $z+$ filter probes the rest-frame V for galaxies at $z < 1$. An important question to address is whether image deconvolution can be used to detect kiloparsec-scale, star-forming regions for low- z galaxies, and whether color variations are preserved after deconvolution.

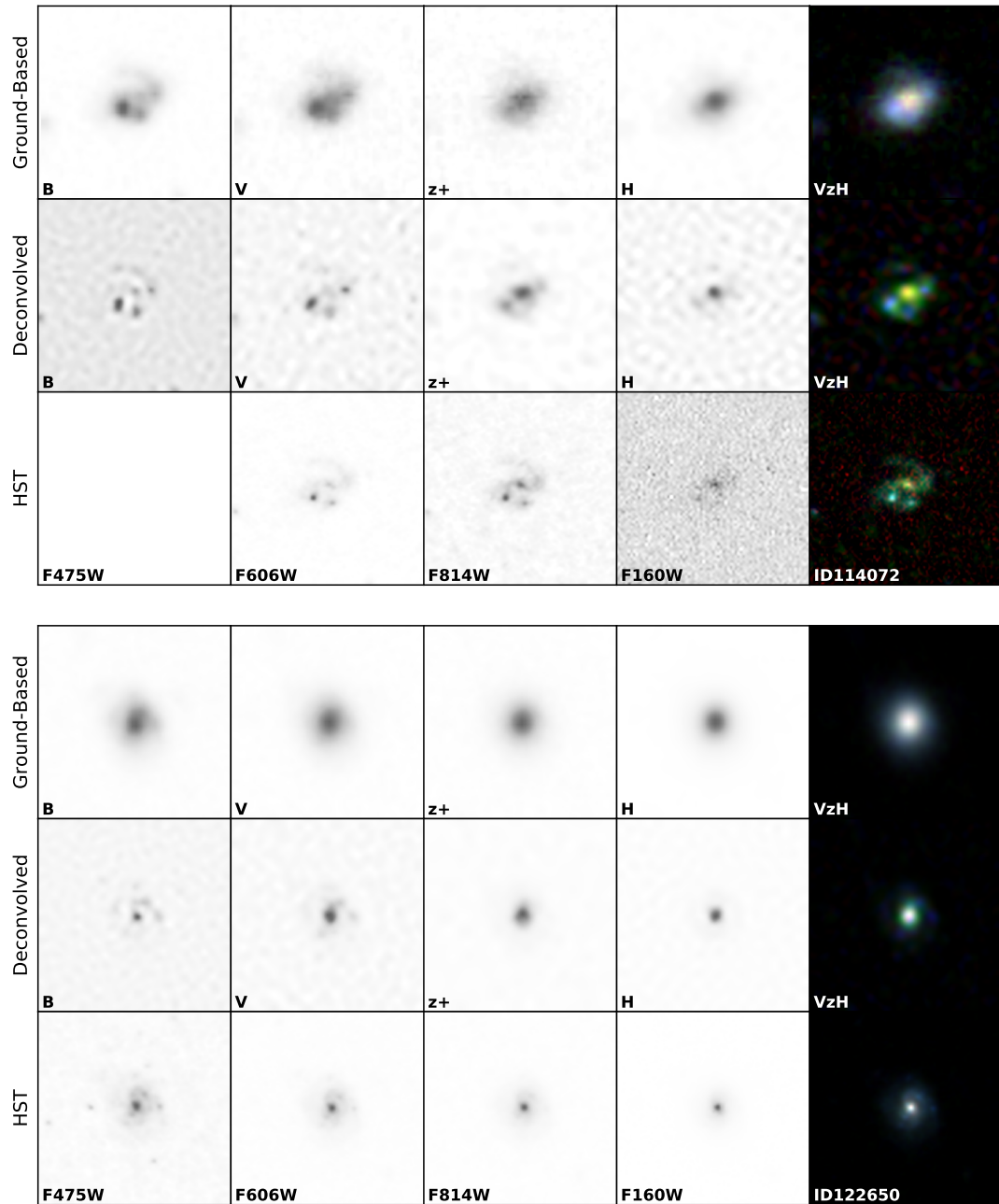
Figure 3.5 show examples of the multi-wavelength deconvolution. It should be note that we do not use information between the different filters as an addition constraint for deconvolution, but instead, each image are separately deconvolved. The galaxies shown are taken from the center-most region of COSMOS, where there exists overlapping HST imaging, and are showcased mainly for their clumpy morphologies. The grey-scale images along each row correspond to the different filters, going toward redder filters from left to right. From top to bottom, each row corresponds to the ground-based, deconvolved and HST images respectively. Note that the HST images are not degraded to match the seeing of the deconvolved data. In the left panels, we show the RGB composite image (or postage stamp) of each galaxy.

A quick visual inspection of the deconvolved and HST data shows striking similarities. While we can descry certain star-forming regions from the ground-based color images alone, these structures are typically smeared out and blended with its host galaxy’s bulge. However, deconvolution clearly resolves these structures. In particular, the grey-scale images for the B (or V) filter and the color images are remarkably comparable to the HST images, with an angular resolution that is on par with HST’s resolution. The robustness of FIREDEC is further highlighted in ID122650, where deconvolution unveils distinct clumps that cannot be detected within the original ground-based images (see B and V images). These structures are also confirmed by HST.



(a)

Figure 3.5: Examples of multi-wavelength deconvolution. For each figure, the rows correspond to the ground-based, deconvolved, and HST images, while the columns show an image of each galaxy in a different filter. The right panels show the composite color images, where the ground-based images are based on the V , $z+$ and H filters and the HST image is based on the $F475W$, $F814W$ and $F160W$ filters.



(b)

Figure 3.5: Same as above.

3.4 Summary of Image Deconvolution

Image deconvolution is a minimization problem, where pixel intensities are redistributed at each iteration until an optimal solution is found. Finite resolution deconvolution implements two new features to help constrain solutions; (1) FIREDEC deconvolves to a finite resolution, and (2) it has a new way of characterizing and regularizing noise during the iterative process. To model the deconvolution kernel, we search for bright stars that are not saturated and have no companions. During the analytical and numerical fit of the deconvolution kernel, the residual maps are checked to ensure that the PSF stars are representative of the local PSF. The target resolution of each deconvolution is set to $0.1''$, which corresponds to a physical size of ~ 0.7 kpc at $0.5 < z < 2$. This target resolution therefore enables us to detect clumps, which have an estimated size of ~ 0.9 kpc based on HST studies.

We also show the robustness of finite resolution deconvolution. In particular, we show that there is a substantial improvement going from ground-based images to deconvolved images, where small-scale structures such as star-forming clumps are unveiled by deconvolution. Further, we validate these structures with the available multi-wavelength HST observations, and show that deconvolved images generally resemble HST images. However, note that deconvolved images are not flawless and that there are differences between deconvolved and HST images. The deconvolved light profile of bright, small-scale structures may not be perfectly calibrated due to the fact that we are deconvolving to a finite resolution and regularization causes flux to spread. Further, since the trade-off for an increased spatial resolution is higher frequency components, deconvolved images generally suffer from low S/N, and in some cases, deconvolution artifacts are created. While these issues suggest that there may be structures that are not perfectly resolved, or even artificially created, we stress that the properties of these structures can be constrained by using the photometric information across multiple filters. Further, during the SED modeling process, pixels are binned together (see Section 4.3) to ensure that there is some minimum signal. For these reasons, we are confident in our ability to broadly classify galaxies as clumpy or non-clumpy using the deconvolved data.

Chapter 4

Methodology

In the previous chapter, we have shown the process in which a deconvolution kernel is created and a few examples of deconvolution. This chapter provides an overview of the analytical tools needed to produce stellar populations maps from the deconvolved images. We also describe the methodology of identifying clumpy structures within the stellar population maps in order to infer their physical properties.

4.1 Segmentation Maps

For computational purposes, image deconvolution is done on a small cutout centered on a galaxy. While each cutout is centered on the galaxy, it is unavoidable that other objects are visible within these cutouts. To distinguish different objects within the cutouts and to assign specific pixels to each object, we create a segmentation map for them.

Typically, `SExtractor` is used to simultaneously create a segmentation map and a catalog of the mosaic. However, we omit rerunning `SExtractor` on the K_s -band image and avoid unnecessary complications with matching the new catalog to the existing one as we already have the coordinates of our galaxies from the COSMOS/UltraVISTA catalog. Instead, we utilize a Python implementation of the watershed algorithm to associate specific pixels to an object. The philosophy behind the watershed algorithm is that the intensity of a grayscale image can be viewed as an overturned topological surface, where local peaks of an image denote the deep points of the topological surface. Image segmentation with the watershed algorithm can be thought of as the process of filling the valley with water; as the water level start to rise, water from different sources will start to mix. To avoid this, the algorithm build barriers at the locations where water merges. The barriers define the boundary of each segmentation map.

To apply the watershed algorithm on a image in practice, we define the background and the local peaks of a given ground-based (undeconvolved) image of the galaxy. The image is rescaled so

that the new pixel scale is the same as the deconvolved pixel scale. The background of the image is determined by performing $3\text{-}\sigma$ clipping on the image. We mask the background, and the masked image is then normalized by the negative of its sum. The local peaks (i.e. sources at which the watershed algorithm will start to “add water”) are taken as the coordinate of the galaxies that are found within the cutout.

4.2 Misaligned Astrometry

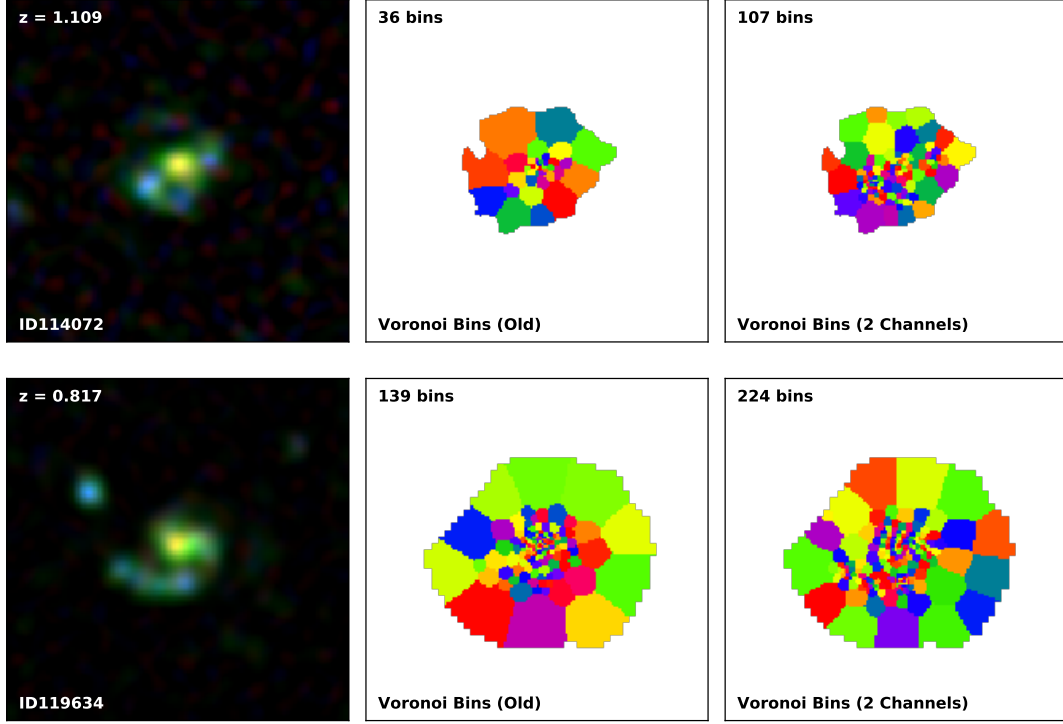
Large surveys require multiple telescope pointing which cause small offsets in the astrometric solution (e.g. $< 0.2''$ for the optical data and $0.1''$ for the NIR data, Capak et al. 2007; McCracken et al. 2012). These offsets are roughly the size of clumps, and therefore can have significant impact on our clump identification. This is particularly true in the case of compact galaxies, since any potential misalignment of those galaxies at bluer wavelengths could be mistaken as an off-center star-forming clump.

While the morphology of galaxies can differ considerably when comparing the optical and NIR images, their morphology is comparable between adjacent filters. As a first-order correction for any potential offsets, we calculate the relative offsets in pixel position by iteratively cross-correlating each photometric cutout to its adjacent longpass photometric cutout. To this end, we fix the K_s photometric cutout, and align the other cutouts to it. The correction is made based on the original ground-based images; we use the integrated S/N of the galaxy (taken from the UltraVISTA catalog) as an indicator of whether a correction should be made. If the S/N for a given cutout is less than 5, we do not apply any corrections to that specific cutout as there is already very little signal within the image.

4.3 Pixel Binning

Since individual pixels can have little to no significant signal (especially when the images are post-processed with deconvolution), biases can be introduced when fitting stellar population models to the spectral energy distribution. A solution is to group pixels together in different bins, so that each bin has a minimum S/N. This ensures that the correct stellar properties for each bin can be inferred. An example of the binning technique can be seen in Wuyts et al. (2012), where they used the Voronoi binning technique by Cappellari & Copin 2003 to bin pixels based on the H band. However, since the morphology of galaxies can vary considerably from the UV to NIR, binning based on the NIR alone can cause compact and localized signals to smear across larger regions.

In this study, in order to deal with the spatial changes of the SEDs, we modified Cappellari & Copin (2003)’s 2D Voronoi binning technique so that there are two binning channels; one based on the band that probes the rest-frame U of the galaxy (i.e depends on the redshift) and the other



(a)

Figure 4.1: Examples of the original Voronoi bins vs. our 2-channels Voronoi bins. For left to right, we show the composite image using the deconvolved data, the original Voronoi bin, and the new Voronoi bins. The original Voronoi binning technique is modified so that there are 2 binning channels (based on the band that probes the rest-frame U of the galaxy and the K_s band), the accretion of pixels toward a bin stopping once either one of those binning channels reach a minimum S/N of 5. In general, the 2-channels Voronoi binning technique result in more bins, particularly around bright, blue clumps.

based on the K_s band. In the original Voronoi binning technique, a pixel is accreted to a bin if the addition of that pixel improve the S/N of the bin. The accretion of pixels stop once the bin reaches the minimum S/N. In the modified version, the binning process is similar, except a bin is decided if it reaches a minimum S/N in either one of the bands. At that point, the algorithm will start a new bin. We define the minimum S/N to be 5. As an additional step to the binning process, we choose to optimally weight the pixels using Equation (3) in Cappellari & Copin (2003) as some pixels have virtually no signal.

As an example, we show the two different binning methods in Figure 4.1. The left panels show the composite image of the SFGs, while the middle and right panels show the original Voronoi bins (based on the K_s band) and the new Voronoi bins (based on the two different bands) respectively. In particular, in regions where prominent clumps are visible in the composite images (blue in color), the original Voronoi bins are generally larger compared to the new Voronoi binning based on 2 channels.

This is further demonstrated by the fact that the new binning technique results in more bins.

4.4 Resolved Spectral Energy Distribution Modeling

We use EAZY (Brammer et al., 2008) to compute the rest-frame U and V luminosities for each spatial bin for all galaxies. EAZY calculates the colors by integrating the best-fit SED through the redshifted filter curves over the appropriate wavelength range. We use the response curve defined in Maíz Apellániz (2006) for the U and V filters. We fix the redshift of each bin to the photometric redshift (or the spectroscopic redshift when available) of its respective galaxy.

The resolved stellar population parameters of each bin are determined by individually fitting Bruzual & Charlot (2003)’s stellar population synthesis models to the 15-bands u^* -to- K_s SED. The fit is done with the code: Fitting and Assessment of Synthetic Template (FAST, Kriek et al. 2009). We adopt a Chabrier (2003) initial mass function and Calzetti et al. (2000) dust extinction law, and assume a uniform solar metallicity and exponentially declining star formation history. We allow $\log(\tau)$ to vary between 7.0 and 10.0, in increments of 0.2, and $\log(t)$ to vary between 7.0 and 10.0, in increments of 0.1. We also restrict t to be less than the age of the universe at the observed redshift of each galaxy. The visual attenuation (A_v) of each fit is allowed to vary between 0 and 4.

It is always a concern whether certain parameters can affect clump properties. However, these effects are usually systematic. Indeed, both mass of the galaxy and its clumps will change in a similar way if we vary the metallicity parameter. If the metallicity of clumps differs from its host galaxy, then we would be inferring the wrong clumps’ mass relative to the galaxy’s. Given that we are working with low S/N photometry, we do not have a handle of the metallicity without performing resolved spectroscopy of these galaxies.

4.5 Clumpy Structures Analyses

A wealth of information can be inferred from the SED models, allowing us to construct resolved maps of stellar population properties (e.g. stellar mass, star formation rate, dust attenuation, age) and surface brightness (e.g. rest-frame U and V luminosities). In this section, we address the spatial variations in stellar populations and colors to identify clumpy structures. This is done by creating normalized profiles for the complete sample of galaxies. A normalized profile is a two-dimensional profile that quantifies the dependence of stellar population properties simultaneously on both surface brightness and galactocentric radius, enabling us to detect spatial variations in stellar population maps. We briefly discuss the process in creating the 2-dimensional profiles, and the classification scheme to identify clumpy regions below, but we refer the reader to Wuyts et al. (2012) for a more detailed discussion of the process.

4.5.1 Normalized Color and Stellar Mass Profiles

We adopt a stellar mass-weighted center to be a reference for all measurements,

$$\begin{aligned} x_c &= \frac{\sum_i x_i M_i}{\sum_i M_i} \\ y_c &= \frac{\sum_i y_i M_i}{\sum_i M_i} \end{aligned} \tag{4.1}$$

The normalized brightness profiles are constructed as follows. We first associate the morphology of each galaxy with a position angle and axial ratio, which is done by fitting an ellipse to its segmentation map. The ellipse parameters are derived from the segmentation map, rather than surface brightness, so that the aperture shape is not driven by individual clumps superimposed on an otherwise smooth surface brightness distribution. We define a half-light radius (R_e) as the semi-major axis length at which an elliptical aperture contains 50% of the light. This radius is derived by constructing a curve of growth from elliptical apertures centered on the mass-weighted center. Having established a half-light radius, we measure the average surface brightness within the half-light radius (Σ_e). The surface brightness of each spatial bin in a galaxy is then normalized by the average surface brightness, and the galactocentric distance (of each pixel in the spatial bin) is normalized by the half-light radius.

The same procedures are used to create the normalized stellar mass profiles, except we compute the half-mass radius as the semi-major axis length at which the curve of growth reaches 50% of its maximum value in the surface stellar mass density map. Note that for a given galaxy, each pixel will have a different normalized distance to the center depending on whether the measurement is made on the U_{rest} , V_{rest} or stellar mass map. This is because the half-mass radius is not necessarily the same as the half-light radius. Since the galactocentric distance of a given light profile is normalized by the half-light radius measured in that band (as opposed to always normalizing by the half-mass radius), galaxies with identical surface brightness distributions will be mapped onto identical positions in the normalized (Σ/Σ_e , R/R_e) space, regardless of the underlying stellar mass distribution. This approach allows for a consistent classification of spatial bins into inner, outer and clumpy regions based on the wavelength of interest.

4.5.2 Examples of Normalized Profiles

Figure 4.2 shows examples of the normalized profiles alongside the resolved U_{rest} , V_{rest} and stellar mass maps for several galaxies. The composite image of the galaxy is shown in the top left panel, while the rest-frame ($U-V$) color map is shown in the top right panel. The radial profile of each map is shown in the right column, where the color map corresponds to the rest-frame ($U-V$) colors.

A number of trends are revealed by the normalized profiles. All three radial profiles are relatively flat within the half-light (half-mass) radius for all the examples. Since galaxies are typically described as Sersic profiles, we expect to find decreasing profiles even within the half-light radius.

The flattening of the radial profiles suggests that our profiles are limited by angular resolution. Indeed, Wuyts et al. (2012) observed a similar flattening in their radial profiles. We note that this does not affect our analysis as we expect to find clumps at the outskirts of galaxies, where the surface brightness is lower. Even at higher resolution, it might be difficult to identify centrally-located clumps as the central brightness of galaxies are much higher.

The surface brightness drops at larger radii, with a considerable scatter. The range in Σ/Σ_e can vary between 0.5-3.0 dex at $R \simeq R_e$. For specific cases (e.g. Figures 4.2a, 4.2b, 4.2c, 4.2d), the large scatter is driven by localized and enhanced brightness within the luminosities, which can exceed the central brightness by ~ 0.2 dex. For the remainder of the paper, we refer to any off-center regions with an enhanced level of surface brightness as “clumps”. This nomenclature is inspired by the morphological appearance of the galaxies as shown in Figure 4.2. However, we stress that this definition encompasses all regions that have an elevated surface brightness, regardless of their geometric shapes (e.g. structures such as spiral arms). It is not intuitive whether a distinction can be made between real clumps and these structures based on the excess of surface brightness alone.

In general, clumps appears as blue regions superimposed on an underlying older stellar population. There is also a color gradient with respect to the normalized radius; we typically find redder colors within the inner region of the objects ($R < -0.5R_e$). While the color gradients can vary for individual cases, the trends we have identified for our examples are consistent and representative of population mean at $0.5 < z < 2.5$ (see Wuyts et al. 2012). Finally, although some galaxies exhibit clumpy morphologies in both appearance and color profiles, the mass profiles for these galaxies appear to be rather smooth.

4.5.3 Classification Scheme for Clumpy Structures

There are several methods of identifying clumpy structures; either based on visual inspection, or algorithms. Identifying clumps based on an algorithm relies on finding pixels that have an intensity above some smooth threshold, which the normalized profiles naturally allow us to do. Following the classification scheme of Wuyts et al. (2012), we split the normalized parameter space into inner, outer and clump sections (see dashed line in the right column of Figure 4.2);

$$\begin{aligned}
 \text{[inner]} \quad & x < -0.5 \\
 \text{[outer]} \quad & x > -0.5, \quad y < 0.06 - 1.16x - x^2 \\
 \text{[clump]} \quad & x > -0.5, \quad y > 0.06 - 1.16x - x^2
 \end{aligned} \tag{4.2}$$

where $x \equiv \log(R/R_e)$ and $y \equiv \log(\Sigma/\Sigma_e)$. Pixels are labeled as inner, outer, or clump based on their location in the $(\Sigma/\Sigma_e, R/R_e)$ space.

However, it is still subjective what the distinction between a clumpy and non-clumpy galaxy is; are all galaxies with clumpy pixels “clumpy”? Recent studies compared the luminosity of clumps to

their host galaxy (i.e. the fractional luminosity) to make the distinction between clumpy and non-clumpy. In Wuyts et al. (2012), clumpy galaxies are defined to be galaxies with clumpy pixels that contribute more than 5% of the total luminosity. On the other hand, Guo et al. (2015) and Shibuya et al. (2016) defined a galaxy as clumpy if it has off-center clumps with a fractional luminosity of 8%. This fractional luminosity was derived by comparing the fractional luminosity of star-forming regions in high- z galaxies and the fractional luminosity of local star-forming regions found in a low- z galaxy. Note that the low- z galaxy was artificially redshifted in order to account for observational effects. The fractional luminosity of 8% represents the point where high- z star-forming regions differ from the redshifted local star-forming regions (in terms of the number count of clumps with that fraction luminosity, see Guo et al. 2015 for further details). Similarly in our case, with the aspiration to focus specifically on galaxies that are really “clumpy”, we choose to use the same fractional luminosity of 8% as the dividing line between clumpy and regular galaxies.

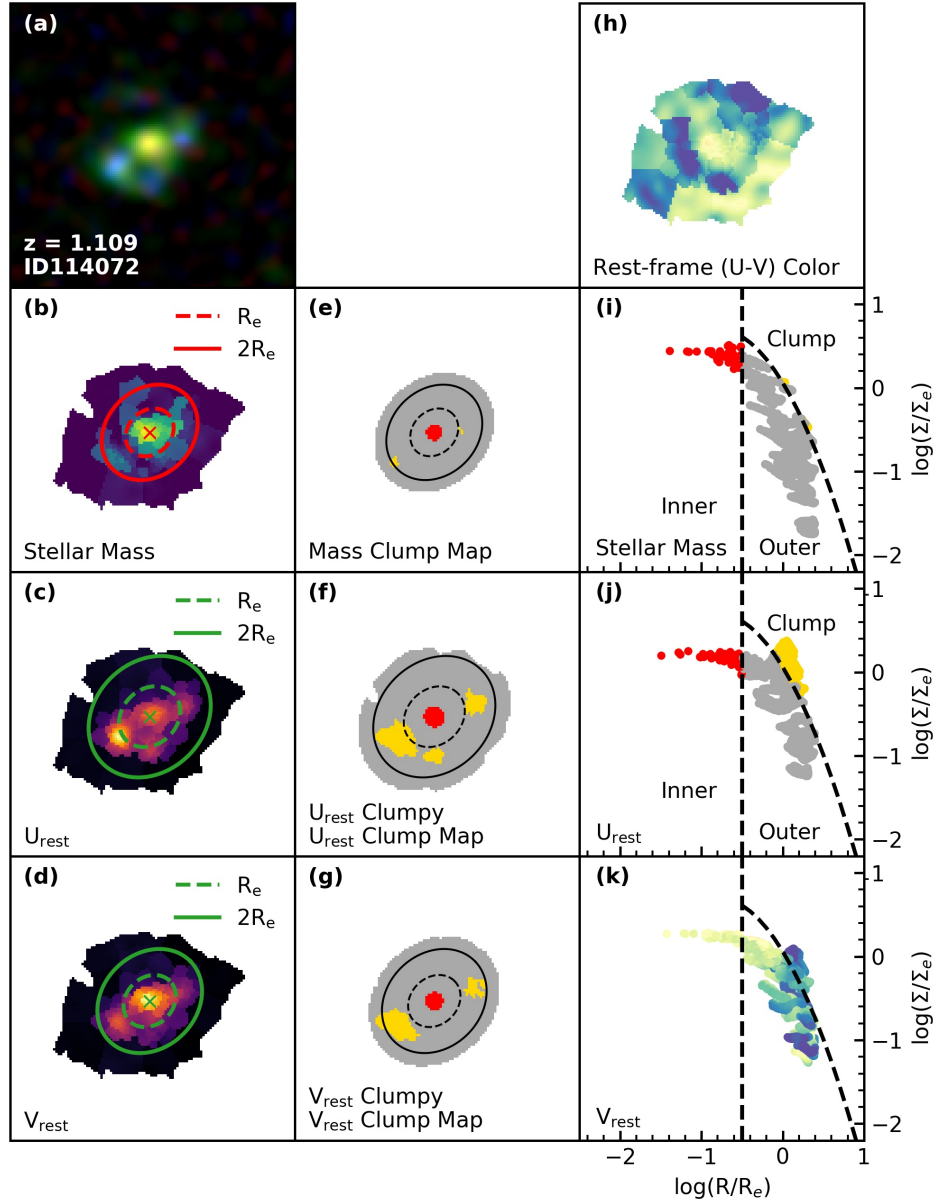
In essence, we use the resolved maps for the two rest-frame luminosities (U and V), as well the stellar mass maps to identify clumpy pixels. A galaxy is defined as clumpy in a given band if pixels originating from the clump regime contribute to at least 8% of the galaxy’s total luminosity in the respective band. Similarly, galaxies are identified as clumpy in stellar mass if at least 8% of the total stellar mass of the galaxy originated from pixels in the clumpy regime of the normalized mass profile. Note that Wuyts et al. (2012) made the dividing lines (Equation 4.2) based on a visual inspection of their normalized profiles, and these lines are fixed for different galaxies. It is visible that these cuts are sufficient to separate the different regions. This is illustrated in the middle column of Figure 4.2, where pixels are color-coded based on their pixel type (i.e. inner, outer, or clump). In general, pixels that are identified as clumpy (color-coded as yellow) correspond to pixels that have a strong blue component in the composite image. The normalized profiles show that these pixels also have blue rest-frame ($U - V$) color.

We iterate that the nomenclature for “clump” in this study includes any off-center regions that have an excess of surface brightness (or stellar mass density) regardless of its geometric shape (e.g. this includes spiral arms and ring-like features). For the rest of the paper, we refer to non-clumpy galaxies as regular galaxies.

4.6 Summary of Methodology

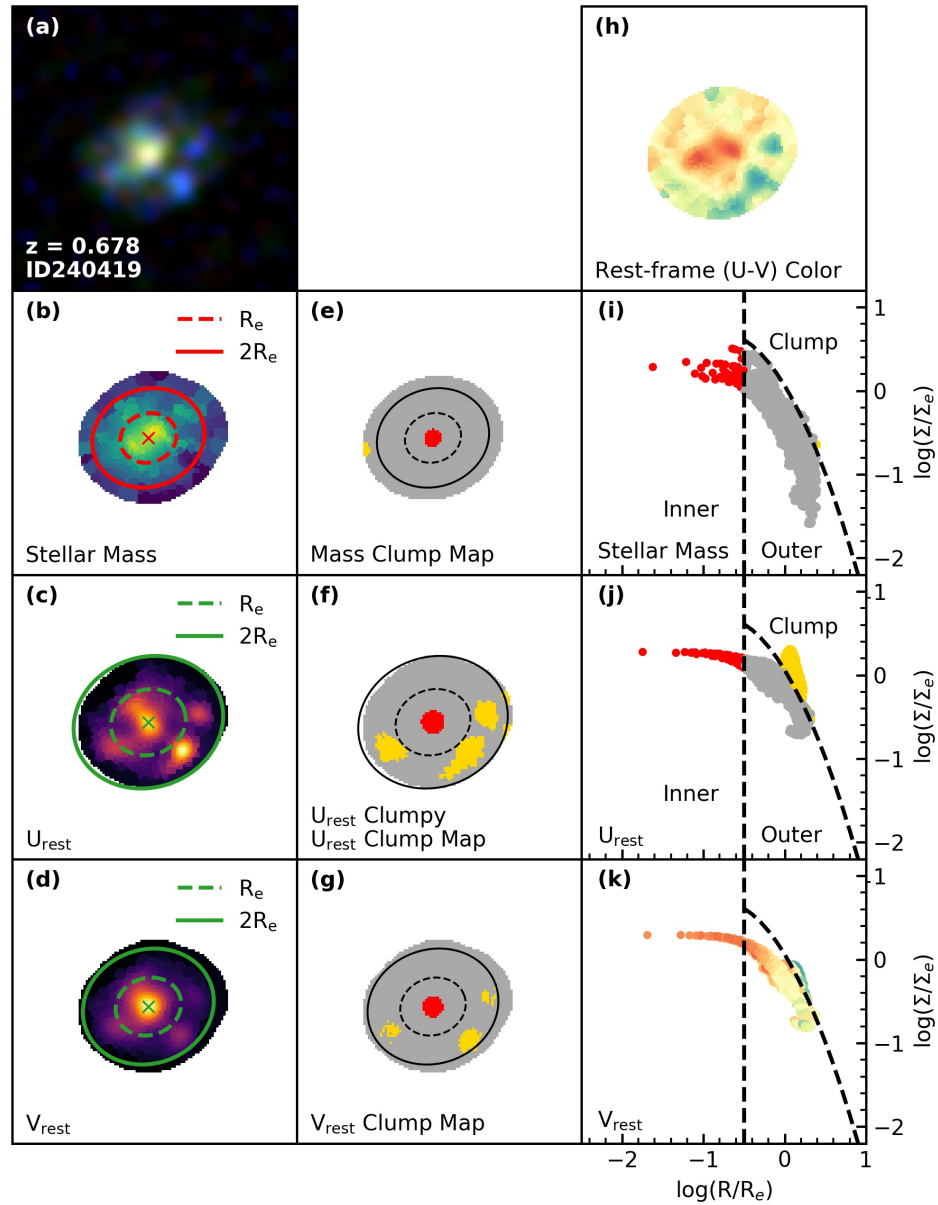
To assign specific pixels to objects in our cutouts, we employ a watershed algorithm in `Python` to create a segmentation map of each object. We also re-align the astrometry of each photometric image to the K_s band by iteratively cross-correlating each photometric cutout to the adjacent longpass cutout. This re-alignment is necessary to ensure that the inferred physical properties are intrinsic and that clumpy structures are not misidentified as the result of offsetted photometric data.

Since noise is enhanced in deconvolved images and the light profile of bright structures may



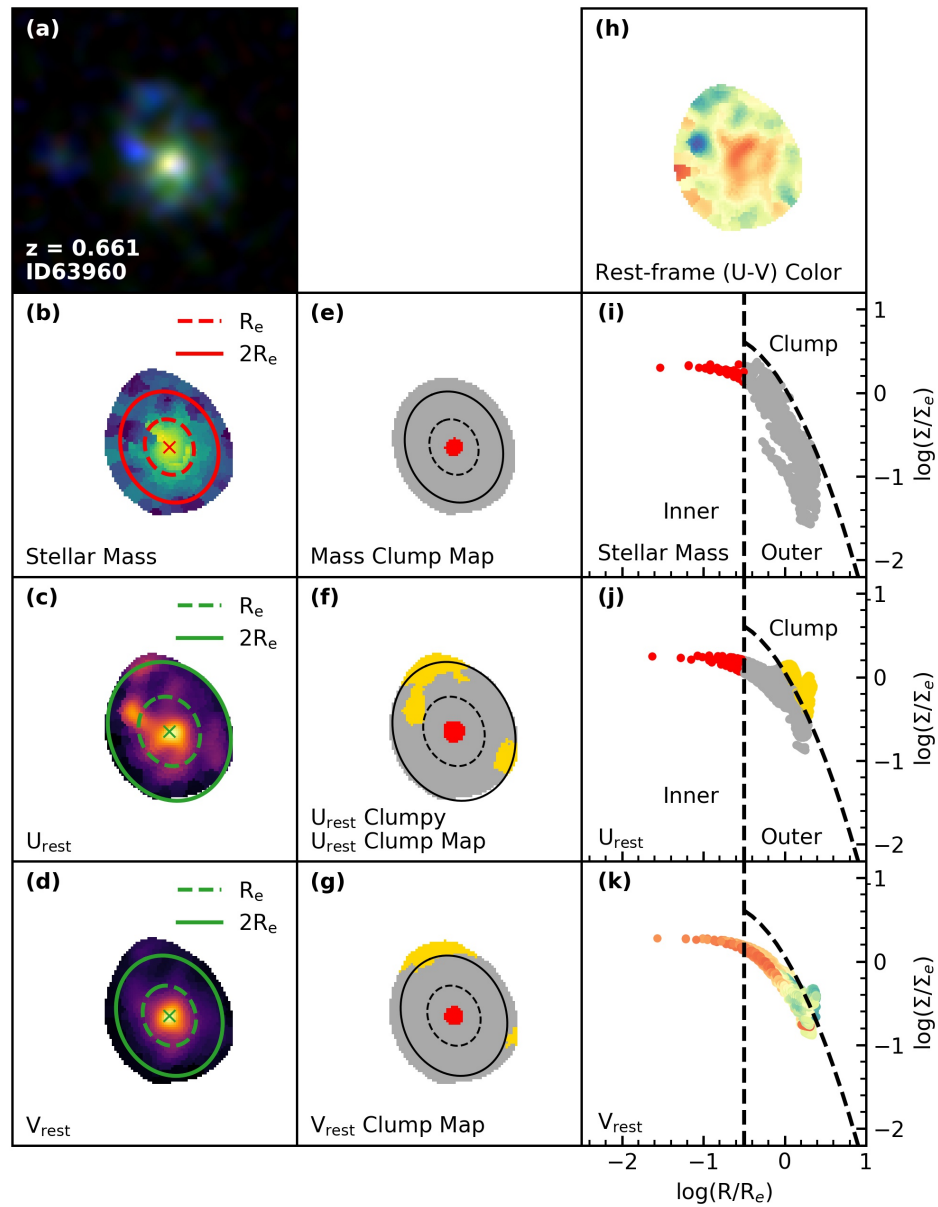
(a)

Figure 4.2: Examples of the 2D maps and their normalized profiles for star-forming galaxies with and without clumpy features. Panels (a), (b), (c) and (d) respectively show the composite image, the stellar mass, the U_{rest} , and V_{rest} maps. Panels (e), (f) and (g) indicate whether pixels of a given map fall into the inner, outer, or clump regime as defined by Equation 4.2. Inner, outer and clump pixels are color coded as red, grey and yellow respectively. The dashed and solid elliptical apertures denote the half-mass (light) radius (R_e) and $2R_e$ respectively. Panels (h), (i), (j) and (k) respectively show the rest-frame ($U - V$) color map and the mass, U_{rest} , and V_{rest} profiles. The dashed lines separate the $(\Sigma/\Sigma_e, R/R_e)$ space into the three different sections. Indeed, in cases where clumpy regions are visible in the composite and rest-frame ($U - V$) images, these regions show up as elevated surface brightness in the normalized profiles.



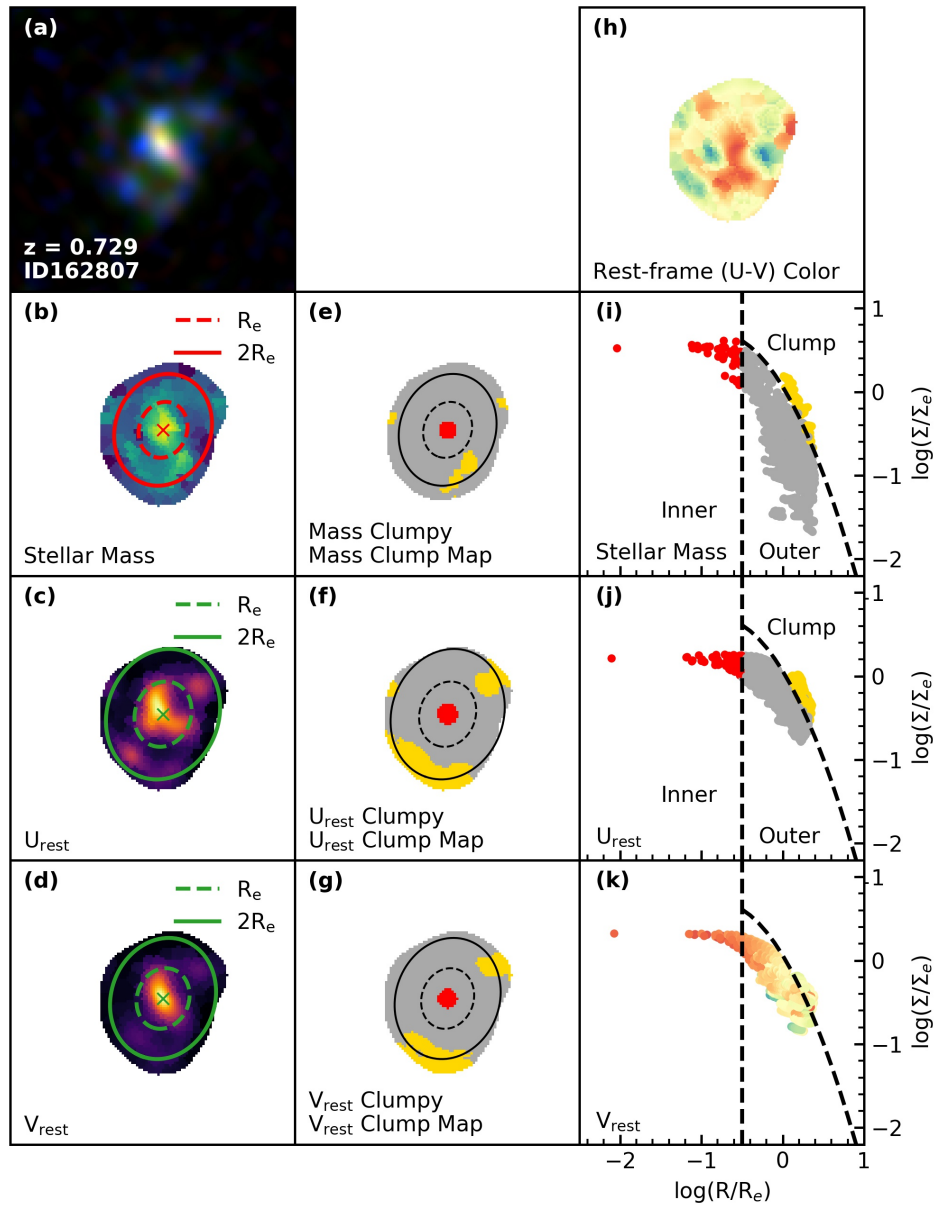
(b)

Figure 4.2: An example of how the normalized profiles are used to classify the morphology of galaxies. The galaxy is shown mainly for its clumpy morphology. Note that the galaxy is defined as clumpy in the rest-frame U luminosity, however its morphology is not clumpy in the rest-frame V luminosity since its clumpy components contribute less than 8% of the total rest-frame V luminosity.



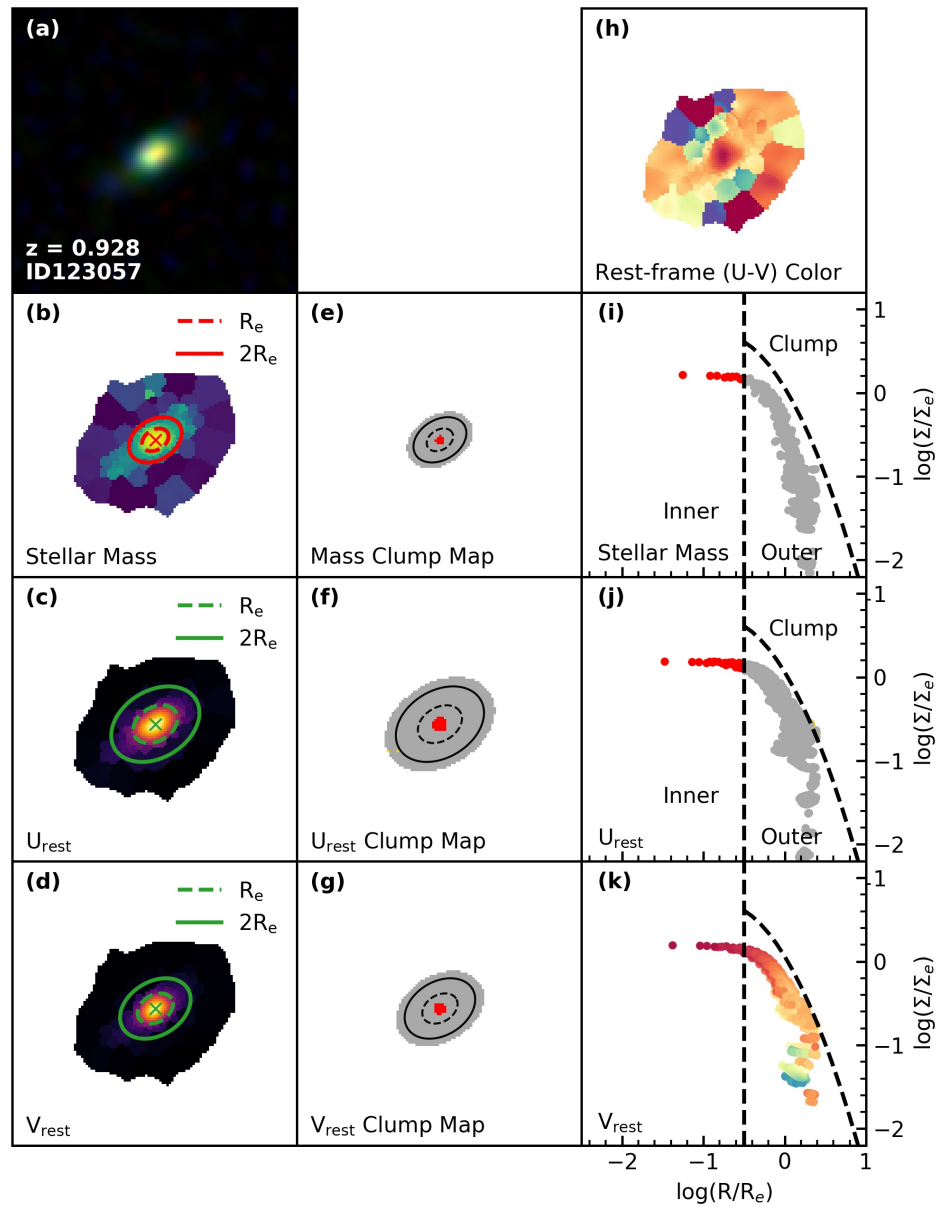
(c)

Figure 4.2: Another example of how the normalized profiles are used to classify the morphology of galaxies. The galaxy is shown, again, mainly for its clumpy morphology. Similar to ID240419, the galaxy is defined as clumpy in the rest-frame U luminosity, however its morphology is not clumpy in the rest-frame V luminosity.



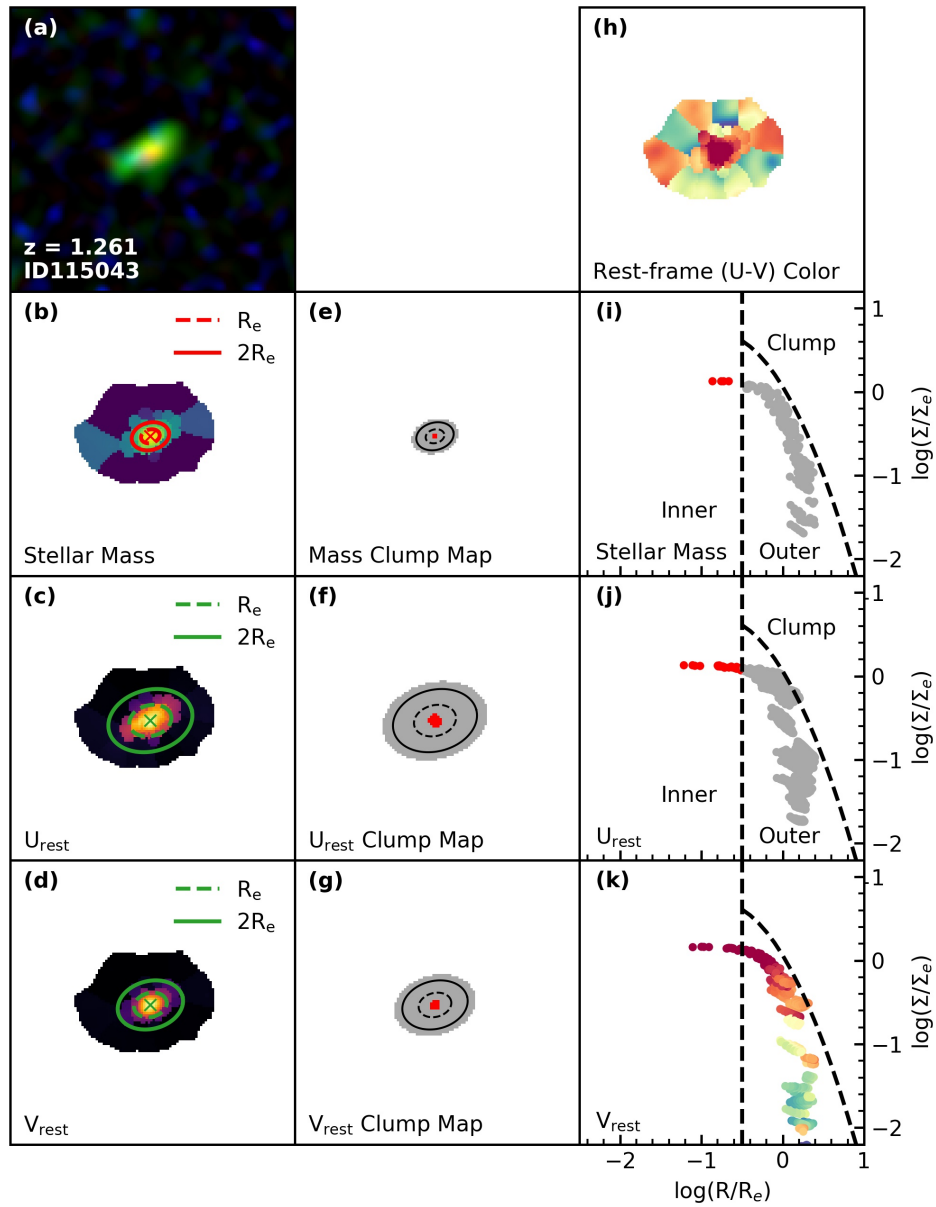
(d)

Figure 4.2: Another example of how the normalized profiles are used to classify the morphology of galaxies. The galaxy is shown, again, mainly for its clumpy morphology. For this galaxy, its morphology is clumpy in all the rest-frame luminosity and stellar mass distribution maps. Interestingly, its clumpy components in the stellar mass distribution map do not correspond to the clumps identified based on the rest-frame luminosities.



(e)

Figure 4.2: An example of the normalized profiles for non-clumpy star-forming galaxies. In this case, the galaxy has smooth light and mass profiles, which are shown in the normalized profiles. The normalized surface brightness and surface mass density fall off with further distance from the mass-weighted center.



(f)

Figure 4.2: Another example of the normalized profiles for non-clumpy star-forming galaxies. Similar to ID123057, its light and mass profiles are smoother, which can be seen within the normalized profiles. As such, the galaxy has been labeled as non-clumpy.

not be perfectly calibrated, significant biases in SED modelings can be introduced when fitting stellar population models to individual pixels. We implement a new binning strategy so that a minimum S/N is reached in either the K_s or rest-frame U band for each bin. Binning pixels together also serves other purposes for deconvolved images. While light profiles may not be accurate, flux is conserved. Therefore, the flux measured for a bin is representative of the underlying stellar populations. Furthermore, noise amplification from deconvolution can result in artificial clumpy structures for some deconvolved images. However, because noise is not correlated between the different photometric data, fitting stellar population models across 14 photometric bands will average the error in flux measurements.

We create the normalized profiles using resolved stellar population and color maps to study the spatial variation of the stellar populations. The profiles enable us to simultaneously quantify the dependence of stellar properties on surface brightness and galactocentric distance. We split the 2-dimensional profiles into three regions; notably, clumpy pixels are defined to have a normalized surface brightness (mass) above the normalized inner surface brightness (mass), and have a distance greater than the effective radius (see Section 4.5.3). Using this definition for clumpy pixels, a galaxy is classified as clumpy in luminosity (mass) if at least 8% of its total luminosity (mass) originate from its clumpy pixels.

Chapter 5

Results

As mentioned in the introduction, the mechanisms behind clump formation have not been fully understood, even with substantial observational efforts. There are two mechanisms that have been proposed to explain clump formation in distant galaxies, (1) *in-situ* origins from the violent disk instabilities (VDI) and (2) *ex-situ* origins from galaxy interaction/mergers. While differentiating between the two mechanisms is possible with integral-field-units spectroscopic observations, these observations are expensive owing to the need for long integration time in order to analyse the kinematics of distant galaxies. Another approach is to probe the abundance of clumpy galaxies. In particular, comparing the fraction of clumpy SFGs (the clumpy fraction; f_{clumpy}) between observations and theoretical predictions can help constrain the evolutionary path of clumpy star-forming galaxies.

The following sections focus on the study of clumpy SFGs using the latter approach. We measure the clumpy fractions based on the luminosity and stellar mass maps ($f_{\text{clumpy}}^{U_{\text{rest}}}$, $f_{\text{clumpy}}^{V_{\text{rest}}}$, $f_{\text{clumpy}}^{\text{mass}}$), and show their evolution with redshift. We also compare our measurements to other studies based on HST imaging, and further show the robustness of FIREDEC in resolving clumpy structures. Finally, we investigate the dependencies of the star-forming clumps on the intrinsic properties (e.g. stellar mass and star formation rate) of the host galaxy.

5.1 The Clumpy Fractions

We present the clumpy fractions for star-forming galaxies at $0.5 < z < 2$ using the luminosity and stellar mass maps. Since the rest-frame U and V continuum emission trace different stellar populations, it is worthwhile to investigate how the clumpy fractions vary between the two bands.

Mass Bin	Detection Map	C	α
$9.8 < \log(M_*/M) < 10.2$	U_{rest}	0.750 ± 0.048	-0.362 ± 0.093
	V_{rest}	0.284 ± 0.036	0.118 ± 0.182
	Mass	0.204 ± 0.030	0.828 ± 0.205
$10.2 < \log(M_*/M) < 10.6$	U_{rest}	0.491 ± 0.065	0.266 ± 0.167
	V_{rest}	0.189 ± 0.017	0.547 ± 0.113
	Mass	0.051 ± 0.018	2.015 ± 0.407
$10.6 < \log(M_*/M)$	U_{rest}	0.390 ± 0.043	0.373 ± 0.127
	V_{rest}	0.131 ± 0.039	0.562 ± 0.340
	Mass	0.019 ± 0.009	2.411 ± 0.498

Table 5.1: We list the values obtained from fitting the clumpy fractions to the form $C(1+z)^\alpha$. In general, we find that the clumpy fraction of low-mass systems evolve slowly compared to higher mass systems. For a given mass bin, we find that the clumpy fraction evolves strongly with redshift when using the stellar mass distribution maps, follows by the V_{rest} and U_{rest} luminosity maps.

5.1.1 Evolution of f_{clumpy}

The clumpy fractions and their evolution with redshift are shown in Figure 5.1. We bin each clumpy fraction into different mass bins. From the top to bottom panel, the clumpy fraction is measured based on the U_{rest} luminosity, V_{rest} luminosity, and the stellar mass distribution map. We find that the clumpy fraction changes considerably based on which map is used to identify clumps, with the f_{clumpy} dropping by $\sim 30\%$ when using the V_{rest} compared to the U_{rest} . When clumps are identified using the stellar mass maps, we find that there is only minor differences between $f_{\text{clumpy}}^{\text{mass}}$ and $f_{\text{clumpy}}^{V_{\text{rest}}}$ at each redshift bin.

Massive galaxies appear to have a lower fraction of clumpy morphologies. This is particularly true for $f_{\text{clumpy}}^{\text{mass}}$ and $f_{\text{clumpy}}^{V_{\text{rest}}}$. We also find that there is a slight evolution in the clumpy fractions for the intermediate and high-mass bin, dropping by $\sim 10\%$ from the highest redshift bin to the lowest redshift bin. However, the slope of the clumpy fraction for U_{rest} and V_{rest} appears to flatten out toward lower redshifts. To further investigate the evolution of the clumpy fractions, we fit the clumpy fractions to the form, $C(1+z)^\alpha$. The values are listed in Table 5.1. The clumpy fraction for low-mass systems appear to evolve slightly with redshift as opposed to higher mass systems. Note that while $f_{\text{clumpy}}^{U_{\text{rest}}}$ for the low-mass bin appears to decrease toward higher redshift, this result is likely affected by a non-complete mass sample toward higher- z . Furthermore, the slope of the clump fractions changes depending on which map is used to identify clumps. In particular, $f_{\text{clumpy}}^{\text{mass}}$ evolves more strongly with redshift, follows by $f_{\text{clumpy}}^{V_{\text{rest}}}$ and $f_{\text{clumpy}}^{U_{\text{rest}}}$.

The dependency of the clumpy fraction on the observed wavelength suggests that this result is driven by the wavelength-dependent resolution effect. However, we iterate that images are deconvolved to a target resolution of $0.1''$. The observed wavelength-dependency of the clumpy fraction therefore originates from real, intrinsic properties of the stellar populations. One cause for concern

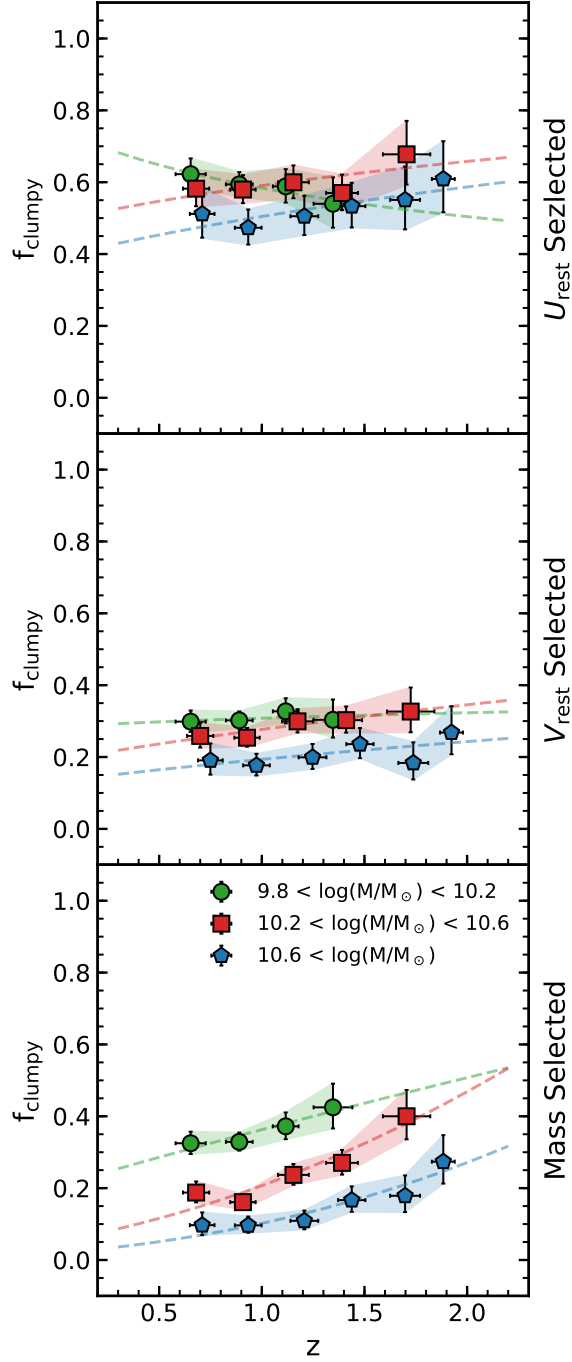


Figure 5.1: The evolution of the clumpy fractions. From top to bottom, clumpy galaxies are identified based on the rest-frame U luminosity, V luminosity, and the stellar mass distribution map. The green, red and blue markers are the clumpy fraction of the low, intermediate, and high-mass bin respectively. The best-fit slopes for the clumpy fraction evolution are given in Table 5.1 and are plotted as the dashed lines.

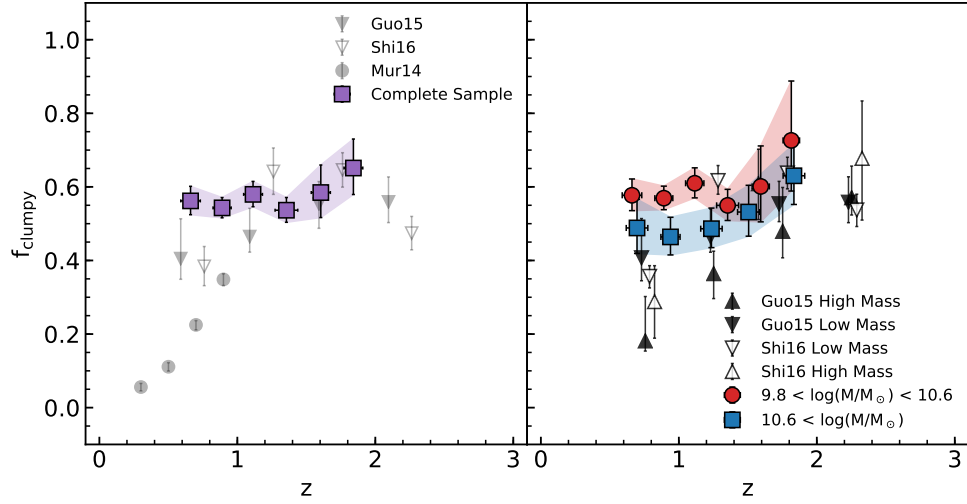


Figure 5.2: Comparison of $f_{\text{clumpy}}^{U_{\text{rest}}}$ to other studies based on HST imaging. The left shows the clumpy fraction derived from different studies. Our clumpy fraction based on the rest-frame U luminosity map are shown as the purple squared markers. The grey markers are the values obtained from other studies. In general, our measurements using the deconvolved images are consistent with other studies. The right panel shows $f_{\text{clumpy}}^{U_{\text{rest}}}$ binned in the low and high-mass bins.

is that it may be more difficult to detect low S/N clumps in low-mass galaxies. Since clumps are defined based on the fractional luminosity to ensure that only bright star-forming regions, which are associated with violent disk instabilities, are considered in our analysis, it is intuitive that only bright clumps will stand out against the low surface brightness of low-mass galaxies. We note that while our observed fraction for low-mass galaxies may be biased toward lower values, previous studies on the clumpy fraction are affected by a similar bias.

5.1.2 Comparison to Other Studies based on HST Imaging

In the previous chapter, we empirically validated deconvolution by comparing deconvolved images to HST images. We can further test whether the resolved structures are intrinsic (i.e. not deconvolution artifacts) by comparing our clumpy fractions with other measurements based on HST imaging (e.g. Wuyts et al. 2012, Murata et al. 2014, Shibuya et al. 2016). Note that these studies used a different method of identifying clumpy galaxies, and also differed in terms of sample size, redshifts and photometric filters. Due to these differences, the following comparison is not perfect, but it can serve as a fiducial test for whether deconvolution quantitatively provides similar fractions and overall trends.

The left panel of Figure 5.2 shows the comparison between the clumpy fraction for the complete sample. In general, the overall distribution of our values is consistent with other measurements. We find that the measured f_{clumpy} evolves slightly with respect to redshift, dropping from ~ 0.65 at

$z \approx 2$ to ~ 0.55 at $z \approx 0.5$. Wuyts et al. (2012) were only able to measure the clumpy fraction at two different redshift bins due to their small sample size. They found that there is a slight decrease in the clumpy fraction with decreasing redshift, going from 0.6 to 0.57. Similarly, both Guo et al. (2015) and Shibuya et al. (2016) reported values that are also in alignment with ours, with the clumpy fraction measured to be ~ 0.5 at $z \approx 2$ and ~ 0.4 at $z \approx 0.5$. There are some inconsistencies between our measurements and those reported by Murata et al. (2014) for clumpy fractions between $0.2 < z < 1$. They found a steeper slope with respect to redshift, with f_{clumpy} dropping from 0.35 at $z \sim 1$ to 0.05 at $z \sim 0.2$. However, note that these measurements are the only one based on a single filter (HST/ACS I_{F814W} -band) to define clumpiness at all redshifts, and could be explained as an effect of the morphological K-correction (which will be discussed in Section 6.4).

The right panel of Figure 5.2 compares the clumpy fractions at different mass bins. For consistency of comparison with the literature, we split our sample into a low-mass bin at $9.8 < \log(M_*/M_\odot) < 10.6$, and a high-mass bin at $10.6 < \log(M_*/M_\odot)$. We find that the overall trends are in agreement, with the clumpy fraction to be higher for lower mass galaxies and the slight decrease in the clumpy fraction toward lower redshifts. However, at lower redshifts, we find some discrepancies between our values and those reported in Guo et al. (2015) and Shibuya et al. (2016). In particular, their fractions are 0.15 (0.3) lower than ours from the low-mass (high-mass) bin.

5.2 The Star-Forming Main Sequence of Clumpy Galaxies

Since star formation rates and stellar masses are fundamental properties of galaxies, an intriguing question to ask is whether the morphology of a galaxy is affected by its relative position to the star-forming main sequence in the M_* -SFR parameter space.

In Figure 5.3, we show the density plot of clumpy and regular galaxies on the M_* -SFR diagram in the left and middle panel respectively. We separate our sample into two different redshift bins, with one bin at $z < 1$ and another at $z \geq 1$. The solid red line denotes the star-forming main sequence relation from Whitaker et al. (2012) using a fiducial redshift of 0.75 and 1.5 for the low and high redshift bin respectively. Both clumpy and regular SFGs have a similar range in SFRs at a given mass bin, however clumpy SFGs appear to have higher SFRs. Indeed, when normalizing the star formation rate by stellar mass, we find that higher- z galaxies typically show higher sSFRs. We further investigate this by plotting the fraction of clumpy galaxies as a function of SFR and stellar mass in the right panel. In general, we find that clumpy galaxies tend to occupy the upper envelope of the main sequence with high sSFRs, while most regular galaxies have low sSFRs.

Although bias could be introduced as a result of finer SFR and stellar mass binning, the result is still in good agreement with the result of Murata et al. (2014). They found that the distribution of clumpy SFGs tends to skew toward higher sSFR values. Furthermore, they investigated the distribution of all galaxies within the M_* -SFR parameter space, and reported that clumpy SFGs

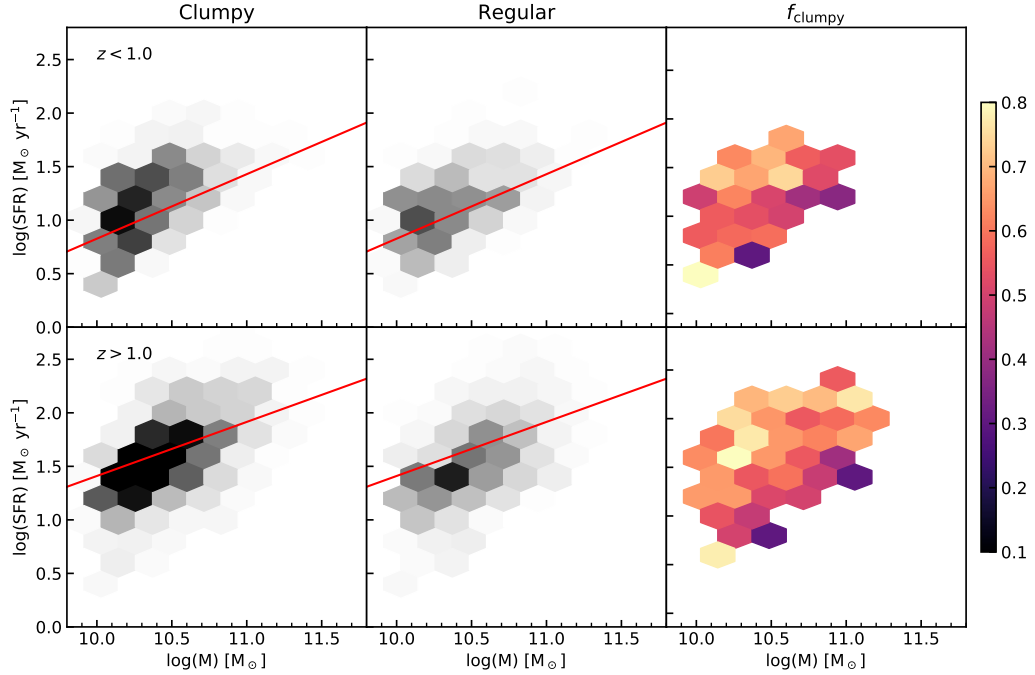


Figure 5.3: We show the distribution of SFGs in the M_* -SFR diagram. We separate our sample into two redshift bins, with the low- z bin ($z < 1$) in the top row and the high- z bin ($z \geq 1$) in the bottom row. From left to right, we show the density plot of clumpy SFGs, regular SFGs, and the clumpy fraction. The red line is the SFMS from Whitaker et al. (2012) using the fiducial redshift of 0.75 (1.5) for the low- z (high- z) bin.

mainly lie along the main sequence, while regular SFGs show a bimodality in their distribution. The bimodality consists of passive evolving galaxies at high stellar masses and main sequence galaxies for $\log(M_*/M_\odot) < 10.5$. Furthermore, the result above is consistent with the observed evolution of the clumpy fraction if star formation rate (and ultimately the gas mass fraction) is the driver of higher clumpy fractions. Figure 5.1 shows an increase of the clumpy fractions toward higher redshifts, where galaxies have higher SFRs (e.g. see 5.3). The gas mass fraction is also observed to increase toward higher redshifts (Tacconi et al., 2010). Indeed, if the observed scaling relation between molecular gas and SFR holds here (e.g. molecular Kennicutt-Schmidt surface density relation, Genzel et al. 2010), these observations can potentially provide a self-consistent picture that links higher SFR and/or higher gas fraction to clumpy morphologies.

5.3 Summary of the Results

We use the derived luminosity and stellar mass distribution maps to classify galaxies as clumpy or regular. We find that the morphology of galaxies changes with respect to their luminosities or stellar mass distribution; in general, $f_{\text{clumpy}}^{V_{\text{rest}}}$ and $f_{\text{clumpy}}^{\text{mass}}$ are similar, while $f_{\text{clumpy}}^{U_{\text{rest}}}$ is higher than

both of these fractions. The clumpy fractions also depend on the mass and star formation rate of the galaxies. When isolating for stellar mass, we find that f_{clumpy} is lower for massive galaxies. The evolution of the clumpy fractions is shallow, dropping $\sim 10\%$ from the high- z bin to low- z bin. However, for the low-mass bin, we see little to no evolution in the clumpy fraction. When considering both the stellar mass and star formation rate, we find that clumpy SFGs tend to occupy the upper envelope of the star-forming main sequence, while regular SFGs tend to occupy the lower envelope. In particular, at fixed stellar mass, clumpy galaxies in general have higher SFRs in comparison to the average star-forming galaxies at that redshift.

We also compare our observed clumpy fractions to other studies based on HST images. We show that our results, which are measured from the deconvolved ground-based images, are in general consistent with these studies. In particular, we found that the clumpy fractions that are comparable to one another, and our observed trends on the clumpy morphologies are also seen in the HST images. We would like to note that these results show that image deconvolution is a powerful tool that should be considered for future studies. The *Hubble Space Telescope* and *James Webb Space Telescope* are impressive observatories that should be used to their fullest potential. However, these observatories are not suited for surveying a large area of the sky in multiple filters. One major advantage of image deconvolution is the ability to capitalize on the existing and extensive ground-based surveys, and to provide resolved stellar population maps for millions of galaxies. Of course, there are disadvantages to image deconvolution, but note that in this study, we have shown that this tool can be used to broadly study the morphology of galaxies, with measurements that are comparable to those found based on HST imaging. In the future, it might be ideal to use image deconvolution in conjunction with space-based observatories to fully understand the nature of star-forming clumps.

Chapter 6

Discussion

In this chapter, we investigate how the clumpy fraction changes as galaxies evolve in mass. We continue our discussion on why clumpy galaxies have higher sSFRs compared to regular galaxies for a given mass bin, aiming to link high- z clumpy galaxies to the local descendants. Furthermore, we show that our results are consistent with different models for clump formation. Lastly, we address the possible biases in the measured clumpy fractions in different studies.

6.1 Evolution of Clumpy SFGs

Figure 5.1 shows the evolution of f_{clumpy} at fixed stellar mass. Galaxies, however, do not evolve at fixed stellar mass over cosmic time. As they evolve, their stellar mass can grow in several ways, which include mergers and *in-situ* star formation. Inferring the mass assembly history of galaxies can be challenging, as it requires us to accurately link progenitors to descendants. This process is complicated by the fact that galaxies can only be observed at one snapshot in time. However, it is possible to connect descendant galaxies to their likely progenitors by observing how galaxy populations in different parameter spaces (e.g. number density) evolve, an endeavor that requires mass-complete censuses of galaxies at different redshifts. The simplest method to derive the progenitor masses is through cumulative number density selection. This method begins with the assumption that the cumulative number density of galaxies would remain constant when there are no mergers, while the effect of mergers on the cumulative density can be predicted from models (e.g. Behroozi et al. 2013).

In fact, Hill et al. (2017) inferred the evolution of different galaxy masses over time by connecting observed mass functions to the number densities of Behroozi et al. (2013). Using the derived mass evolution from Hill et al. (2017), we show the subsequent evolution of the clumpy fractions for the progenitors of galaxies with $\log(M_*/M_\odot) \sim 10.85$ and $\log(M_*/M_\odot) \sim 10.35$ at $z \sim 0.65$ as the circle and square markers respectively in Figure 6.1. We find that the clumpy fractions decrease as galaxies

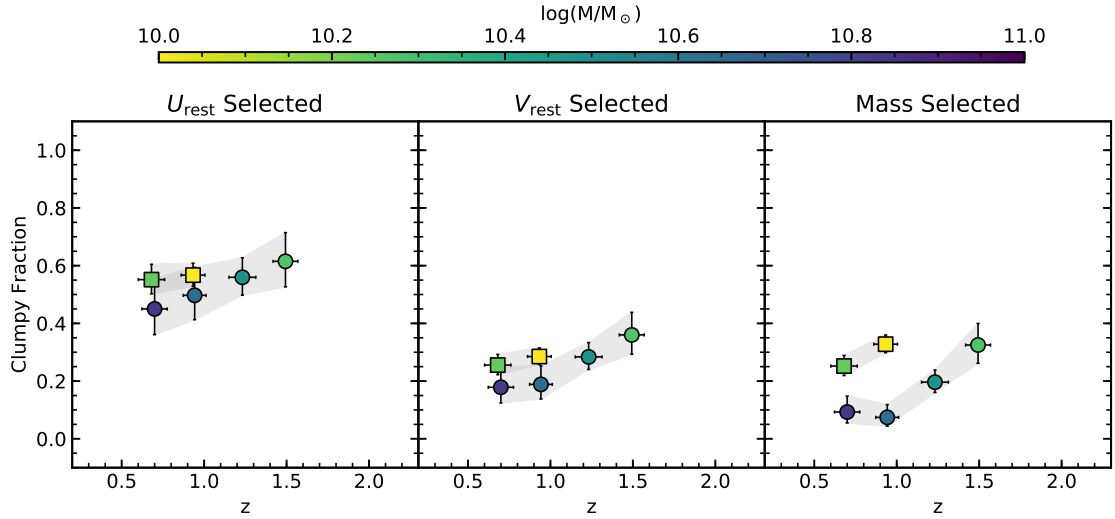


Figure 6.1: We show the evolution of clumpy fraction for the progenitors of galaxies with masses of $10^{10.85} M_{\odot}$ and $10^{10.35} M_{\odot}$ (the circle and square markers respectively) at redshift of 0.65. The mass evolution is obtained from Hill et al. (2017), by connecting the observed mass functions to the galaxy number density of Behroozi et al. (2013). At lower redshifts, only low-mass systems exhibit clumpy morphologies, while the same clumpy fraction is observed in more massive galaxies at higher redshift. This result is consistent with the down-sizing picture in the clumpy morphology.

grow in stellar mass. This mass dependency suggests the interplay between the formation of clumps, the availability of gas, and galaxies’ mass. Indeed, cosmological simulations predict that cold gas accretion rate decreases at lower redshifts (Kereš et al. 2005; Dekel & Birnboim 2006), where gas accretion in intermediate and high-mass systems is mainly dominated by hot mode accretion. With the suppressed supply of gas for star formation, galaxies will passively evolve into the “red and dead” populations. Our result is therefore not inconsistent with clump formation via disk fragmentation within an unstable gas-rich disk that is being supplied with cold, pristine gas accretion.

Furthermore, when comparing the clumpy fractions for the two descendant populations, we find that the lower mass descendants exhibit higher clumpy fractions at all redshift bins. This result is consistent with the so-called “down-sizing effect” in the clumpy morphology, which have been noted in several studies (e.g. Elmegreen et al. 2009b, Murata et al. 2014). While massive galaxies can exhibit a clumpy morphology at higher redshifts, such clumpy morphologies are more common in low-mass systems such as dwarf irregular galaxies in the local universe.

6.2 Connecting High- z Galaxies to Low- z Galaxies

The current picture of galaxy evolution consists of mass growth via star formation, dictated mainly by the galaxy’s dark matter halo mass. As the dark matter halo mass is correlated to the stellar mass, the star formation rate and stellar mass of galaxies is observed to have a tight relation, known

as the main sequence of star-forming galaxies. Observing the star formation rate and stellar mass of galaxies enable us to directly study the process in which gas is converted into stars, and subsequently the stellar mass build-up.

It is perhaps not surprising that clumpy and regular SFGs are distributed a certain way in the M_* -SFR parameter space, where clumpy SFGs mostly have higher specific star formation rates compared to regular SFGs (see Figure 5.3). The consistency between the clumpy fractions and SFRs at higher redshifts suggest that the gas fraction could indeed be the key factor in clumpy morphologies. The distribution of clumpy SFGs along the main sequence could be explained via clump fragmentation within the unstable gas-rich disk, which leads to a burst of star formation that sends them toward higher sSFRs. This idea is similar to what was observed in Tacchella et al. (2016), where they found galaxies to oscillate up and down the main sequence. In their simulations, galaxies reaches the upper envelope as the result of intense gas inflow (either from mergers or counter-rotating streams, and can be associated with violent disk instability), leading to higher star formation.

Similar results that relate irregular morphologies, SFRs and gas are also observed within the local universe. Note that in the local universe, galaxy morphologies are classified based on the Hubble Sequence, with late-type galaxies referring to spirals and irregulars, and early-type galaxies referring to ellipticals. Eales et al. (2017) found that galaxy morphologies change systematically with respect to the specific star formation rate (sSFR) and stellar mass, where late-type galaxies have higher sSFRs at lower masses and early-type galaxies are typically more massive with lower sSFRs. As late-type galaxies tend to have a higher gas reservoir compared to early-type galaxies (Calette et al., 2018), the change in galaxy morphologies in the local universe can be explained through the availability of gas for star formation.

6.3 The Role of Mergers in the Formation of Clumpy SFGs

Galaxy mergers can induce star-forming clumps as gravitational interaction can cause disturbances within the cold gas distribution of the disks. Mergers can be classified in a number of ways, but the most common classifications are based on the comparative size of the merging galaxies and the abundance of gas within them. For example, minor mergers refer to mergers where one of the galaxies is significantly smaller than the other, typically having a mass ratio between 1:10 and 1:4. Similarly, major mergers refer to mergers where the mass ratio of the merging galaxies is greater than 1:4. The merger of two gas-rich galaxies is known as wet mergers, while the merger of two gas-poor galaxies is referred as dry mergers. When the merging galaxies consist of both gas-rich and gas-poor galaxies, the merger is known as mixed. In this section, we address whether mergers are an important mechanism for clump formation by comparing the evolution of different clumpy fractions between $0.5 < z < 2$.

When analyzing the clumpy fraction of our sample, it is particularly intriguing that there are

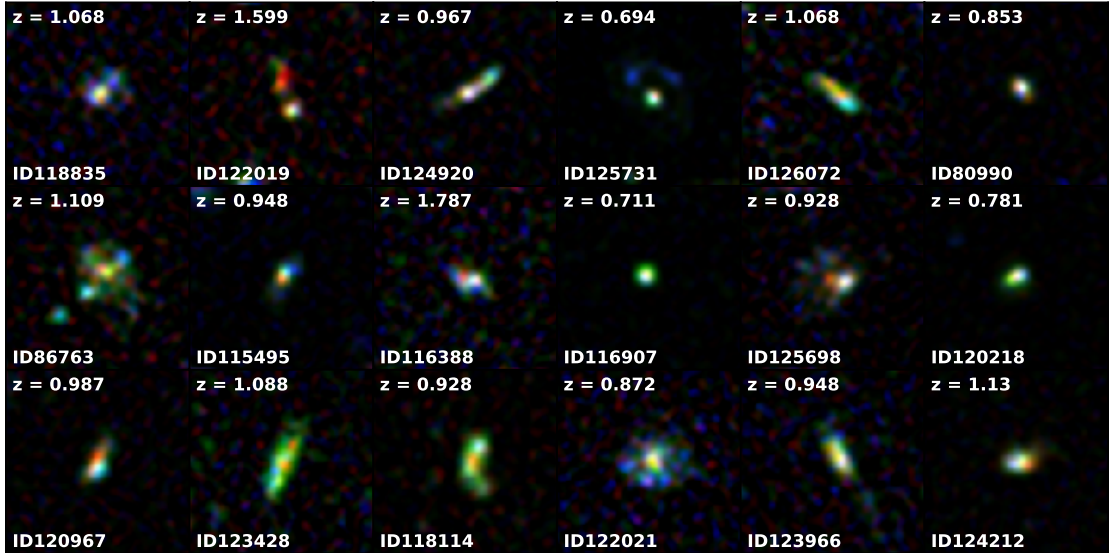


Figure 6.2: We show the deconvolved postage stamps for a few galaxies that are identified as clumpy in its stellar mass distributions. These galaxies are randomly selected from the central regions of COSMOS, with $10.1 < \log(M_*/M_\odot) < 10.6$ and $0.65 < z < 1.8$. While most galaxies show extended features, there are a few cases where the galaxies appear to be isolated with no irregular features (eg. ID80990, ID,115495, ID116907, ID120218).

a selection of galaxies which are identified as clumpy in its stellar mass distribution. We show the deconvolved postage stamps for a few galaxies that are clumpy in stellar mass distribution in Figure 6.2. Recall that a galaxy is classified as clumpy in its stellar mass distribution if pixels originating from the clump regime of the normalized mass profile contribute to at least 8% of the total mass of the galaxy. In this sense, the clumpy stellar mass component already constitutes a sizeable mass compared to its host galaxy, and could potentially be an *ex-situ* satellite. In the following discussion, we interpret clumpy-in-mass galaxies as galaxies in the process of accreting satellites or merging. We iterate that other structures could be the cause (e.g. spiral arms), so this interpretation is an upper limit on the accretion of satellites.

If mergers play a role in clump formation, the clumpy fractions based on the stellar mass and U_{rest} distribution are expected to be correlated with one another. Figure 6.3 shows these the clumpy fractions for galaxies identified as clumpy in stellar mass, and clumpy in both stellar mass and U_{rest} as a function of redshift and mass. At first glance, their evolution appears to be correlated. However, when looking at the fraction of clumpy-in-mass galaxies that are also clumpy in U_{rest} (e.g. the grey marker), we find that this fraction is decreasing toward lower redshifts. In the high-mass bin, the fraction decreases from 0.85 at $z \sim 1.85$ to ~ 0.7 toward lower redshifts. This trend is also seen in the intermediate mass bin. While the lower-mass bin does not show this trend, we note that these low-mass systems are found at lower redshifts, and we find that the fraction is still low compared to both the intermediate and high mass bins.

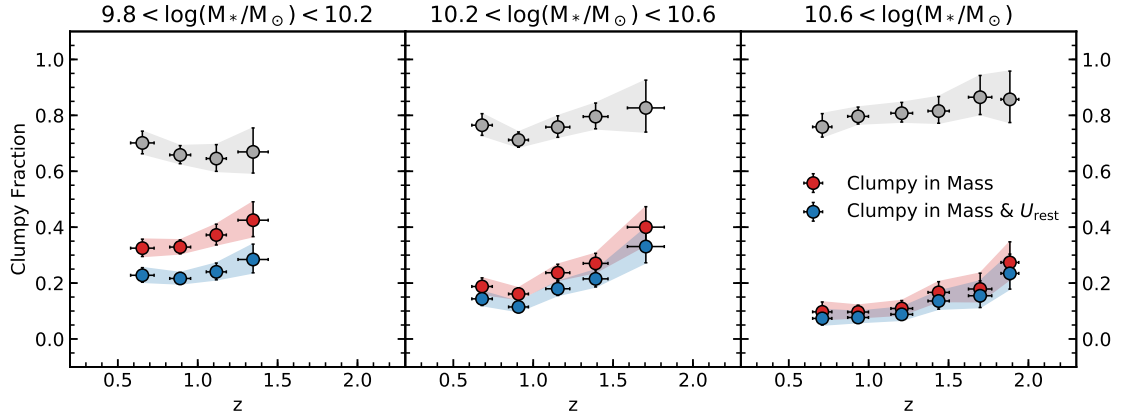


Figure 6.3: The red and blue markers show the fraction of galaxies that are clumpy in mass and clumpy in both mass and U_{rest} respectively. The grey markers show the fraction of clumpy-in-mass galaxies that are also clumpy in U_{rest} . At higher redshifts, most clumpy-in-mass galaxies are also seen as clumpy in luminosity, but this fraction decreases toward lower redshifts. This is shown in the intermediate and high mass bins. If the clumpy fraction based on stellar mass is taken as a proxy for mergers, the dependency of the fraction (i.e. the grey markers) on redshift imply that not all mergers are responsible for clumpy morphologies.

If clumpy-in-mass galaxies can be taken as a proxy for galaxy mergers, and clumpy-in- U_{rest} galaxies are the induced star-forming clumps, then the observed fraction suggests that not all mergers are likely to induce star-forming clumps. In particular, Di Matteo et al. (2008) suggested that gas-rich wet mergers can help induce disk fragmentation. Along with studies that found the wet merger rate to increase with redshift (e.g. Lin et al. 2008), these findings can explain the observed fraction in Figure 6.3. In this picture, wet mergers facilitate the formation of star-forming clumps in the high- z universe, while toward lower redshifts, other mechanisms of clumpy formation are taking place as the number of wet mergers decrease. We note that there are simulations which suggest that the number of clumps is only mildly enhanced for gas-rich interacting systems (Fensch et al., 2017). Therefore, in order to disentangle the plausible role of gas-rich mergers in inducing star-forming clumps, future studies should investigate the gas mass fraction of clumpy, interacting systems.

It is important to address some caveats. We stress that individual clumps cannot be distinguished based on the clump finding algorithm. Therefore, each clumpy component could be a superposition of smaller clumps, and not just one accreting satellite. Further, mergers can be associated with clumps in several ways. This discussion specifically focuses on the effects of galaxy mergers on the formation of clumps. However, accreting satellites can themselves be considered as clumps. For example, using a cosmological simulation, Mandelker et al. (2014) found that 25% of their identified clumps are likely to be merger remnants, and therefore have an *ex-situ* origin (i.e. these clumps have their own dark matter halo).

6.4 Possible Biases in Different f_{clumpy} Measurements

The discrepancies in the measured clumpy fractions shown in Figure 5.2 can be attributed to different data and methods of identifying clumps. In Murata et al. (2014), **SExtractor** is used to deblend galaxies so that individual bright clumps can be cataloged. Further, their analysis is based on the I_{814} image, which effectively probes the rest-frame 4000 Å (B band) and rest-frame 6000 Å (V band) for their highest and lowest redshift bins respectively. In Section 5.1, we have shown that f_{clumpy} is affected by the morphological K-correction, where the fraction of clumpy galaxies varies significantly depending on which wavelength is used to identify clumpy structures. In particular, a higher fraction is observed when using the rest-frame U band compared to the rest-frame V band. Note that this effect has also been observed in Wuyts et al. (2012). Accounting for the morphological K-correction, the slope of the clumpy fraction from Murata et al. (2014) would be dampened, and can better align their measurements to ours.

Guo et al. (2015) and Shibuya et al. (2016) used a different method of identifying clumps. In essence, a high-pass filter is used on the galaxy cutouts to isolate clumps since star-forming clumps are regions with a sharp and bright light profile. **SExtractor** is then used to automatically identify local peaks within the filtered image. To account for the morphological K-correction, they identified UV bright clumps using a selection of HST photometric bands, where Guo et al. (2015) used the $B_{435}V_{606}i_{775}Z_{850}$ images and Shibuya et al. (2016) used the $I_{814}V_{606}$ images. Since clumps are believed to be embedded in the galaxies, they also accounted for the background flux of the galaxies when measuring the photometry of clumps. Their fractions may be lower due to this harsher constraint on the flux of clump. However, it is still unclear whether the local background should be considered in clump studies as the uncertainty involved in estimating clump properties (e.g. from the treatment of background light) only allows for order-of-magnitude comparison between different clump samples. We choose not to account for the background in our analyses as we are mainly interested in the evolution of the clumpy fractions, and accounting for the background flux will not affect the observed trends.

Note that there are certainly some limitations with image deconvolution (e.g. slightly degraded resolution compared to HST's and degeneracy in the solutions) that can lead to differences between our measurements and others. However, considering these limitations, we show that with 14 filters and 10,000 galaxies, we have obtained results that are largely consistent with other studies that used HST. In addition, we have overcome the issues that HST (and future JWST) studies have with limited filter coverage and small sample size. While there are advantages and disadvantages associated with these two approaches, utilizing them complementary going forward will undoubtedly have an enormous potential in the study of star-forming clumps.

6.5 Summary of the Discussion

In this chapter, we investigate the evolution of clumpy galaxies, and test whether our results are consistent with theoretical models of clump formation. In order to connect progenitors to descendants, we use the derived mass evolution from Hill et al. (2017), which accounted for the changing galaxy number density from mergers. We find that galaxies are less likely to have a clumpy morphology as they are growing in mass. This observed dependency of the clumpy fraction on stellar mass is not inconsistent with models that suggest clump formation within an unstable gas-rich disk that is fueled by cold gas accretion. In this picture, the supplement of gas in massive galaxies at low redshift is limited as cold mode accretion is suppressed. With gas supply shuts off and existing cold gas reservoir being consumed, the mode of star formation is eventually turned off, allowing galaxies to passively evolve toward the lower envelope of the star-forming main sequence diagram. We also investigate the role of mergers on clump formation. We use clumpy-in-mass galaxies as a proxy for mergers with the motivation that the stellar mass component already has a sizeable mass compared to its host galaxy. If mergers have an effect on clump formation, we expect $f_{\text{clumpy}}^{U_{\text{rest}}}$ and $f_{\text{clumpy}}^{\text{mass}}$ to be correlated. Instead, we found that the fraction of clumpy galaxies that are clumpy in both mass and U_{rest} is dependent on redshift, decreasing toward lower redshifts. This suggests that not all mergers are responsible for star-forming clumps.

Chapter 7

Conclusions

The avalanche of observational data over the past decades has given us a broad understanding of the stellar mass growth of galaxies over much of cosmic time. However, the detailed physics of how and where galaxies built up their stellar masses to become present-day galaxies is still an enigmatic topic in astronomy.

Studying the evolution of galaxies during the epoch of cosmic star formation can shed light on the stellar mass assembly of galaxies. With the prominence of irregular galaxies that host kiloparsec-scale, star-forming clumps during this period, it is highly possible that these star-forming regions play a role in shaping how galaxies evolve. Indeed, the fate of clumps is often suggested to be responsible for building up the progenitor of present-day galactic bulges and disks. Although clumpy galaxies are ubiquitous at higher redshifts, there is still a lack of observational constraints on their origin and evolution. Specifically, resolved studies of high- z galaxies can only be done with HST, or ground-based observatories aided by adaptive optics technologies. These types of observation are time-intensive, and therefore are generally limited to smaller samples of galaxies.

In this study, we present a novel approach to resolve galaxies at the kiloparsec-scale in ground-based images of the COSMOS field. This is done by using image deconvolution (the algorithm is called finite resolution deconvolution). While deconvolution can introduce uncertainties in the light profiles, this drawback is mitigated by the fact that the study has access to a much larger sample of galaxies compared to the other existing HST studies. Indeed, the COSMOS field is roughly 2 square degrees, which enables us to select 22960 star-forming galaxies at $0.5 < z < 2$ based on a rest-frame color cut, a stellar mass cut at $10^{9.8} M_{\odot}$, and an integrated S/N cut of 20 in the K_s band.

We further stress that image deconvolution is the ideal tool for this study. One key feature of finite resolution deconvolution is that images are deconvolved to a finite resolution to ensure that solutions are well-defined. Deconvolution toward a finite resolution enables us to define a target resolution of $0.1''$. This target resolution corresponds to a physical scale of ~ 0.7 kpc for our redshift range, which effectively is enough to resolve star-forming clumps that have been estimated to be

~ 0.9 kpc in size based on HST studies.

We list below a summary of the notable points and conclusions from this study.

1. Stars that are chosen for PSF modeling are unsaturated and unblended. The fitting process is done in two steps; first by fitting the profile of the PSF stars with an analytical fit, and then a numerical fit to capture any residual structures that were not fitted properly by the analytical fit. We carefully model the deconvolution kernel by varying the Lagrange parameter (λ_n), and checking the residuals of both the analytical and numerical fits.
2. We show that the residuals between the deconvolved $z+$ and PSF-matched I_{814} images are in general small. In the multi-wavelength comparison, structures that are resolved by deconvolution are also found in the HST/ACS images.
3. Pixels are binned together when inferring stellar properties from the deconvolved images. While the light profile of deconvolved images can have some uncertainties, the flux within a bin is representative of the underlying stellar populations. It is unlikely that noise is correlated across the different photometric data, and therefore, the SED modelling of the combined data will average out these errors.
4. In order to make use of the resolved luminosity and stellar mass distribution maps, we employ the normalized radial profiles of Wuyts et al. (2012). The normalized profiles enable us to simultaneously probe dependencies on colors, stellar mass, luminosities, and galactocentric distance.
5. We define 3 regimes in the parameter space of the normalized profile, with the clumpy regime representing the parameter space that contains pixels with enhanced luminosities or stellar mass relative to the underlying profile. It should be noted that the dividing lines are not analytically derived, but based on visual classification (see Wuyts et al. 2012).
6. Galaxies are distinguished between clumpy and regular based on how much of the total luminosity (or mass) is resided in pixels originating from the clumpy regime. In essence, a galaxy is labeled as clumpy in luminosity (mass) if 8% of its total luminosity (mass) comes from the clumpy regime.
7. We measure the clumpy fractions for star-forming galaxies as a function of redshift and stellar mass. We find that there is a slight evolution with redshift, dropping by ~ 0.15 from $z \sim 2$ to $z \sim 0.5$. We find that the clumpy fractions are also dependent on stellar mass, with massive galaxies showing lower clumpy fractions.
8. When investigating the clumpy fraction to both stellar mass and SFR, we find that clumpy galaxies are more likely to be located along the upper envelope of the star-forming main

sequence. In essence, for a given mass bin, clumpy galaxies have higher SFRs compared to the average star-forming galaxies at that redshift.

9. We compare our clumpy fractions to the measure clumpy fractions of other studies that are based on HST images, and found that these measurements are in general comparable with one another. This further indicates that the clumps resolved by deconvolution are real, and not artificially created.
10. We trace the progenitors to two populations of descendent galaxies at $z \sim 0.5$. We find that the clumpy fractions decrease as galaxies grow in mass. This is consistent with the downsizing picture, where clumpy morphologies are found mostly in low-mass systems in the local universe.
11. Finally, we test for evidences of clump formation from mergers. We make a basic assumption that clumpy-in-mass galaxies are galaxies that are in the process of merging, or accreting a satellite. We find that around 80% of clumpy-in-mass galaxies are also clumpy in U_{rest} at $z \sim 2$, but this percentage drop to 60% at $z \sim 0.5$. At face value, this suggests that not all mergers are responsible for clump formation.

7.1 Future Directions

In this work, we have shown that the deconvolved ground-based images provide consistent results as HST studies. Specifically, the comparison between the deconvolved and HST images, along with the comparison of the clumpy fractions, have shown that finite resolution deconvolution is robust. Combined with the extensive data of multi-wavelength images of COSMOS, this work showcases the potential of FIREDEC to provide resolved color and stellar population maps for thousands of galaxies. In the near future, we will release our catalog of the 22960 star-forming galaxies in COSMOS. The catalog will be the largest existing catalog with resolved stellar properties for intermediate redshift galaxies.

The future directions are exciting. Using new and well-test deconvolution algorithms on the enormous amount of ground-based imaging that are being taken by wide-field observatories, and those already in archives is the ideal next step. In particular, the *Vera C. Rubin Observatory* will survey two-third of the night sky over the next decade from the ground as part of the Legacy Survey of Space and Time program. Further, the Euclid space mission will map half the sky in the NIR, while ground-based observatories will supplement the optical part. Indeed, applying deconvolution to these data would allow for resolved stellar population mapping for hundreds of millions of galaxies. We hope that this initial study provide the frameworks that lead other investigators to consider the use of deconvolution in studies where it would be of use.

With the ability to resolve star-forming clumps in bright galaxies, we can also catalog clumps, from detailing their number counts to estimating their stellar mass and star formation rate. This catalog can act as useful observational constraints for numerical simulations that aim to investigate how well small-scale structures in the interstellar medium are reproduced in different stellar feedback, ISM, or subgrid models (e.g. Inoue & Yoshida 2019; Li et al. 2020). While there are limitations with FIREDEC to resolve and distinguish individual clumps in low S/N galaxies, the ability to broadly classify galaxies as clumpy or non-clumpy also presents an opportunity for astronomers to find clumpy candidates for further observations with space-based observatories. This is especially true for newer fields that are being observed with ground-based observatories.

As a final note, while our results do not provide definitive observational evidences for clump formation via cold mode accretion and/or mergers, they do provide additional hints that these mechanisms are responsible for clump formation in distant galaxies. To further investigate this, future studies should focus on the kinematic and gas properties of these galaxies in order to robustly understand these mechanisms. For example, isolated and clumpy galaxies can be linked to cold gas accretion by identifying whether they have more pristine gas compared to regular galaxies. On the other hand, identifying the gas fraction in mergers that show signs of clumpy morphologies can place observational constraints on whether wet mergers facilitate clump formation. Future studies such as these can bring additional insights on this enigmatic topic.

7.2 Final Words

We would like to acknowledge Pascale Jablonka and Frédéric Courbin for allowing us to use finite resolution deconvolution, and for their time in answering and diagnosing problems along the way. Once again, a special thank you to everyone who read and provided thoughtful comments on this work.

Bibliography

- Abraham, R. G., Tanvir, N. R., Santiago, B. X., Ellis, R. S., Glazebrook, K., & van den Bergh, S. 1996, *Mon. Not. R. Astron. Soc.*, 279, L47
- Aretxaga, I., Wilson, G. W., Aguilar, E., Alberts, S., Scott, K. S., Scoville, N., Yun, M. S., Austermann, J., Downes, T. P., Ezawa, H., Hatsukade, B., Hughes, D. H., Kawabe, R., Kohno, K., Oshima, T., Perera, T. A., Tamura, Y., & Zeballos, M. 2011, *Mon. Not. R. Astron. Soc.*, 415, 3831
- Baldry, I. K., Balogh, M. L., Bower, R. G., Glazebrook, K., Nichol, R. C., Bamford, S. P., & Budavari, T. 2006, *Mon. Not. R. Astron. Soc.*, 373, 469
- Beckwith, S. V. W., Stiavelli, M., Koekemoer, A. M., Caldwell, J. A. R., Ferguson, H. C., Hook, R., Lucas, R. A., Bergeron, L. E., Corbin, M., Jogee, S., & et al. 2006, *The Astronomical Journal*, 132, 17291755
- Behroozi, P. S., Marchesini, D., Wechsler, R. H., Muzzin, A., Papovich, C., & Stefanon, M. 2013, *Astrophys. J. Lett.*, 777, L10
- Bertin, E. & Arnouts, S. 1996, *Astron. Astrophys. Suppl. Ser.*, 117, 393
- Bournaud, F. 2016, in *Astrophysics and Space Science Library*, Vol. 418, *Galactic Bulges*, ed. E. Laurikainen, R. Peletier, & D. Gadotti, 355
- Bouwens, R. J., Illingworth, G. D., Oesch, P. A., Stiavelli, M., van Dokkum, P., Trenti, M., Magee, D., Labbé, I., Franx, M., Carollo, C. M., & Gonzalez, V. 2010, *Astrophys. J. Lett.*, 709, L133
- Brammer, G. B., van Dokkum, P. G., & Coppi, P. 2008, *The Astrophysical Journal*, 686, 1503
- Bruzual, G. & Charlot, S. 2003, *Monthly Notices of the Royal Astronomical Society*, 344, 1000
- Calette, A. R., Avila-Reese, V., Rodríguez-Puebla, A., Hernández-Toledo, H., & Papastergis, E. 2018, *Rev. Mexicana Astron. Astrofis.*, 54, 443
- Calzetti, D., Armus, L., Bohlin, R. C., Kinney, A. L., Koornneef, J., & Storchi-Bergmann, T. 2000, *The Astrophysical Journal*, 533, 682
- Cantale, N., Courbin, F., Tewes, M., Jablonka, P., & Meylan, G. 2016a, *Astron. Astrophys.*, 589, A81
- Cantale, N., Jablonka, P., Courbin, F., Rudnick, G., Zaritsky, D., Meylan, G., Desai, V., De Lucia, G., Aragón-Salamanca, A., Poggianti, B. M., Finn, R., & Simard, L. 2016b, *Astron. Astrophys.*, 589, A82
- Capak, P., Aussel, H., Ajiki, M., McCracken, H. J., Mobasher, B., Scoville, N., Shopbell, P., Taniguchi, Y., Thompson, D., Tribiano, S., Sasaki, S., Blain, A. W., Brusa, M., Carilli, C., Comastri, A., Carollo, C. M., Cassata, P., Colbert, J., Ellis, R. S., Elvis, M., Giavalisco, M., Green, W., Guzzo, L., Hasinger, G., Ilbert, O., Impey, C., Jahnke, K.,

- Kartalpe, J., Kneib, J. P., Koda, J., Koekemoer, A., Komiyama, Y., Leauthaud, A., Le Fevre, O., Lilly, S., Liu, C., Massey, R., Miyazaki, S., Murayama, T., Nagao, T., Peacock, J. A., Pickles, A., Porciani, C., Renzini, A., Rhodes, J., Rich, M., Salvato, M., Sanders, D. B., Scarlata, C., Schiminovich, D., Schinnerer, E., Scodreggio, M., Sheth, K., Shioya, Y., Tasca, L. A. M., Taylor, J. E., Yan, L., & Zamorani, G. 2007, *Astrophys. J. Suppl. Ser.*, 172, 99
- Cappellari, M. & Copin, Y. 2003, *Monthly Notices of the Royal Astronomical Society*, 342, 345
- Cava, A., Schaerer, D., Richard, J., Pérez-González, P. G., Dessauges-Zavadsky, M., Mayer, L., & Tamburello, V. 2018, *Nature Astronomy*, 2, 76
- Chabrier, G. 2003, *Publications of the Astronomical Society of the Pacific*, 115, 763
- Dekel, A. & Birnboim, Y. 2006, *Mon. Not. R. Astron. Soc.*, 368, 2
- Dekel, A., Sari, R., & Ceverino, D. 2009, *The Astrophysical Journal*, 703, 785
- Di Matteo, P., Bournaud, F., Martig, M., Combes, F., Melchior, A. L., & Semelin, B. 2008, *Astron. Astrophys.*, 492, 31
- Dickinson, M. 2000, in *Astronomy, physics and chemistry of H⁺₃*, Vol. 358, 2001
- Eales, S., de Vis, P., Smith, M. W. L., Appah, K., Ciesla, L., Duffield, C., & Schofield, S. 2017, *Mon. Not. R. Astron. Soc.*, 465, 3125
- Elmegreen, B. G. & Elmegreen, D. M. 2005, *Astrophys. J.*, 627, 632
- Elmegreen, B. G., Elmegreen, D. M., Fernandez, M. X., & Lemonias, J. J. 2009a, *Astrophys. J.*, 692, 12
- Elmegreen, D. M., Elmegreen, B. G., Marcus, M. T., Shahinyan, K., Yau, A., & Petersen, M. 2009b, *Astrophys. J.*, 701, 306
- Elmegreen, D. M., Elmegreen, B. G., Ravindranath, S., & Coe, D. A. 2007, *Astrophys. J.*, 658, 763
- Elvis, M., Civano, F., Vignali, C., Puccetti, S., Fiore, F., Cappelluti, N., Aldcroft, T. L., Fruscione, A., Zamorani, G., Comastri, A., Brusa, M., Gilli, R., Miyaji, T., Damiani, F., Koekemoer, A. M., Finoguenov, A., Brunner, H., Urry, C. M., Silverman, J., Mainieri, V., Hasinger, G., Griffiths, R., Carollo, C. M., Hao, H., Guzzo, L., Blain, A., Calzetti, D., Carilli, C., Capak, P., Etori, S., Fabbiano, G., Impey, C., Lilly, S., Mobasher, B., Rich, M., Salvato, M., Sanders, D. B., Schinnerer, E., Scoville, N., Shopbell, P., Taylor, J. E., Taniguchi, Y., & Volonteri, M. 2009, *Astrophys. J. Suppl. Ser.*, 184, 158
- Fensch, J., Renaud, F., Bournaud, F., Duc, P. A., Agertz, O., Amram, P., Combes, F., Di Matteo, P., Elmegreen, B., Emsellem, E., Jog, C. J., Perret, V., Struck, C., & Teyssier, R. 2017, *Mon. Not. R. Astron. Soc.*, 465, 1934
- Förster Schreiber, N. M., Shapley, A. E., Genzel, R., Bouché, N., Cresci, G., Davies, R., Erb, D. K., Genel, S., Lutz, D., Newman, S., Shapiro, K. L., Steidel, C. C., Sternberg, A., & Tacconi, L. J. 2011, *Astrophys. J.*, 739, 45
- Genzel, R., Tacconi, L. J., Eisenhauer, F., Förster Schreiber, N. M., Cimatti, A., Daddi, E., Bouché, N., Davies, R., Lehnert, M. D., Lutz, D., Nesvadba, N., Verma, A., Abuter, R., Shapiro, K., Sternberg, A., Renzini, A., Kong, X., Arimoto, N., & Mignoli, M. 2006, *Nature*, 442, 786
- Genzel, R., Tacconi, L. J., Gracia-Carpio, J., Sternberg, A., Cooper, M. C., Shapiro, K., Bolatto, A., Bouché, N., Bournaud, F., Burkert, A., Combes, F., Comerford, J., Cox, P., Davis, M., Schreiber, N. M. F., Garcia-Burillo, S., Lutz, D., Naab, T., Neri, R., Omont, A., Shapley, A., & Weiner, B. 2010, *Mon. Not. R. Astron. Soc.*, 407, 2091

- Grogin, N. A., Kocevski, D. D., Faber, S. M., Ferguson, H. C., Koekemoer, A. M., Riess, A. G., Acquaviva, V., Alexander, D. M., Almaini, O., Ashby, M. L. N., Barden, M., Bell, E. F., Bournaud, F., Brown, T. M., Caputi, K. I., Casertano, S., Cassata, P., Castellano, M., Challis, P., Chary, R.-R., Cheung, E., Cirasuolo, M., Conselice, C. J., Roshan Cooray, A., Croton, D. J., Daddi, E., Dahlen, T., Davé, R., de Mello, D. F., Dekel, A., Dickinson, M., Dolch, T., Donley, J. L., Dunlop, J. S., Dutton, A. A., Elbaz, D., Fazio, G. G., Filippenko, A. V., Finkelstein, S. L., Fontana, A., Gardner, J. P., Garnavich, P. M., Gawiser, E., Giavalisco, M., Grazian, A., Guo, Y., Hathi, N. P., Häussler, B., Hopkins, P. F., Huang, J.-S., Huang, K.-H., Jha, S. W., Kartaltepe, J. S., Kirshner, R. P., Koo, D. C., Lai, K., Lee, K.-S., Li, W., Lotz, J. M., Lucas, R. A., Madau, P., McCarthy, P. J., McGrath, E. J., McIntosh, D. H., McLure, R. J., Mobasher, B., Moustakas, L. A., Mozena, M., Nandra, K., Newman, J. A., Niemi, S.-M., Noeske, K. G., Papovich, C. J., Pentericci, L., Pope, A., Primack, J. R., Rajan, A., Ravindranath, S., Reddy, N. A., Renzini, A., Rix, H.-W., Robaina, A. R., Rodney, S. A., Rosario, D. J., Rosati, P., Salimbeni, S., Scarlata, C., Siana, B., Simard, L., Smidt, J., Somerville, R. S., Spinrad, H., Straughn, A. N., Strolger, L.-G., Telford, O., Teplitz, H. I., Trump, J. R., van der Wel, A., Villforth, C., Wechsler, R. H., Weiner, B. J., Wiklind, T., Wild, V., Wilson, G., Wuyts, S., Yan, H.-J., & Yun, M. S. 2011, *Astrophys. J. Suppl. Ser.*, 197, 35
- Guo, Y., Ferguson, H. C., Bell, E. F., Koo, D. C., Conselice, C. J., Giavalisco, M., Kassin, S., Lu, Y., Lucas, R., Mandelker, N., McIntosh, D. M., Primack, J. R., Ravindranath, S., Barro, G., Ceverino, D., Dekel, A., Faber, S. M., Fang, J. J., Koekemoer, A. M., Noeske, K., Rafelski, M., & Straughn, A. 2015, *The Astrophysical Journal*, 800, 39
- Guo, Y., Rafelski, M., Bell, E. F., Conselice, C. J., Dekel, A., Faber, S. M., Giavalisco, M., Koekemoer, A. M., Koo, D. C., Lu, Y., Mandelker, N., Primack, J. R., Ceverino, D., de Mello, D. F., Ferguson, H. C., Hathi, N., Kocevski, D., Lucas, R. A., Pérez-González, P. G., Ravindranath, S., Soto, E., Straughn, A., & Wang, W. 2018, *The Astrophysical Journal*, 853, 108
- Hasinger, G., Cappelluti, N., Brunner, H., Brusa, M., Comastri, A., Elvis, M., Finoguenov, A., Fiore, F., Franceschini, A., Gilli, R., Griffiths, R. E., Lehmann, I., Mainieri, V., Matt, G., Matute, I., Miyaji, T., Molendi, S., Paltani, S., Sanders, D. B., Scoville, N., Tresse, L., Urry, C. M., Vettolani, P., & Zamorani, G. 2007, *Astrophys. J. Suppl. Ser.*, 172, 29
- Hemmati, S., Miller, S. H., Mobasher, B., Nayyeri, H., Ferguson, H. C., Guo, Y., Koekemoer, A. M., Koo, D. C., & Papovich, C. 2014, *Astrophys. J.*, 797, 108
- Hill, A. R., Muzzin, A., Franx, M., & Marchesini, D. 2017, *Astrophys. J. Lett.*, 849, L26
- Hubble, E. P. 1936, *Realm of the Nebulae*
- Inoue, S. & Yoshida, N. 2019, *Mon. Not. R. Astron. Soc.*, 488, 4400
- Kauffmann, G., White, S. D. M., Heckman, T. M., Ménard, B., Brinchmann, J., Charlot, S., Tremonti, C., & Brinkmann, J. 2004, *Mon. Not. R. Astron. Soc.*, 353, 713
- Kereš, D., Katz, N., Weinberg, D. H., & Davé, R. 2005, *Mon. Not. R. Astron. Soc.*, 363, 2
- Koekemoer, A. M., Aussel, H., Calzetti, D., Capak, P., Giavalisco, M., Kneib, J. P., Leauthaud, A., Le Fèvre, O., McCracken, H. J., Massey, R., Mobasher, B., Rhodes, J., Scoville, N., & Shopbell, P. L. 2007, *Astrophys. J. Suppl. Ser.*, 172, 196
- Koekemoer, A. M., Faber, S. M., Ferguson, H. C., Grogin, N. A., Kocevski, D. D., Koo, D. C., Lai, K., Lotz, J. M., Lucas, R. A., McGrath, E. J., Ogaz, S., Rajan, A., Riess, A. G., Rodney, S. A., Strolger, L., Casertano, S., Castellano, M., Dahlen, T., Dickinson, M., Dolch, T., Fontana, A., Giavalisco, M., Grazian, A., Guo, Y., Hathi, N. P., Huang, K.-H., van der Wel, A., Yan, H.-J., Acquaviva, V., Alexander, D. M., Almaini, O., Ashby, M. L. N.,

- Barden, M., Bell, E. F., Bournaud, F., Brown, T. M., Caputi, K. I., Cassata, P., Challis, P. J., Chary, R.-R., Cheung, E., Cirasuolo, M., Conselice, C. J., Roshan Cooray, A., Croton, D. J., Daddi, E., Davé, R., de Mello, D. F., de Ravel, L., Dekel, A., Donley, J. L., Dunlop, J. S., Dutton, A. A., Elbaz, D., Fazio, G. G., Filippenko, A. V., Finkelstein, S. L., Frazer, C., Gardner, J. P., Garnavich, P. M., Gawiser, E., Gruetzbauch, R., Hartley, W. G., Häussler, B., Herrington, J., Hopkins, P. F., Huang, J.-S., Jha, S. W., Johnson, A., Kartaltepe, J. S., Khostovan, A. A., Kirshner, R. P., Lani, C., Lee, K.-S., Li, W., Madau, P., McCarthy, P. J., McIntosh, D. H., McLure, R. J., McPartland, C., Mobasher, B., Moreira, H., Mortlock, A., Moustakas, L. A., Mozena, M., Nandra, K., Newman, J. A., Nielsen, J. L., Niemi, S., Noeske, K. G., Papovich, C. J., Pentericci, L., Pope, A., Primack, J. R., Ravindranath, S., Reddy, N. A., Renzini, A., Rix, H.-W., Robaina, A. R., Rosario, D. J., Rosati, P., Salimbeni, S., Scarlata, C., Siana, B., Simard, L., Smidt, J., Snyder, D., Somerville, R. S., Spinrad, H., Straughn, A. N., Telford, O., Teplitz, H. I., Trump, J. R., Vargas, C., Villforth, C., Wagner, C. R., Wand ro, P., Wechsler, R. H., Weiner, B. J., Wiklind, T., Wild, V., Wilson, G., Wuyts, S., & Yun, M. S. 2011, *Astrophys. J. Suppl. Ser.*, 197, 36
- Kriek, M., van Dokkum, P. G., Labbé, I., Franx, M., Illingworth, G. D., Marchesini, D., & Quadri, R. F. 2009, *The Astrophysical Journal*, 700, 221
- Li, H., Vogelsberger, M., Marinacci, F., Sales, L., & Torrey, P. 2020, arXiv e-prints, arXiv:2001.07214
- Lin, L., Patton, D. R., Koo, D. C., Casteels, K., Conselice, C. J., Faber, S. M., Lotz, J., Willmer, C. N. A., Hsieh, B. C., Chiueh, T., Newman, J. A., Novak, G. S., Weiner, B. J., & Cooper, M. C. 2008, *Astrophys. J.*, 681, 232
- Livermore, R. C., Jones, T. A., Richard, J., Bower, R. G., Swinbank, A. M., Yuan, T. T., Edge, A. C., Ellis, R. S., Kewley, L. J., Smail, I., Coppin, K. E. K., & Ebeling, H. 2015, *Mon. Not. R. Astron. Soc.*, 450, 1812
- Lotz, J. M., Jonsson, P., Cox, T. J., Croton, D., Primack, J. R., Somerville, R. S., & Stewart, K. 2011, *Astrophys. J.*, 742, 103
- Madau, P. & Dickinson, M. 2014, *Annu. Rev. Astron. Astrophys.*, 52, 415
- Magain, P., Courbin, F., & Sohy, S. 1998, *Astrophys. J.*, 494, 472
- Maíz Apellániz, J. 2006, *Astron. J.*, 131, 1184
- Man, A. W. S., Zirm, A. W., & Toft, S. 2016, *Astrophys. J.*, 830, 89
- Mandelker, N., Dekel, A., Ceverino, D., Tweed, D., Moody, C. E., & Primack, J. 2014, *Mon. Not. R. Astron. Soc.*, 443, 3675
- Mantha, K. B., McIntosh, D. H., Brennan, R., Ferguson, H. C., Kodra, D., Newman, J. A., Rafelski, M., Somerville, R. S., Conselice, C. J., Cook, J. S., Hathi, N. P., Koo, D. C., Lotz, J. M., Simmons, B. D., Straughn, A. N., Snyder, G. F., Wuyts, S., Bell, E. F., Dekel, A., Kartaltepe, J., Kocevski, D. D., Koekemoer, A. M., Lee, S.-K., Lucas, R. A., Pacifici, C., Peth, M. A., Barro, G., Dahlen, T., Finkelstein, S. L., Fontana, A., Galametz, A., Grogin, N. A., Guo, Y., Mobasher, B., Nayyeri, H., Pérez-González, P. G., Pforr, J., Santini, P., Stefanon, M., & Wiklind, T. 2018, *Mon. Not. R. Astron. Soc.*, 475, 1549
- Martin, D. C., Fanson, J., Schiminovich, D., Morrissey, P., Friedman, P. G., Barlow, T. A., Conrow, T., Grange, R., Jelinsky, P. N., Milliard, B., Siegmund, O. H. W., Bianchi, L., Byun, Y.-I., Donas, J., Forster, K., Heckman, T. M., Lee, Y.-W., Madore, B. F., Malina, R. F., Neff, S. G., Rich, R. M., Small, T., Surber, F., Szalay, A. S., Welsh, B., & Wyder, T. K. 2005, *Astrophys. J. Lett.*, 619, L1
- Massey, R., Stoughton, C., Leauthaud, A., Rhodes, J., Koekemoer, A., Ellis, R., & Shaghoulain, E. 2010, *Mon. Not. R. Astron. Soc.*, 401, 371

- McCracken, H. J., Milvang-Jensen, B., Dunlop, J., Franx, M., Fynbo, J. P. U., Le Fèvre, O., Holt, J., Caputi, K. I., Goranova, Y., Buitrago, F., Emerson, J. P., Freudling, W., Hudelot, P., López-Sanjuan, C., Magnard, F., Mellier, Y., Møller, P., Nilsson, K. K., Sutherland, W., Tasca, L., & Zabl, J. 2012, *Astron. Astrophys.*, 544, A156
- McLeod, D. J., McLure, R. J., Dunlop, J. S., Robertson, B. E., Ellis, R. S., & Targett, T. A. 2015, *Mon. Not. R. Astron. Soc.*, 450, 3032
- Mieda, E., Wright, S. A., Larkin, J. E., Armus, L., Juneau, S., Salim, S., & Murray, N. 2016, *Astrophys. J.*, 831, 78
- Momcheva, I. G., van Dokkum, P. G., van der Wel, A., Brammer, G. B., MacKenty, J., Nelson, E. J., Leja, J., Muzzin, A., & Franx, M. 2017, *Publ. Astron. Soc. Pac.*, 129, 015004
- Mowla, L. A., van Dokkum, P., Brammer, G. B., Momcheva, I., van der Wel, A., Whitaker, K., Nelson, E., Bezanson, R., Muzzin, A., Franx, M., MacKenty, J., Leja, J., Kriek, M., & Marchesini, D. 2019, *Astrophys. J.*, 880, 57
- Murata, K. L., Kajisawa, M., Taniguchi, Y., Kobayashi, M. A. R., Shioya, Y., Capak, P., Ilbert, O., Koekemoer, A. M., Salvato, M., & Scoville, N. Z. 2014, *Astrophys. J.*, 786, 15
- Muzzin, A., Marchesini, D., Stefanon, M., Franx, M., Milvang-Jensen, B., Dunlop, J. S., Fynbo, J. P. U., Brammer, G., Labbé, I., & van Dokkum, P. 2013, *The Astrophysical Journal Supplement Series*, 206, 8
- Oesch, P. A., Brammer, G., van Dokkum, P. G., Illingworth, G. D., Bouwens, R. J., Labbé, I., Franx, M., Momcheva, I., Ashby, M. L. N., Fazio, G. G., Gonzalez, V., Holden, B., Magee, D., Skelton, R. E., Smit, R., Spitler, L. R., Trenti, M., & Willner, S. P. 2016, *Astrophys. J.*, 819, 129
- Oliver, S. J., Bock, J., Altieri, B., Amblard, A., Arumugam, V., Aussel, H., Babbedge, T., Beelen, A., Béthermin, M., Blain, A., Boselli, A., Bridge, C., Brisbin, D., Buat, V., Burgarella, D., Castro-Rodríguez, N., Cava, A., Chanical, P., Cirasuolo, M., Clements, D. L., Conley, A., Conversi, L., Cooray, A., Dowell, C. D., Dubois, E. N., Dwek, E., Dye, S., Eales, S., Elbaz, D., Farrah, D., Feltre, A., Ferrero, P., Fiolet, N., Fox, M., Franceschini, A., Gear, W., Giovannoli, E., Glenn, J., Gong, Y., González Solares, E. A., Griffin, M., Halpern, M., Harwit, M., Hatziminaoglou, E., Heinis, S., Hurley, P., Hwang, H. S., Hyde, A., Ibar, E., Ilbert, O., Isaak, K., Ivison, R. J., Lagache, G., Le Floch, E., Levenson, L., Faro, B. L., Lu, N., Madden, S., Maffei, B., Magdis, G., Mainetti, G., Marchetti, L., Marsden, G., Marshall, J., Mortier, A. M. J., Nguyen, H. T., O'Halloran, B., Omont, A., Page, M. J., Panuzzo, P., Papageorgiou, A., Patel, H., Pearson, C. P., Pérez-Fournon, I., Pohlen, M., Rawlings, J. I., Raymond, G., Rigopoulou, D., Riguccini, L., Rizzo, D., Rodighiero, G., Roseboom, I. G., Rowan-Robinson, M., Sánchez Portal, M., Schulz, B., Scott, D., Seymour, N., Shupe, D. L., Smith, A. J., Stevens, J. A., Symeonidis, M., Trichas, M., Tugwell, K. E., Vaccari, M., Valtchanov, I., Vieira, J. D., Viero, M., Vigroux, L., Wang, L., Ward, R., Wardlow, J., Wright, G., Xu, C. K., & Zemcov, M. 2012, *Mon. Not. R. Astron. Soc.*, 424, 1614
- Sandage, A. 1961, *The Hubble Atlas of Galaxies*
- Sanders, D. B., Salvato, M., Aussel, H., Ilbert, O., Scoville, N., Surace, J. A., Frayer, D. T., Sheth, K., Helou, G., Brooke, T., Bhattacharya, B., Yan, L., Kartaltepe, J. S., Barnes, J. E., Blain, A. W., Calzetti, D., Capak, P., Carilli, C., Carollo, C. M., Comastri, A., Daddi, E., Ellis, R. S., Elvis, M., Fall, S. M., Franceschini, A., Giavalisco, M., Hasinger, G., Impey, C., Koekemoer, A., Le Fèvre, O., Lilly, S., Liu, M. C., McCracken, H. J., Mobasher, B., Renzini, A., Rich, M., Schinnerer, E., Shopbell, P. L., Taniguchi, Y., Thompson, D. J., Urry, C. M., & Williams, J. P. 2007, *Astrophys. J. Suppl. Ser.*, 172, 86
- Schinnerer, E., Smolčić, V., Carilli, C. L., Bondi, M., Ciliegi, P., Jahnke, K., Scoville, N. Z., Aussel, H., Bertoldi, F., Blain, A. W., Impey, C. D., Koekemoer, A. M., Le Fèvre, O., & Urry, C. M. 2007, *Astrophys. J. Suppl. Ser.*, 172, 46

- Scott, K. S., Austermann, J. E., Perera, T. A., Wilson, G. W., Aretxaga, I., Bock, J. J., Hughes, D. H., Kang, Y., Kim, S., Mauskopf, P. D., Sanders, D. B., Scoville, N., & Yun, M. S. 2008, *Mon. Not. R. Astron. Soc.*, 385, 2225
- Shibuya, T., Ouchi, M., Kubo, M., & Harikane, Y. 2016, *Astrophys. J.*, 821, 72
- Soto, E., de Mello, D. F., Rafelski, M., Gardner, J. P., Teplitz, H. I., Koekemoer, A. M., Ravindranath, S., Grogin, N. A., Scarlata, C., Kurczynski, P., & Gawiser, E. 2017, *Astrophys. J.*, 837, 6
- Stott, J. P., Swinbank, A. M., Johnson, H. L., Tiley, A., Magdis, G., Bower, R., Bunker, A. J., Bureau, M., Harrison, C. M., Jarvis, M. J., Sharples, R., Smail, I., Sobral, D., Best, P., & Cirasuolo, M. 2016, *Mon. Not. R. Astron. Soc.*, 457, 1888
- Tacchella, S., Dekel, A., Carollo, C. M., Ceverino, D., DeGraf, C., Lapiner, S., Mandelker, N., & Primack Joel, R. 2016, *Mon. Not. R. Astron. Soc.*, 457, 2790
- Tacconi, L. J., Genzel, R., Neri, R., Cox, P., Cooper, M. C., Shapiro, K., Bolatto, A., Bouché, N., Bournaud, F., Burkert, A., Combes, F., Comerford, J., Davis, M., Schreiber, N. M. F., Garcia-Burillo, S., Gracia-Carpio, J., Lutz, D., Naab, T., Omont, A., Shapley, A., Sternberg, A., & Weiner, B. 2010, *Nature*, 463, 781
- Taniguchi, Y., Kajisawa, M., Kobayashi, M. A. R., Shioya, Y., Nagao, T., Capak, P. L., Aussel, H., Ichikawa, A., Murayama, T., Scoville, N. Z., Ilbert, O., Salvato, M., Sanders, D. B. B., Mobasher, B., Miyazaki, S., Komiyama, Y., Le Fèvre, O., Tasca, L., Lilly, S., Carollo, M., Renzini, A., Rich, M., Schinnerer, E., Kaifu, N., Karoji, H., Arimoto, N., Okamura, S., Ohta, K., Shimasaku, K., & Hayashino, T. 2015, *Publ. Astron. Soc. Jpn.*, 67, 104
- Taniguchi, Y., Scoville, N., Murayama, T., Sanders, D. B., Mobasher, B., Aussel, H., Capak, P., Ajiki, M., Miyazaki, S., Komiyama, Y., Shioya, Y., Nagao, T., Sasaki, S. S., Koda, J., Carilli, C., Giavalisco, M., Guzzo, L., Hasinger, G., Impey, C., LeFevre, O., Lilly, S., Renzini, A., Rich, M., Schinnerer, E., Shopbell, P., Kaifu, N., Karoji, H., Arimoto, N., Okamura, S., & Ohta, K. 2007, *Astrophys. J. Suppl. Ser.*, 172, 9
- van den Bergh, S., Abraham, R. G., Ellis, R. S., Tanvir, N. R., Santiago, B. X., & Glazebrook, K. G. 1996, *Astron. J.*, 112, 359
- Volonteri, M., Saracco, P., & Chincarini, G. 2000, *Astron. Astrophys. Suppl. Ser.*, 145, 111
- Whitaker, K. E., Labbé, I., van Dokkum, P. G., Brammer, G., Kriek, M., Marchesini, D., Quadri, R. F., Franx, M., Muzzin, A., Williams, R. J., Bezanson, R., Illingworth, G. D., Lee, K.-S., Lundgren, B., Nelson, E. J., Rudnick, G., Tal, T., & Wake, D. A. 2011, *Astrophys. J.*, 735, 86
- Whitaker, K. E., van Dokkum, P. G., Brammer, G., & Franx, M. 2012, *Astrophys. J. Lett.*, 754, L29
- Williams, R. E., Blacker, B., Dickinson, M., Dixon, W. V. D., Ferguson, H. C., Fruchter, A. S., Giavalisco, M., Gilliland, R. L., Heyer, I., Katsanis, R., Levay, Z., Lucas, R. A., McElroy, D. B., Petro, L., Postman, M., Adorf, H.-M., & Hook, R. 1996, *Astron. J.*, 112, 1335
- Williams, R. J., Quadri, R. F., Franx, M., van Dokkum, P., & Labbé, I. 2009, *Astrophys. J.*, 691, 1879
- Williams, R. J., Quadri, R. F., Franx, M., van Dokkum, P., Toft, S., Kriek, M., & Labbé, I. 2010, *Astrophys. J.*, 713, 738
- Wuyts, S., Förster Schreiber, N. M., Genzel, R., Guo, Y., Barro, G., Bell, E. F., Dekel, A., Faber, S. M., Ferguson, H. C., Giavalisco, M., Grogin, N. A., Hathi, N. P., Huang, K.-H., Kocevski, D. D., Koekemoer, A. M., Koo, D. C., Lotz, J., Lutz, D., McGrath, E., Newman, J. A., Rosario, D., Saintonge, A., Tacconi, L. J., Weiner, B. J., & van der Wel, A. 2012, *Astrophys. J.*, 753, 114

Wuyts, S., Förster Schreiber, N. M., Nelson, E. J., van Dokkum, P. G., Brammer, G., Chang, Y.-Y., Faber, S. M., Ferguson, H. C., Franx, M., Fumagalli, M., Genzel, R., Grogin, N. A., Kocevski, D. D., Koekemoer, A. M., Lundgren, B., Lutz, D., McGrath, E. J., Momcheva, I., Rosario, D., Skelton, R. E., Tacconi, L. J., van der Wel, A., & Whitaker, K. E. 2013, *Astrophys. J.*, 779, 135

Zanella, A., Le Floch, E., Harrison, C. M., Daddi, E., Bernhard, E., Gobat, R., Strazzullo, V., Valentino, F., Cibinel, A., Sánchez Almeida, J., Kohandel, M., Fensch, J., Behrendt, M., Burkert, A., Onodera, M., Bournaud, F., & Scholtz, J. 2019, *Mon. Not. R. Astron. Soc.*, 489, 2792